UNIVERSIDAD DE GRANADA

Departamento de Electrónica y Tecnología de Computadores

TESIS DOCTORAL

Desarrollo de instrumentación portátil microcontrolada en el ámbito de la salud y el deporte

Author:
Isidoro Ruiz Garcia

Supervisors:
Miguel Ángel Carvajal Rodríguez
Pablo Escobedo Araque

To apply for:
International PhD Degree in Information and Communication Technologies

Programa de Doctorado en Tecnologías de la Información y las Comunicaciones

Julio 2024

Editor: Universidad de Granada. Tesis Doctorales
Autor: Isidoro Ruiz García
ISBN: 978-84-1195-436-5
URI: https://hdl.handle.net/10481/94932

A mis padres.
A mis hermanos.

Agradecimientos

No puedo comenzar esta tesis sin agradecer a todos los que directa o indirectamente han ayudado a que algo que, hace unos años ni tan siquiera entraba en mis planes, hoy sea una realidad.

Empezando por la forma tan peculiar en la que llegué a este grupo de investigación, gracias a ti Migue, que confiaste en mi y me diste esa oportunidad que no olvidaré. Me "engañaste" para acabar haciendo el doctorado y no puedo estar más agradecido por ello. Aunque me respondas correos a las 2.00 a.m. o haya que "apretarse" para ir a irradiar a cualquier sitio preparándolo todo en 4 días, ha merecido la pena (y mucho) por esos ratos, esas cervezas post-curro y todo lo que he aprendido de ti. Estas palabras de agradecimiento las tengo que extender a mi otro director, Pablo, con quien he tenido la suerte de compartir despacho y mesa (cuando no estaba de baja por repoblar el mundo). Eres un ejemplo que seguir.

Gracias a Alberto Palma, que, aun sin ser mi director de tesis me dió la oportunidad de estar aquí con la FPI de la que es mi responsable. Todo lo que he aprendido de ti lo llevaré siempre conmigo. Gracias también a Nuria López, Antonio Martínez y Jesús Banqueri que me han prestado su ayuda siempre que lo he necesitado. No me olvido de la suerte que he tenido de compartir penas y alegrías con los Antonios: Pérez, Pousibet y Juanan. Aunque a veces os "mataría" no habría sido lo mismo sin esos cafés o cerves en la Posada. Ánimo con lo que os queda.

Todo esto tampoco habría sido posible sin la colaboración de los servicios de Radiofísica del Hospital Universitario Clínico San Cecilio, en especial a Damian Guirado, gracias por tu tiempo y dedicación. Agradecer también al departamento de Química Analítica de la Universidad de Granada, con quien he colaborado durante el desarrollo de esta investigación, mencionando especialmente a Luis Fermin Capitán.

Tampoco me olvido de todos esos amigos y familiares que han mostrado su apoyo (incluso admiración) durante estos años. Gracias por acordaros e interesaros por mi, me habéis ayudado mucho a estar hoy donde estoy.

Gracias a la persona que me acompaña y que ha aparecido en mi vida para ayudarme y darme todo su apoyo y cariño, Gracia. Aunque a veces sea un poco desastre e insoportable o se me olviden las cosas, siempre estas para animarme y acompañarme (incluso en la distancia, donde fuiste el principal pilar sobre el que sustentarme). Y he dejado para el final a los más importantes, aquí quiero dar las gracias de corazón a mi familia. El cariño y comprensión que han tenido en todo este camino ha sido indispensable, sin vosotros no habría llegado hasta aquí. Gracias a mis padres, Isidoro y Sonia por lo que me habéis enseñado y cómo lo habéis hecho. Por educarnos a mi y a mis hermanos de la mejor manera, darnos tanto cuanto hemos necesitado, dejar que

nos equivoquemos y ayudarnos a resolver todos los problemas que hemos tenido. Lo habéis hecho mejor que bien, me faltan palabras para expresar todo lo que siento y lo orgulloso que estoy de ser quien soy gracias a vosotros. Gracias a mis hermanos Lorena y Rubén, aunque no seáis tan pequeños ya, siempre seré vuestro hermano mayor para todo lo que os haga falta, para ayudaros y enseñaros, así como para aprender de vosotros. No me faltéis, os quiero.

Una vez más, a todos, **GRACIAS**.

Resumen

Motivación y objetivos

Un microprocesador es un circuito integrado que actúa como la unidad central de procesamiento (CPU) de una computadora. Este componente es fundamental para ejecutar las instrucciones de los programas informáticos, gestionando las operaciones básicas de aritmética, lógica, control y entrada/salida. Los microcontroladores trabajan junto a otros tipos de componentes y circuitos electrónicos, normalmente conectados a través de una placa de circuito impreso (PCB). Esta combinación de microcontrolador, conexiones y periféricos o sensores desempeña un papel clave en el control, la supervisión y el funcionamiento de diversos tipos de sistemas.

Cabe destacar que el estudio objeto de esta tesis doctoral profundizará en tres campos aparentemente distintos: la investigación sobre dispositivos semiconductores como sensores dosimétricos en radioterapia, del uso de sensores inerciales aplicados a la monitorización deportiva y las plataformas microfluídicas para la monitorización de flujos en sustratos celulósicos. A pesar de que estas áreas puedan parecer a priori inconexas, la motivación subyacente a esta investigación surge de un hilo conductor común: la búsqueda de soluciones innovadoras para la detección de diversos parámetros mediante plataformas microcontroladas en el ámbito de la atención sanitaria. Los objetivos de esta tesis pueden dividirse entre los tres temas antes mencionados, aunque comparten muchas similitudes. En general, se han diseñado, desarrollado, fabricado y validado plataformas sensoras de bajo coste, portátiles y basadas en microcontroladores.

El primer objetivo de la tesis consiste en el desarrollo de un nuevo sistema de dosimetría basado en el trabajo previo realizado en el seno de nuestro grupo de investigación. Esto implica la adaptación del sistema desarrollado para su uso con otros dispositivos sensores (como fotodiodos), así como la implementación de los correspondientes algoritmos de compensación térmica necesarios para un funcionamiento preciso durante los procesos de dosimetría en vivo.

La motivación tras el desarrollo de esta plataforma sensora es clara: La radioterapia es una de las técnicas actuales más eficientes para tratar tumores sólidos, por lo que resulta esencial garantizar que la energía absorbida sea suficiente para eliminar las células tumorales, pero sin que supere un determinado nivel umbral para evitar el riesgo de provocar daños en los tejidos sanos. Por lo tanto, en los tratamientos de radioterapia es obligatorio controlar con gran precisión la dosis administrada (energía absorbida por unidad de masa). Para realizar esta medición, los sensores dosimétricos más comunes (cámaras de ionización y diodos PN y PIN de silicio fabricados específicamente para la detección de radiación ionizante) producen una corriente de salida proporcional a la tasa de dosis absorbida, que se monitoriza mediante

electrómetros especializados. Como medida dosimétrica se suele proporcionar la carga total generada por la radiación obtenida mediante la integración de la corriente inducida por la radiación. También se utilizan en este campo los transistores MOSFET (Metal-Oxide-Semiconductor Fiel Effect Transistor) fabricados con ciertos procesos específicos que les confieren una sensibilidad especial y una mayor resistencia a la radiación; son los llamados RADFET (RADiation Field Effect Transistor).

El segundo de los objetivos es el desarrollo de un sistema sensor microcontrolado basado en el uso de unidades de medida inerciales (IMU) para la monitorización de la actividad física y deportiva. Estos dispositivos permitirán el estudio de la técnica, ayudando así a mejorar el rendimiento y previniendo posibles lesiones. A lo largo de los años, se han propuesto diferentes sistemas y metodologías para supervisar el rendimiento de los deportistas, así como su ejecución técnica. Entre las más utilizadas se encuentra el análisis de vídeo y el uso de sistemas globales de navegación por satélite (GNSS). Las IMU, en cambio, presentan varias ventajas con respecto a sus predecesoras. Su bajo coste, pequeño tamaño y versatilidad han causado un aumento significativo en la utilización de estos dispositivos para la monitorización de diferentes deportes, así como en estudios del movimiento y posturales.

El último objetivo consiste en desarrollar una plataforma analítica completa basada en tecnología microfluídica capilar sobre sustratos celulósicos y textiles. La microfluídica y la evolución observada en las tecnologías asociadas a su desarrollo han sido determinantes en el progreso en el campo de los sistemas de análisis total (µTAS), también conocidos como Lab-on-a-chip (LOC). Este sistema debe incorporar materiales actuadores que respondan a diferentes estímulos, incluyendo los de tipo fotosensible, electrosensible y quimiosensible. Como resultado, operaciones como la mezcla, interrupción o ralentización del flujo para facilitar reacciones químicas o separaciones, la disolución y transporte de reactivos encapsulados, la inmovilización de reactivos y las inyecciones o diluciones secuenciales, podrán llevarse a cabo. Esto permitirá realizar análisis más complejos, hasta ahora inalcanzables.

Resultados y conclusiones

Expuestos los objetivos y la motivación de los diferentes estudios realizados, a continuación se resumen los resultados obtenidos en esta tesis por compendio organizados de forma similar a los objetivos.

El sistema dosimétrico desarrollado se basó en un microcontrolador de la familia PIC del fabricante Microchip, en concreto el PIC18F46K42. Este dispositivo destaca por su potente núcleo de procesamiento, capaz de ejecutar instrucciones complejas con alta precisión y eficiencia, lo que lo hace ideal para aplicaciones que requieren respuestas en tiempo real. Incluye numerosos periféricos integrados, como interfaces UART, SPI e I2C, facilitando la conectividad con dispositivos externos y sensores. Además, el

PIC18F46K42 ofrece un ecosistema robusto de herramientas de desarrollo y software, lo que permite simplificar el desarrollo y prototipado de aplicaciones.

En dosimetría con diodos y fotodiodos, el parámetro de interés es la corriente inducida por la radiación. Para medirla, es necesario realizar una conversión intensidad-voltaje mediante un amplificador operacional con una resistencia de realimentación. Esta señal se filtra (con un filtro RC) y digitaliza mediante un conversor analógico-digital externo. Teniendo en cuenta los componentes empleados y la incertidumbre experimental, se obtuvo una resolución de 200 pA. Además del amplificador de transimpedancia, se incluyó una fuente de corriente a la unidad lectora para polarizar los diodos y fotodiodos, permitiendo medir la tensión en directa ($V\gamma$). Esta modificación se realizó para poder medir la temperatura de los sensores gracias a la relación de $V\gamma$ con la temperatura. El efecto de la temperatura en las mediciones dosimétricas es una limitación importante de los dosímetros de estado sólido, lo cual tiene especial relevancia en el caso de los dosímetros basados en fotodiodos PIN, en los que la corriente de oscuridad depende exponencialmente de la temperatura.

Esta plataforma se empleó en la primera publicación incluida en el compendio para caracterizar diferentes fotodiodos y fototransistores como sensores dosimétricos [¿ref?]. Para ello, se aplicó un ciclo de irradiación escalonado que incluía valores de tasa de dosis de 0.81 a 4.87 cGy/s, alcanzando una dosis absorbida total de 21.4 Gy. Los resultados experimentales del fotodiodo PIN de Si BPW34S mostraron una sensibilidad de (13.9 ± 0.5) nC/cGy, una reducida dependencia de la sensibilidad con la tasa de dosis, y una alta linealidad de la corriente con la tasa de dosis media e instantánea. Como conclusión de esta primera publicación, el fotodiodo PIN de silicio BPW34S resulta ser un candidato fiable para la determinación de la tasa de dosis y la dosis absorbida en la piel en irradiaciones típicas de tratamientos de radioterapia, para el cual se ha medido una pérdida de sensibilidad por debajo del 2% hasta 21.4 Gy.

En la segunda publicación que se incluye como resultado de la tesis por compendio, se presenta un método de compensación térmica basado en la propia estructura del diodo, sin necesidad de un sensor o dispositivo externo. Durante la irradiación, el fotodiodo se conmuta periódicamente de polarización inversa a polarización directa para determinar la temperatura del dispositivo. Esta medición se basa en la dependencia lineal entre la temperatura y la tensión directa del diodo. El procedimiento propuesto redujo la incertidumbre debida a la deriva térmica en un factor de 7.5.

Además de la caracterización descrita anteriormente, para completar el estudio del sensor elegido como dosímetro de haces de fotones, se llevó a cabo una caracterización de la dependencia angular del fotodiodo BPW34S, donde se encontró una dependencia máxima de la sensibilidad del 35.3%. Para solventar este problema se propuso una solución basada en una estructura sensora tridimensional: Un cubo de seis caras con un fotodiodo en cada cara, donde todos los fotodiodos se conectaron en paralelo, consiguiendo así reducir al 10.6%. la dependencia angular.

Siguiendo con la caracterización del fotodiodo BPW34S como sensor dosimétrico, se estudió su respuesta ante haces de protones de 5.36, 70, 150 y 230 MeV. Los resultados obtenidos para la energía más baja no fueron satisfactorios. Sin embargo, para las otras tres energías estudiadas se obtuvo una sensibilidad calculada como la relación entre la carga generada por la radiación ionizante y la dosis suministrada de $(0.32x + 3.81)$, $(0.31x + 2.68)$ y $(0.36x + 5.78)$ µC/Gy, respectivamente.

Posteriormente, se estudió la respuesta de cuatro modelos de diodo frente a rayos gamma de alta tasa (365.17 Gy/min). En este caso, la sensibilidad obtenida para los diferentes modelos testeados osciló entre 101.0 y 66.9 µC/kGy con una degradación máxima del 1.4%.

Para terminar con la caracterización de sensores dosimétricos, se caracterizó y estudió el RADFET VT06 de Varadis (Cork, Ireland) como sensor para haces de protones. Aquí se usó la unidad lectora desarrollada previamente en nuestro grupo de investigación, y se realizaron caracterizaciones ante diferentes energías: 1, 2, 3, 151.23 y 230 MeV. Los resultados mostraron una dependencia de la sensibilidad con la energía, obteniendo sensibilidades de 0.68, 0.79, 0.92, 1.10 y 1.14 mV/Gy, respectivamente.

Continuando con el segundo objetivo, se desarrolló una plataforma microcontrolada basada en el uso de unidades de medida inerciales. Los principales componentes de la placa electrónica son el microcontrolador SAMD21G18 de arquitectura ARM Cortex-M0+, que sirve de columna vertebral para multitud de tareas que requieren capacidades de procesamiento fiables y de alta velocidad, junto con la unidad de medida inercial MPU-9250, que integra magnetómetro, giróscopo y acelerómetro de 3 ejes cada uno. Todo ello, alimentado por batería y a una frecuencia de muestreo de 112 Hz, ofrece una autonomía superior a 10 horas.

En la tercera publicación presentada como resultado de la tesis, se emplea este sistema para analizar la técnica durante la práctica de esquí alpino. En el esquí es importante conocer cómo acelera e inclina los esquís el esquiador durante el giro para evitar lesiones y mejorar la técnica. El objetivo de este trabajo fue validar el sistema para detectar la inclinación y aceleración de los esquís. Para ello se colocó la plataforma desarrollada en cada esquí, detrás de la bota del esquiador, y se obtuvieron los datos de orientación y actitud de los esquís (balanceo, cabeceo y guiñada). Esta información se comparó con los datos recogidos por un sistema de referencia 3D-cinemático basado en vídeo para validar su funcionamiento, obteniéndose el coeficiente de correlación entre 0,9959 y 0,922. Además, los resultados demuestran que el sistema basado en IMU propuesto puede proporcionar datos fiables con baja deriva.

Finalmente, dentro del campo de la microfluídica, se ha desarrollado y evaluado una plataforma sensora que consiste en un par de electrodos metálicos paralelos colocados debajo de la tira de papel que transporta el líquido por capilaridad. A medida que la tira de papel se humedece, la capacidad eléctrica entre estos electrodos se modifica, lo que permite una medición precisa y en tiempo real del flujo capilar sin necesidad de cámaras de vídeo ni sensores de flujo externos. Para ello se empleó el sensor capacitivo AD7746, que mide el cambio de capacidad controlado por un Arduino Nano, el cual posee el microcontrolador ATmega 328. El sensor capacitivo tiene un rango de 8 pF con una precisión de 4fF. Este rango puede ajustarse mediante un desplazamiento (offset) para situarse en torno a los valores de capacidad deseados. En este caso se empleó el ATmega 328 debido a la cantidad de información, librerías y recursos disponibles.

Este sistema dio como resultado la cuarta publicación del compendio, en la que se presenta el desarrollo del mismo. La monitorización precisa y en tiempo real del proceso de absorción de líquidos es esencial para permitir un control preciso del flujo en dispositivos microfluídicos, mejorando así su rendimiento y utilidad. Sin embargo, la mayoría de las estrategias existentes de monitorización del flujo requieren instrumentación externa que suele ser voluminosa e inadecuada para sistemas portátiles.

El rendimiento de la plataforma de monitorización capacitiva se evaluó para diferentes soluciones acuosas (agua purificada y solución de NaCl 1 M), varias geometrías de tiras de papel y varias válvulas químicas a medida para la retención del flujo (barreras a base de quitosano, cera y sacarosa). La validación experimental arrojó un error relativo a escala real del 0.25%, lo que se tradujo en un error de capacidad absoluta de ± 10 fF. En cuanto a la reproducibilidad, la incertidumbre máxima fue inferior a 10 nl/s para la determinación del caudal. Además, los datos experimentales se compararon y validaron con análisis numéricos mediante simulaciones eléctricas y de dinámica de flujo en medios porosos.

Contents

List of Figures

List of Tables

1 Introduction

Microprocessors have demonstrated their utility across a large variety of contexts. These compact integrated devices have revolutionized numerous industries and fields of study thanks to their capacity to execute programmable commands stored within their memory. Comprised of various functional blocks, microprocessors—also known as microcontroller units or simply microcontrollers (μC, UC, or mCU)—provide tailored solutions to a broad spectrum of problems [1-3].

Now, focusing on the present thesis, it is important to highlight that the following study will delve into three seemingly disparate fields: inertial sensor technology applied to sports monitoring, microfluidic platforms for flow monitoring in cellulosic substrates, and the investigation of semiconductors devices as dosimetric sensors in radiotherapy. While these areas may initially appear unrelated, the underlying motivation for this research stems from a common thread: the pursuit of innovative sensing solutions using microcontroller platforms in healthcare. The combination of microcontrollers with other peripherals on the same platform provides a wide range of specific solutions to a variety of challenges, thereby establishing a common ground for the development of pioneering and innovative applications in diverse areas such as sports, biotechnology, and medicine.

1.1 Motivation

In recent times, there has been an increasing demand for monitoring activities in sport practice, reflecting a growing emphasis on tracking performance metrics. In this context, there has been a surge in the utilization of inertial units to measure accelerations and angles in sports, due to the potential of analysing specific parameters to prevent injuries or improve technique [4,5]. In particular, skiing and other winter sports have witnessed a growing demand for technology aimed at improving performance and ensuring the safety of athletes [6,7]. The inclusion of inertial sensors in sports equipment enables detailed and meticulous analysis of movement and posture, which can lead to significant improvements in technique and injury prevention. Therefore, the motivation behind the first sensing platform, which constitutes a part of this research, is driven by the need to leverage technology for the benefit of athletes.

Similar to the trend in sports monitoring, there has also been a parallel trend in health and medical monitoring. In this context, the second sensing platform resulting from this thesis focuses on the field of radiotherapy. Radiotherapy stands as an essential technique in cancer treatment, where precise delivery of radiation doses is of vital importance [8-11]. It is essential to ensure that the absorbed energy is enough to eradicate tumour cells but does not exceed the threshold level to induce new damage in healthy tissues. Therefore, accurate monitoring of the delivered dose becomes mandatory in radiotherapy treatments. The most common dosimetric sensors, such as ionization chambers or the specific silicon PN and PIN diodes, provide an output current under radiation fields. Other semiconductor devices used as radiation sensors are the MOSFET-based (metal-oxide semiconductor field-effect transistor) dosimeters [12-14], in which radiation produces a measurable threshold voltage shift. The exploration of commercial general-purpose devices, not explicitly designed for ionizing radiation detection, as dosimetry sensors for radiotherapy aims to reduce the cost of treatment monitoring. The motivation behind this research lies in optimizing radiotherapy treatments and reducing the treatment expenses by leveraging readily available commercial devices not specifically developed for radiation measurement.

Finally, the common ground of precision instrumentation and the need for accurate monitoring highlight the development of microcontrolled systems in the field of microfluidic analysis, underscoring a broader trend towards the creation of precise yet portable sophisticated sensing platforms. Understanding the phenomenon of liquid wicking in porous media is crucial for various applications, including the transportation of fluids in soils, the absorption of liquids in textiles and paper, and the development of new and efficient microfluidic paper-based analytical devices (μPADs) [15-17]. Overall, microfluidics holds great promise in revolutionizing healthcare and medicine by enabling precise control over fluid behaviour on a small scale, leading to advancements the development of rapid diagnostic devices, precise drug delivery systems, or point-of-care testing [18-20]. Hence, accurate and real-time monitoring of the liquid wicking process is essential to enable precise flow transport and control in microfluidic devices, thus enhancing their performance and usefulness. However, most existing flow monitoring strategies require external instrumentation, are generally bulky and unsuitable for portable systems. In this field, a portable, compact, and cost-effective electronic platform for real-time and wireless flow monitoring of liquid wicking in paper strips would be very useful. Despite the diversity of the topics addressed in this thesis, the underlying connection is the pursuit of technological solutions with significant implications for healthcare and societal benefit. Whether enhancing athletic performance, promoting environmental sustainability, or advancing medical treatment, each of these topics intersects with the broader goal of improving public health outcomes. Therefore, this thesis aims to contribute to the ongoing advancement of science and technology in these critical areas through the development of low-cost, compact, and portable microcontrolled sensing platforms.

1.2 Objectives

The objectives of this thesis can be divided among the three topics addressed, although they share many similarities. Low-cost, portable, and microcontroller-based sensing platforms have been designed, developed, manufactured, and tested. The main objectives, divided into the three research lines, are as follows:

- To enhance the previous dosimetry system based on MOSFETs developed by our research group. This involves the adaptation of the developed system for use with other sensor devices (such as photodiodes) and the implementation of the corresponding thermal compensation algorithms necessary for its accurate operation in in-vivo dosimetry.

- To develop a sensor system based on the use of inertial units for the study of sports and physical activity. These devices will enable the study of the technique, thereby helping to improve performance and preventing potential injuries. The primary objectives include designing these systems for cross-country skiing and monitoring jumps.
- To develop a complete analytical platform based on capillary microfluidics on cellulosic and textile substrates. This system should incorporate actuating materials that respond to different stimuli, including photosensitive, electrosensitive and chemo sensitive type, enabling intelligent control of flow to expand the range and complexity of possible analytical operations. This will allow for more complex analyses so far unattainable.

Among the three objectives outlined, there is a need for communication between the user and the system, so the development of various software interfaces will be also necessary. Considering the requirements and applications of the systems to be developed, user interfaces will be created for PC or smartphone platforms based on Python or Android, respectively.

1.3 Outline of the thesis

It should be emphasized that this is a thesis comprises a compendium of publications resulting from the research work conducted during the pre-doctoral period.

Chapter two provides a review of the previous work conducted along the three main lines of this thesis and the methodology employed, encompassing descriptions of the equipment employed for the different characterizations, the software used for design, simulation, and parameter measurements, and the specific methods and technologies occupied. In addition, this chapter includes a brief introduction to dosimetry and its principles, an overview of different sensors available for this purpose, an updated discussion on inertial sensors used in the specific sports focused on in this study, and finally, a general exploration of liquid wicking in porous media and its applications.

The results and discussion are reported in chapter three. This chapter also shows the results not yet published or included in the compendium, along with the four publications that constitute the thesis by compendium of publications.

Finally, chapter four summarizes the conclusions drawn from the research and outlines future work.

2 Background and Methodology

A microcontroller is a compact computer that is entirely self-contained on a single chip. It can be described as a simplified computer designed to repeatedly execute a single basic program. Typically, a microcontroller is intended to perform a specific automated task pre-programmed by the user. These devices are designed to execute a single task repeatedly, often in a timed loop. This type of application is referred to as embedded, as opposed to the more flexible general-purpose applications managed entirely by a Central Processing Unit (CPU). The programming languages used to code the microcontrollers vary depending on the manufacturer and the type of microcontroller. Some of the commonly used programming languages include C, C++, and assembly language. In comparison, other programmable devices such as Field-Programmable Gate Arrays (FPGAs) offer a different approach: While microcontrollers are fixed-function devices programmed to perform specific tasks, FPGAs provide reconfigurable hardware that allows users to define and modify the functionality of digital circuits through programming. This flexibility makes FPGAs well-suited for applications requiring rapid prototyping, complex algorithm implementation, or tasks demanding high levels of parallel processing. Despite their differences, both microcontrollers and FPGAs serve vital roles in embedded systems, each offering unique advantages depending on the application's requirements. In our case, we have chosen to implement the sensor systems using microcontrollers because FPGAs have higher power consumption, more complex communication with, and less widespread usage.

The fundamentals of microcontrollers dictate that they work in conjunction with other types of components and electronic circuits, typically connected via a printed circuit board (PCB). This combination of microcontroller, connections, and peripherals or sensors plays a key role in the control, monitoring and operation of various types of systems. When properly programmed to react to certain inputs or signal detections, an MCU processor can be used to perform tasks in a wide range of functions and applications. These behaviours can range from simple input-output (I/O) triggers and sensor control to additional component control tasks in much more complex fully integrated systems.

Among the microcontroller options available, three families are popular: Advanced Virtual RISC (Reduced Instruction Set Computer) (AVR), Advanced RISC Machine (ARM) and Peripheral Interface Controller (PIC). The different architectures makes each type more suitable depending on the final application. In addition, the existence of libraries for communication or control of the different sensors created by the community behind each microcontroller was another of the main reasons for selecting the processor to be used in each application. Three microcontrolled sensing platforms were developed in this research with three different purposes, each of them using a different architecture. The characteristics are detailed below:

1. **AVR**

- Architecture: AVR microcontrollers utilize a RISC architecture, focusing on efficiency through a simplified instruction set.
- Manufacturer: Manufactured by Microchip Technology, AVR microcontrollers were originally developed by Atmel Corporation, which was acquired by Microchip in 2016.
- Size and Power Consumption: Renowned for their compact size and low power consumption, AVR microcontrollers are favoured for applications requiring minimal power usage, such as portable devices and battery-powered systems.
- Ease of Use: Programming for AVR microcontrollers typically involves assembly language or C, with development environments like AVR Studio or Atmel's integrated development environment (IDE) providing comprehensive tools for development and debugging.

2. **ARM**
   - Architecture: ARM microcontrollers also employ a RISC architecture but are distinguished by their advanced and powerful designs compared to AVR.
   - Manufacturer: ARM Holdings licenses its technology to various manufacturers such as STMicroelectronics, NXP, and Texas Instruments, resulting in a wide range of ARM-based microcontrollers available in the market.
   - Scalability and Power: Offering high scalability, ARM microcontrollers come in various configurations, from low-power devices to high-performance microcontrollers suitable for complex embedded systems.
   - Development Environment: ARM microcontrollers are typically programmed in high-level languages like C or C++, using development environments such as Keil or Eclipse-based IDEs.
3. **PIC**
   - Architecture: PIC microcontrollers feature a RISC or a CISC architecture, with a more extensive instruction set capable of executing complex operations in a single instruction. Depending on the model and family, it will use one or the other architecture.
   - Manufacturer: Manufactured by Microchip Technology, PIC microcontrollers are renowned for their popularity in consumer electronics and education, owing to their simplicity and availability of learning resources.
   - Popularity: Widely used in hobbyist projects, educational settings, and consumer products, PIC microcontrollers offer simplicity and abundant learning materials.
   - Development Environment: Programming for PIC microcontrollers is typically done using the MPLAB IDE provided by Microchip, offering a comprehensive suite of tools for development and debugging.

Therefore, to address the different challenges posed in this thesis, microcontrollers will be used as the core of the different sensor systems. For each application the sensors will be selected as well as the conditioning and power supply electronics required in each case. Subsequently, the introduction to the fields in which sensor systems will be developed will be provided.

2.1 Dosimetry

Radiotherapy is one of the most common techniques to treat solid tumours. It is essential to ensure that the energy absorbed is enough to eliminate the tumour cells but does not exceed the threshold level to induce damage in healthy tissues. Therefore, an accurate monitoring of delivered dose (energy absorbed per unit mass) is mandatory in radiotherapy treatments. This task is performed by *in vivo* dosimetry. Dosimetry is not only capable of detecting errors in the administered dose, but also allows corrective measures to be taken to improve treatment. This has been recognized as an effective method to reduce the potential risk to patients and increase their safety, as recommended by the International Commission on Radiological Protection [11].

In economic terms, radiotherapy is responsible for about 5 % of the total cost of cancer care [21], and the estimated proportion of patients in Spain with an evidence-based indication for radiotherapy ranges from 49.7 to 51.1 %, which is between 107018 and 110159 people for the year 2012 [22]. These data support the need for further research in the field of dosimetry, trying to find new sensors to reduce treatment costs.

The most common dosimetric sensors (ionization chambers and dedicated silicon PN and PIN diodes) produce an output current proportional to the absorbed dose, which is monitored by specialized electrometers. Also used in this field are MOSFET transistors (Metal-Oxide-Semiconductor Fiel Effect Transistor) manufactured with certain specific processes that give them special sensitivity and higher resistance to radiation; these are called RADFETs (RADiation Field Effect Transistor). These detectors and electrometers are expensive and use high voltages to obtain enough sensitivity.

2.1.1 Radiation types

Radiation is divided into two main categories: ionizing radiation and non-ionizing radiation: Non-ionizing radiation is radiation that does not have enough energy to ionize atoms and molecules upon interacting with matter. This form of radiation generally lacks the energy to break chemical bonds or release electrons from atoms. Examples of non-ionizing radiation include ultraviolet (UV) radiation, microwaves, radio waves, television waves, mobile phone waves, and infrared waves. Non-ionizing radiation has numerous applications in communications technology, heating, lighting, electronics, and medical applications such as laser therapy and light therapy.

In contrast, ionizing radiation is radiation that has enough energy to ionize atoms and molecules upon interacting with matter. This ability to ionize atoms and molecules means that ionizing radiation can release electrons from atoms, creating positively or negatively charged ions and causing changes in the chemical structure of molecules. It can be divided into two categories:

- **Directly ionizing radiation:** It is radiation that directly transfers energy to charged particles (such as electrons or protons) as it passes through matter. This type of radiation interacts directly with atoms or molecules, causing the ejection of electrons from atoms and leading to the formation of ions. Examples of directly ionizing radiation include alpha particles, beta particles, electrons, positrons, and protons.

- **Indirectly ionizing radiation:** It is radiation that does not directly transfer energy to charged particles but instead interacts with matter to produce charged particles indirectly. This type of radiation typically interacts with atoms or molecules to produce secondary particles, such as free radicals or excited atoms, which then ionize other atoms upon further interactions. Examples of indirectly ionizing radiation include X-rays, gamma rays, and neutrons, which primarily interact with matter through electromagnetic or nuclear interactions to produce ionization indirectly.

2.1.2 Radiation sources

The three most commonly used sources of radiation for external radiotherapy are (Figure 1): Lineal accelerator, cobalt-60 source or cyclotron.

(a) (b) (c)

Figure 1*. Radiation sources in radiotherapy: (a) LINAC, (b) Cobalt-60 irradiator, and (c) Cyclotron.*

- **Linear accelerator:** The linear accelerator (LINAC) is now the basic equipment in most radiotherapy centres. They provide high-energy electron and X-ray beams; the clinical range is from a few MeV (mega electron volts) to about twenty MeV. Electron beams have a range of a few centimetres inside the patient and are only used in the treatment of superficial tumours and intraoperative techniques.
- **Cobalt-60 source:** Cobalt-60 (Co-60) sources have historically been used in radiotherapy applications because of their ability to emit high-energy gamma radiation, which is effective in damaging and destroying cancerous tissue. Cobalt-60 emits high-energy gamma radiation with a characteristic energy of approximately 1.17 and 1.33 mega electron volts (MeV). This gamma radiation can penetrate deep into tissue and is effective in damaging and destroying cancer cells. Co-60 sources are in the form of sealed sources, which contain small amounts of Cobalt-60 encapsulated in a shielding material to prevent radiation scattering.
- **Cyclotron:** Cyclotrons can indeed serve as sources for proton and neutron beams used in radiotherapy are commonly employed to accelerate protons to

high energies suitable for therapeutic purposes in proton therapy. In proton therapy, the cyclotron accelerates protons to the desired energy level, typically in the range of tens to hundreds of mega-electron volts (MeV). These high-energy protons are then directed toward the patient's tumour, delivering radiation precisely to the targeted area while minimizing damage to surrounding healthy tissues. Proton therapy is particularly advantageous for treating tumours located near critical organs or in paediatric patients due to its ability to spare healthy tissues from radiation exposure. While less common than proton therapy, cyclotrons can also be used to produce neutron beams for therapeutic purposes in neutron therapy.

2.1.3 Electronic equilibrium

Electronic equilibrium in dosimetry refers to the state of balance between the generation and loss of electrons in an irradiated material. In the context of radiotherapy, when a radiation beam interacts with a material, it results in the release of electrons and other types of secondary particles. These generated secondary electrons can interact with the irradiated material, depositing their energy and causing biological or physical effects [23].

Electronic equilibrium is an important concept because it influences the radiation dose distribution in an irradiated material. When electronic equilibrium is reached, the rate of secondary electron generation is equal to the rate of electron loss due to energy absorption or scattering. In this state, the dose distribution stabilises and becomes more predictable.

In clinical dosimetry, electron balance is crucial to ensure accurate delivery of radiation dose to the target tissue during radiotherapy treatment. Treatment planners use planning algorithms that take electronic balance into account to calculate the dose distribution in the irradiated tissue and optimise treatment accuracy and efficacy.

2.1.4 Ionizing detectors

Although there are different radiation detectors, this work study mainly PIN photodiodes as radiation dosimeters. Therefore, the main ionizing detectors will be introduced.

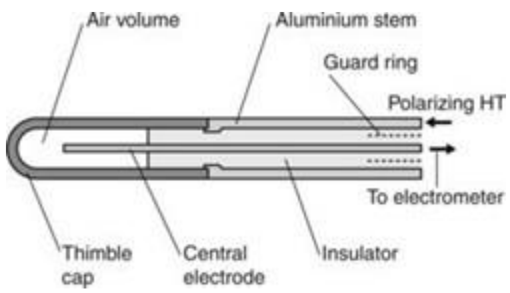

***Figure 2**. Ionization chamber scheme [23].*

- **Ionization chambers**

Currently, the free-air, or standard, ionization chambers are one of the most widely used dosimetric systems in radiotherapy due to their simplicity and reliability. The detector material is a volume of air enclosed in a cavity. The sensitive volume of air is defined by three electrodes: the bias electrode, which is directly connected to one of the poles of the bias voltage source; the collection electrode, which is connected to ground through a low-impedance circuit and is responsible for collecting the charge or current generated in the air cavity; and the guard electrode, which is also directly connected to ground and is intended to delimit the sensitive volume of the chamber and prevent the collection electrode from collecting undesirable currents generated outside the chamber cavity. The chamber cavity is filled with air and the collected charge is a consequence of the ionization of the air molecules by the high energy electrons generated by photoelectric, Compton or pair production on the chamber wall or on the phantom. The electric field applied between the electrodes causes the electric charges generated by the interaction of the radiation to move towards the electrodes of opposite sign. This produces an electric current in the detection circuit that can be measured with an electrometer [13].

However, as ionization chambers are usually manufactured open to the air, the mass of the air inside the cavity depends on pressure, temperature, and humidity. Therefore, corrections are necessary considering the atmospheric conditions under which the measurement was carried out. On the other hand, they have very low dependence on energy and absorbed dose rate. For a better understanding, the schematic of an ionization chamber can be seen in Figure 2.

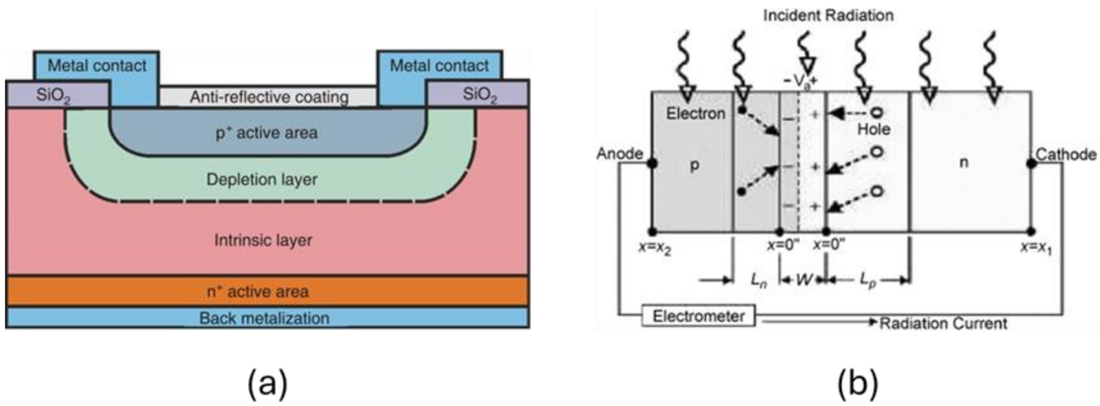

Figure 3*. (a) Silicon PIN photodiode cross-section [24] and (b) schematic diagram of a Si (p, n) diode [26].*

- **Silicon diodes**

Silicon diodes are widely used as dosimetric sensors [24-26]. Ionizing radiation creates electron-hole pairs in their detection volume, which are separated by an electric field. The schematic diagram of a Si (PIN and PN) diode is depicted in Figure 3. As previously explained, in the case of an ionization chamber, electron-hole pairs are created in the volume of air contained in the chamber and these pairs are separated by a high external electric field between the two metal electrodes. Silicon diodes work similarly, but the main sensing volume is the depletion region of the device. Now, the electric field for charge separation can be applied internally (photoconductive mode) or externally (photoconductive mode). The induced current is collected and usually measured with an electrometer. This current is proportional to the radiation dose rate, and integrating the current over exposure time will give a cumulative charge value proportional to the absorbed dose [27-29].

However, semiconductor-based systems generally present an important limitation due to their temperature dependence, hindering an accurate dose measurement. Moreover, even in darkness, the photodiode can present a small current, named dark current, which is also affected by the shunt resistance, a parasitic parallel resistance. In contrast, photodiodes are low cost, small volume, and lightweight detectors.

- **MOSFET (metal-oxide semiconductor field-effect transistor)**

For in vivo dosimetry, other sensors used are MOSFETs. MOS transistors have several advantages for dosimetry applications, such as low power consumption, good sensitivity and reproducibility, and immediate readouts [30,31]. Although these sensors have some advantages, they have low sensitivity in unbiased mode (without external polarization), and at high dose rates, the linearity of their response is reduced. In consequence, MOSFETs manufactured with a special technological process to increase the thickness of gate oxide have been produced, obtaining an increase in sensitivity. The resulting devices are known as RADFETs (Radiation Field Effect Transistor) [32-34]. A comprehensive schematic is shown in Figure 4.

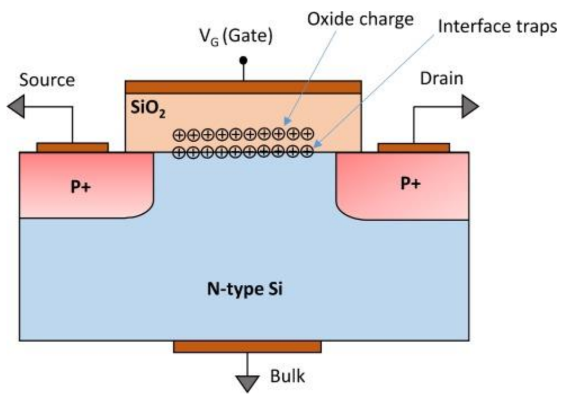

Figure 4. *RADFET cross-section illustrating the radiation-induced charge deposition in the oxide [34].*

In short, the MOSFET sensitivity (S), defined as the shift of $|V_T|$ per dose unit, depends on the radiation energy, the electric field in the oxide, the encapsulation of the transistor, and the incidence direction of the radiation beam during irradiation. Indeed, a transistor in biased mode (a positive voltage is applied between the gate and the source) presents greater sensitivity and a wider linear range than the same transistor in unbiased mode (terminals short-circuited altogether, without external polarization) due to a more efficient charge transport and storage in the oxide [35]. Just after irradiation, the reordering of charges in the MOSFET can change the threshold voltage, which could falsify the dose reading [36]. This is known as the fading effect, and it avoids using MOSFET dosimeters as dose accumulator sensors over long periods of time.

2.1.5 Facilities and equipment

This section presents the specific materials and methods used for the dosimetry research line. In this aspect, the different facilities used, all the devices studied, and the reader unit developed to study the response of the dosimetric devices will be explained.

2.1.5.1 Facilities

The irradiation sessions for dosimetry characterizations were conducted in four facilities of different characteristics, depending on the radiation types and the studies to be conducted:

- **"Hospital Universitario Clínico San Cecilio" (Granada, Spain)**

In recent years, a productive collaboration with the 'Hospital Universitario Clinico San Cecilio' has allowed the access to their facilities for the research conducted by our research group. This collaboration has enabled us to perform the characterisation of the devices using a linear accelerator (LINAC) Siemens Artiste (Siemens Healthcare GmbH, Erlangen, Germany) on numerous occasions, where the photon beam was produced with an electric potential of 6 MV. Typically, devices under test (DUTs) were located in the radiation isocenter (at 100 cm) and were irradiated with a 10x10 cm^2 field. To reach the electronic equilibrium, two solid water phantoms of 1 cm each were placed over the DUT. In addition, five solid water phantoms were placed under the DUT. With these irradiation conditions, regarding delivered dose, one monitor unit (MU) corresponds to 0.973 cGy (calibrated at 300 MU/min with a pulse duration of 3 μs and a pulse repetition frequency of 222 Hz). The constancy checks performed on the LINAC ensure that the absorbed dose per monitor unit varies less than 0.5% during the complete tests.

- **"Centro Nacional de Aceleradores (CNA)" (Sevilla, Spain)**

Figure 5. *CNA Tamdem Accelerator.*

At the CNA, irradiations were carried out using the Tandem Accelerator for generating a low-energy proton beam. It has several beamlines, but only the implantation-irradiation line was used for this test campaign, with protons up to energy 5.36 MeV. Since low-energy protons have a very short range in matter, all the irradiation tests were performed in a vacuum chamber (~10−6 mbar) placed at the end of the beamline. In addition, a Gammabeam™ X200 Cobalt-60 irradiator from Best Theratronics was also available at the CNA for irradiation.

The irradiations carried out at the CNA were held at the Tamdem Accelerator for generating a low-energy proton beam (see Figure 5). It has several beamlines, but only the implantation-irradiation line was used for this test campaign. Since low-energy protons have a very short range in matter, all the irradiation tests were performed in a vacuum chamber (~10^{-6} mbar) placed at the end of the beamline.

Firstly, the proton beam was focused on a scintillator that was placed in the same sample holder as the device under test (DUT), to check the position, shape, and size of the beam to work with around 1 cm^2 spot size; this area completely covered the sensitive area of the DUT. Second, we measured the proton beam flux by using a Brookhaven 1000c current integrator connected to the sample holder, which was electrically insulated from the rest of the line. Then, we used the 2D beam-rastering system to cover a larger surface with the same conditions, so that flux was reduced to the required value. Finally, we moved the sample holder to align the DUT with the beam, and we started the irradiation of the DUT with the fixed conditions. The flux was also measured while the beam was sweeping thanks to the Faraday cup configuration of the sample holder. The fluence associated with each irradiation step was calculated by multiplying the averaged measured flux by the irradiation time.

- **"Centro de Investigaciones Energéticas, Medioambientales y Tecnológicas" (Madrid, Spain)**

A Cobalt-60 source, known as NAYADE, is located in a pool of 1.2 m sides and under 4.5 m water, which provides biological shielding. The main characteristic of this facility is that very high dose rates can be provided. As a special feature, since the cobalt-60 sources are submerged in water, the devices should be submerged to be irradiated. Therefore, the devices under test (DUT) were mounted on a sample holder that was placed into a waterproof chamber. The connection with the reader unit was carried out with an ad-hoc shielded wire of 16 vias inserted into a waterproof tube. Finally, the chamber with the DUTs was positioned close to the Co-60 sources in the pool bottom. With this configuration dose rate up to 21.9 kGy/h was achieved with a dose non-uniformity of 8.74%. To achieve this dose rate, 12 Cobalt-60 sources were arranged in a circle at the bottom of the pool. The dose rate was read at the centre of the circle, inside the sample holder. This capsule could be opened to place the devices under test inside it. The wiring of the sensors was passed through a watertight tube to avoid contact of the electronics with water. In our case, a 10-meter-long shielded cable was used to reduce measurement noise.

In addition, the reader unit that works as an interface between the sensors and the computer was placed in the control room.

- **Paul Scherrer Institute (PSI) (Villigen, Switzerland)**

During the period from November 27 to December 1, 2023, a short research stay was carried out at the Paul Scherrer Institute in Switzerland. Irradiation sessions at PSI were performed in the Proton Irradiation Facility (PIF), where a high energy proton beam between 70 and 230 MeV was available. It enables generating of realistic proton spectra encountered at any potential orbit in space. In this case, tests were performed at three different energies: 69.78, 151.23, and 230 MeV, adjusting the flux to the maximum possible with a beam current of 5 nA. The complete PIF test area is located in air. On the one hand, it provides enough space for users apparatus facilitating easier and faster preparations. On the other hand, the energy losses of high energy protons in air are minimal and can be calculated. The control room is located at the entrance to the Nucleon Area (NA) of the PSI, requiring long unshielded cables of approximately 50 m. Numerous coaxial and high voltage connections, RS232 interfaces, and extended PC cables are available between the test area and the control room.

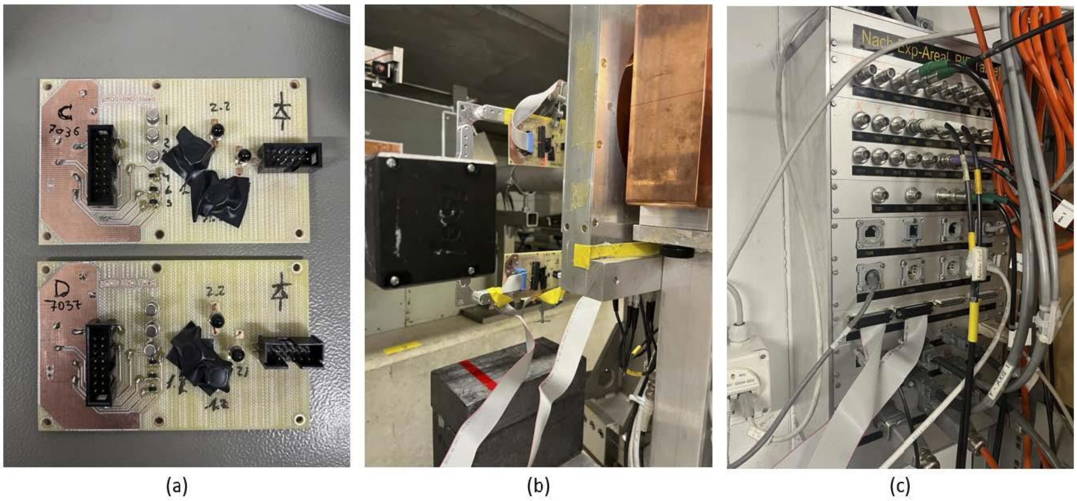

***Figure 6**. Complete setup for irradiations at PSI.*

The basic beam optics components in the NA included beam stops, slits, centering magnets, and focusing quadrupoles that can be operated from the PIF control room, thus enabling fast setting and tuning of the beam. In the preparation phase, the beam was centred on the PIF target and required parameters like profiles and intensities were adjusted.

The irradiation sessions were planned in runs of 2 minutes that provide a dose of about 10 Gy, with rests periods of around 5 minutes of pre- and post-irradiation measurements. Due to the limited time available to perform the tests, experiments had different durations, with a total of 60 Gy per device for RADFET (with a final shot of 100 Gy for two energies), and between 130 and 100 Gy per device for photodiodes.

DUTs were located within a circular region of 5 cm diameter, which was the beam shape provided for this campaign. The boards were positioned centred in this area, so all the devices were tested under the same radiation conditions, i.e., at 8 cm from the beam output. Device encapsulation had been removed for the RADFETs but not for other devices, since for such high energies the penetration depth in matter of the protons was expected to be sufficient to pass through them and reach the active volume.

Two boards were placed in the sample holder at the same time in front of the beam output. This frame was attached to a mechanical system that could be remotely controlled to position the boards in the desired position. During the tests, only one of the boards was irradiated per time, considering the width of the beam and the possible scattering of the incident radiation. Each irradiation was programmed from the control room, indicating the desired energy and the total dose to be delivered, while the flux was always maintained at the maximum value. The reader unit was placed in the control room, connected to a laptop via USB. The DUTs were located inside a bunker that was not accessible during the irradiations, separated from the control room. Two separate cables were used for each of the boards. The complete setup is shown in Figure 6.

2.1.5.2 Devices under test

Although this research is focused on PIN photodiodes, irradiation tests with diodes, phototransistors, Light Depend Resistors (LDR), MOSFETs, and photodiodes were performed.

Photodiodes

Table 1. *Main characteristic of the photodiodes used.*

	Manufacturer	Reverse Voltage (V)	Active area (mm^2)	Central wavelength (nm)	Package
VTB8440BH	PerkinElmer Optoelectronics	40	5.16	525	Ceramic
BPW34S	Vishay Semiconductors	60	7.5	900	Top view
BPW24R	Vishay Semiconductors	60	0.78	900	TO-18
BPW21R	PN Vishay Semiconductors	10	7.5	565	TO-5

Phototransistors

Table 2. *Main characteristic of the phototransistors used.*

	Manufacturer	Type	Viewing Angle	Central wavelength (nm)	Package
BPW85B	Vishay Semiconductors	NPN	25°	860	T-1
OP505A	TT Electronics	NPN	20°	850	T-1

Diodes

Table 3. *Main characteristic of the diodes used.*

	Manufacturer	Type	Reverse Voltage (V)	Package
1N4007	Vishay Semiconductors	Rectifier	1000	DO-41
UF4007	Vishay Semiconductors	Ultrafast Rectifier	1000	DO-41
BY203-20S	Vishay Semiconductors	Avalanche	2000	SOD-57
GP02-40	Vishay Semiconductors	High Voltage Rectifier	4000	DO-41

LDR

Table 4. *Main characteristic of the LDRs used.*

	Manufacturer	Dark resistance (Ω)
NORPS-12	Silonex Inc	1 M
NSL-19M51	Luna Optoelectronics	20 M
VT43N2	Excelitas Technologies	300 K

RADFETs

Table 5. *Main characteristic of the RADFET used.*

	Manufacturer	Gate oxide	Package
VT06	Varadis	100 nm	Eight-lead Ceramic Side Braze

2.1.5.3 Reader units

Once the devices to be studied and the facilities where the tests were performed have been presented, the readout units used to measure the response of the DUTs under the different types of radiation will be explained. Mainly, two different readers were used during the studies: the first one, previously developed by our research group for the study of the use of MOSFETs as dosimeters [37], was employed to analyse the response of RADFETs under different radiation beams. It is based on the PIC16F877A to control all the components. Its main features are a resolution of 60 nA to bias the transistors (drain current) and a maximum bias voltage (gate voltage) of 22 V. Moreover, two channels are available to measure the threshold voltage, the amplifier one with an instrumentation amplifier (INA129 from Texas Instruments, Dallas, USA) and the non-amplifier. On the other hand, to study the behaviour of diodes, photodiodes and phototransistors, a new version of the reader unit, adapted for these devices, was developed. It will be studied in detail in section 4.1.1 This system has two functions essentially: i) To bias the DUT with a buffered voltage divider and ii) to convert to voltage the device´s output current with a transimpedance amplifier.

2.2 Sport monitoring

Over the years, different systems and methodologies have been proposed to monitor the performance of athletes, as well as their technical execution. In particular, skiing presents unique challenges in performance monitoring due to its dynamic nature and the intricacies of snow and terrain interaction. Among the proposed monitoring techniques, those based on video analysis can be highlighted [38]. For this particular sport, a 3D video-based method was implemented to examine kinematic, kinetic, and energetic variables related to skier technique during slalom race simulations [39]. In alpine skiing, some authors used the smartphone Inertial Measurement Units (IMUs) to recognize activity [40]. In addition, a high kinematic accuracy global navigation satellite system (GNSS) was evaluated to detect classical cross-country skiing technique [41]. Other sports involve more specific equipment for performance monitoring, such as jumping monitoring [42]. All the mentioned equipment and techniques require an underlying understanding of their use as well as the interpretation of the results.

IMUs have several advantages over their predecessors. Their low cost, small size, and versatility have led to a significant increase in the utilization of these devices in different sports [43,44], as well as in movement and postural studies [45,46]. Unlike using accelerometer units or gyroscopes, with an IMU, basic measurements (acceleration, rotational speed, or orientation) can be obtained alongside pattern recognition through data processing [47].

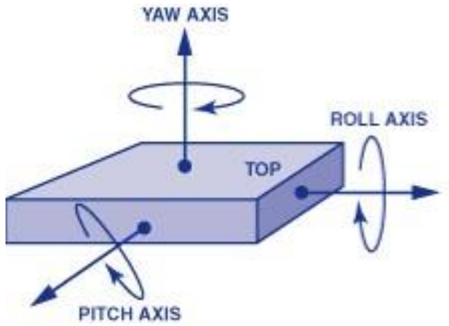

***Figure 7**. Representation of the reference system used in navigation (Yaw, Pitch and Roll).*

More and more elite athletes and coaches are demanding the use of new technologies to monitor and improve their performance, as the correct execution of technique can greatly influence their sporting success. In certain sports, victory can be determined by minute differences, so it is important to obtain as much information as possible from training sessions to identify areas for improvement. IMUs have been applied to monitor performance in a variety of sports. Some examples include skiing, where the angle of the ski entering a turn can be monitored [48]; jumping, where the time of flight and height of the jump can be recognised [49]; basketball, where information about a player's dribbling ability can be discerned from the player's dribbling frequency, captured through acceleration information [50]; or o evaluate the anaerobic power of elite volleyball players [51].

2.2.1 IMUs: Working principle

An IMU is an electronic device used to measure and report the velocity, orientation, and acceleration of a moving object. It consists of three different sensors: a gyroscope, an accelerometer, and a magnetometer. These sensors work together to provide accurate information about the motion and orientation of an object in three-dimensional space. Gyroscopes measure angular velocity or the rate of rotation around a specific axis, while accelerometers measure linear acceleration in a particular direction. By combining readings from these sensors, an IMU can calculate the orientation, position, and changes in velocity of a moving object. These inertial sensors are used in a wide range of applications, including inertial navigation in aerial, terrestrial, and maritime vehicles, stabilization of cameras and platforms, virtual and augmented reality, robotics, wearable devices such as activity trackers, and gaming devices, among others [52,53].

Typically, there are two types of IMUs: six degrees of freedom (6DoF) or nine degrees of freedom (9DoF). The difference between the first and second is that the six-degree-of-freedom IMU uses only a three-axis accelerometer and a three-axis gyroscope to obtain the orientation. On the other hand, in the nine-degree-of-freedom IMUs, information is obtained from the magnetometer to correct the estimates made with the other sensors. Although all the information needed to obtain the position and orientation of a body is available only with the use of accelerometer, magnetometer, and gyroscope, the integration of data is crucial for obtaining accurate estimates of the position and orientation of a body. The role of each sensor is the following:

- **Accelerometer**

  Accelerometers measure acceleration forces along multiple axes. They are commonly used to estimate the orientation of the IMU with respect to the gravity vector. By analyzing the acceleration measurements, especially when the IMU is at rest or in a known orientation, the tilt angles can be determined, providing information about pitch and roll.

- **Gyroscope**

  Gyroscopes measure angular velocity or the rate of rotation around multiple axes. They are used to track changes in orientation over time. By integrating the angular velocity measurements over time, the orientation of the IMU can be estimated relative to its initial orientation.

- **Magnetometer**

  Magnetometers measure the strength and direction of the magnetic field along multiple axes. They provide information about the Earth's magnetic field, which can be used to determine the orientation of the IMU relative to the Earth's magnetic field. Magnetometers are particularly useful for correcting drift in the orientation estimates obtained from accelerometers and gyroscopes, especially over long periods of time.

The integration of data from these sensors typically involves using algorithms such as Kalman filters (including the extended Kalman filter), complementary filters, or sensor fusion algorithms. These algorithms combine data from multiple sensors, taking into account their individual strengths and weaknesses, to provide more accurate estimates of position and orientation [54].

In the case of 6DoF IMUs, only accelerometers and gyroscopes are used for orientation estimation. While this can provide reasonably accurate estimates, it may suffer from drift over time due to the inherent integration of angular velocity measurements. On the other hand, 9DoF IMUs incorporate magnetometer data to correct for drift and provide more stable long-term orientation estimates, especially in environments where magnetic disturbances are present. Overall, the choice between six and nine DoF depends on the specific application requirements, including accuracy, stability, and the presence of magnetic interference in the environment, as well as the computational capacity of the microcontroller.

2.2.2 Data Fusion Algorithms

Data fusion algorithms for IMUs aim to integrate data from accelerometers, gyroscopes, and sometimes magnetometers to provide accurate estimates of orientation, position, and motion [55]. Here are some common data fusion algorithms used for IMUs:

- **Kalman Filter (KF) and Extended Kalman Filter (EKF)**

  The Kalman filter is an estimation algorithm used to filter and predict the state of a dynamic system from incomplete and noisy measurements. It employs a probabilistic model of the system and combines past and present measurements to produce an accurate estimate of the current state [56].
  The Extended Kalman Filter is an extension of the Kalman filter that allows for modelling of nonlinear systems. It utilizes a local linear approximation around the current estimated point to update the system state and covariance [57].

- **Complementary Filter**

  The Complementary Filter is a method used for data fusion from multiple sources, such as sensors, to obtain an accurate estimation of a system's state. It combines two or more signals, typically a high-frequency signal and a low-frequency signal, in a way that each one complements the deficiencies of the other. The high-frequency signal is often utilized to provide a quick response to rapid changes, while the low-frequency signal offers a smooth and accurate response to slow or gradual changes [58].

- **Madgwick Filter**

The Madgwick Filter, also known as the Madgwick AHRS (Attitude and Heading Reference System) algorithm, is a sensor fusion algorithm used primarily for estimating the orientation (attitude) of an IMU based on data from gyroscopes, accelerometers, and magnetometers. It was developed by Sebastian Madgwick and is widely used in applications such as motion tracking, virtual reality, and robotics [59].

The Madgwick Filter employs a quaternion-based approach to represent the orientation of the IMU. It combines measurements from the gyroscope to estimate the rate of change of orientation (angular velocity) with measurements from the accelerometer and magnetometer to correct for drift and biases. The algorithm is computationally efficient and robust, making it suitable for real-time applications.

- **Mahony Filter**

The Mahony Filter [60], is another sensor fusion algorithm used for estimating the orientation (attitude) of an IMU based on data from gyroscopes, accelerometers, and magnetometers, and it reports results similar than the Madgwick Filter. It was developed by Robert Mahony and is widely used in applications such as motion tracking, drone navigation, and robotics.

The Mahony Filter also utilizes a quaternion-based approach to represent the orientation of the IMU. Similar to the Madgwick Filter, it combines measurements from the gyroscope to estimate the rate of change of orientation (angular velocity) with measurements from the accelerometer and magnetometer to correct for drift and biases. One notable difference from the Madgwick Filter is the inclusion of a proportional-integral-derivative (PID) control scheme to address some of the limitations of the original complementary filter.

- **Particle Filters**

Particle Filters, also known as Sequential Monte Carlo methods, are a class of sequential state estimation algorithms used in situations where the system state and/or measurement models are nonlinear, non-Gaussian, or both. They are particularly useful for tracking systems with highly non-linear dynamics or in scenarios where the system is subject to non-Gaussian noise [61].

The basic idea behind Particle Filters is to represent the posterior probability density function (PDF) of the system state using a set of weighted particles, where each particle represents a hypothesis of the state. These particles are propagated forward in time according to the system dynamics, and their weights are updated based on how well they match the measurements received.

As the process continues, particles representing less likely hypotheses are gradually discarded, and particles representing more likely hypotheses are replicated, resulting in a set of particles that approximates the true posterior distribution.

Particle Filters have found applications in various fields, including robotics, target tracking, computer vision and finance, where traditional Kalman filters may not be applicable due to their linear and Gaussian assumptions.

In particular, the Madgwick AHRS algorithm was used for the development of the inertial measurement unit used to monitor several sports. It was chosen because it is computationally efficient and robust, making it ideal for real-time applications. These features also make it compatible for implementation on low-power microcontrollers. In fact, several open-source libraries can be found to implement this algorithm in a simple way.

2.2.3 Sport monitoring equipment

- Ski simulator: MaxxTracks ISB2000 ski simulator (©MaxxTracks Indoor Skislopes, Beverwijk, The Netherland) designed for training, research, and teaching purposes, the dimensions of which are 12.50 × 6.55 m (48 m2) (see Figure 8a). The speed of this treadmill can be varied between 1 and 21 km/h, and the slope ranges from 10° to 19°. Surface wetting is required for achieving suitable skier sliding.

(a) (b)

Figure 8. Equipment used as gold standard for the inertial sensor studies. (a) Ski simulator and infrared cameras and (b) force platform. (image (b) is extracted from the equipment data sheet).

- 3D photogrammetric system: (© 2021 NaturalPoint, Inc. DBA OptiTrack, Beaverton, OR, USA) was used. It is composed of a ring of 12 Flex 3 (resolution: 640 × 480, frame rate: 100 FPS) infrared (IR).
- Force platform: Kistler 9260AA6 (Kistler, Barcelona, Spain), a portable triaxial platform for footprint and balance analysis (see Figure 8b). Its dimensions are 600 × 500 × 50 mm, and it is capable of measuring forces up to 5 kN. The system exhibits a low linearity error (<±0.5% FSO, Full Scale Output) and hysteresis (<0.5% FSO), as well as high sensitivity (0.9–19 mV/N on the z-axis). The sampling frequency on the z-axis is 250 Hz. The platform is connected to the computer via USB through the Bioware software (© 2022 Kistler Group, Barcelona, Spain) to initiate and stop recording the jump sessions, edit the measurements, and download the data for further processing.

2.2.4 Setup for jumping tests

Seven subjects without walking difficulties, comprising one woman and six men aged 18 to 46 (average age 28 ± 9), took part in this research. Their average weight was 72 ± 9 kilograms. All participants were in good health and physically active, engaging in over three exercise sessions per week. However, none of them were competing at an elite level. The selected system used as the gold standard in this study was the Kistler 9260AA6 (Kistler, Barcelona, Spain), a portable triaxial platform for footprint and balance analysis. Participants executed the countermovement jump (CMJ) technique, starting with a knee angle of 180° and hands on hips. They performed a countermovement until the knee angle reached about 90°, followed by an immediate vertical jump to achieve maximum height. Upon landing, knees remained extended at a 180° angle. Each of the seven subjects completed three jumps, totalling 21 measurements. Only the acceleration components were monitored in this study. This method enabled a sampling frequency of 200 Hz, which is similar to the sampling frequency of the reference system.

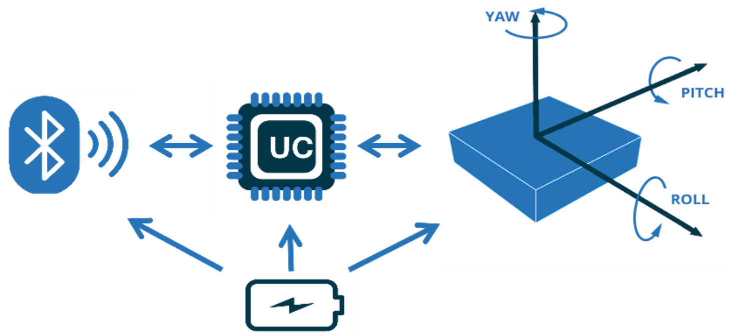

Figure 9. *Schematic of the inertial sensor custom electronic board.*

2.2.5 Inertial sensor and microcontroller

The system used to perform the tests was developed and will be explained in the section 4.1.2. It is mainly composed of a microcontroller (SAMD21G18U) and an inertial unit (MPU-9250) with 9 axes of freedom. With this combination a sample rate of up to 200 Hz with a configurable acceleration from ±2 g to ±16 g, a configurable gyroscope range from ±250 to ±2000 degrees per second and a magnetometer with a range of 4800 μT. Figure 9 shows a simple diagram of the developed system.

2.3 Microfluidics

The growing demand for real-time information to monitor and control different chemical parameters of environmental, industrial, and biomedical interest has promoted significant advances in the field of analytical chemistry. Microfluidics and the evolution observed in the technologies associated with its development have been instrumental in the exponential progress observed in the area of micro-total analysis systems (μTAS), also known as Lab-on-a-chip (LOC). These systems consist of silica, glass, or polymer chips with channels for transporting fluids using different propulsion systems, which can implement various analytical operations and may include electronic signal processing stages to communicate the results to the user.

As part of the platforms where fluid movement is achieved by capillary action, there are three types of substrates: paper, thread, and textile. These devices are known as Paper-based Analytical Devices (μPAD) [62], Thread-based Analytical Devices (μTAD) [63,64] and Cloth-based Analytical Devices (μCAD) [65,66], respectively, presenting some advantages over other microfluidic systems based on silica, glass, or polymers that incorporate fluidic channels prepared by different fabrication procedures. An overview of various applications on the different substrates is shown in Figure 10.

The first works on μPAD appeared in 2008 [67,68] and since then, the number of articles has continuously grown. The paper support allows the design of microfluidic structures capable of integrating different stages of the analytical process, structures that do not require instrumental support, that are disposable and single use, with very low-cost measurements and compatible with signal processing using tools such as smartphones, therefore, presenting an enormous potential for application in chemical analysis. On the other hand, paper is abundant, cheap, sustainable, easy to use, biodegradable, has high compatibility with many chemicals, is biocompatible, easy to modify chemically and, of interest in this application, allows the movement of liquids through it by capillary, passive transport without the need to apply external forces [69,70].

The main problem it presents is that it is necessary to define the path from the sampling zone to the detection zone, passing through areas where analytical operations take place. This is solved by the fabrication of channels through which the sample can flow [71,72].

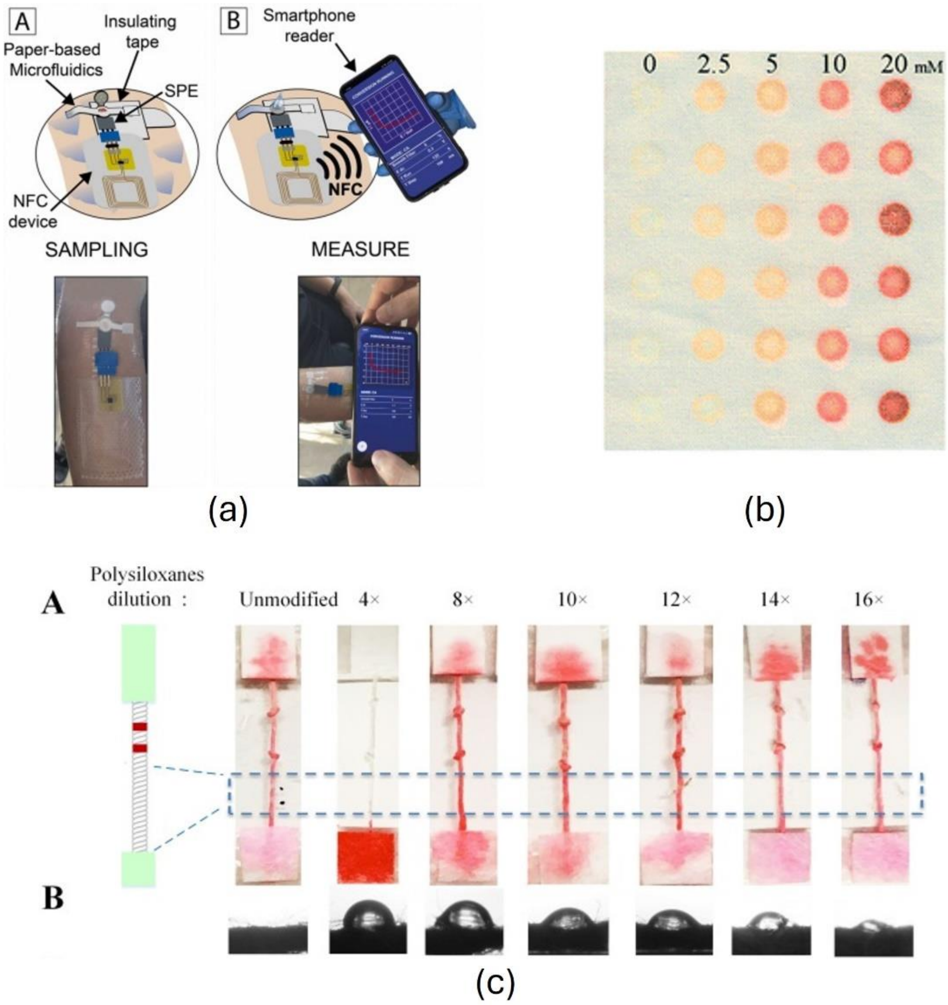

Figure 10. (a) Paper-based Analytical Device (μPAD) for reliable cortisol detection in sweat [62], (b) cloth-based Analytical Device (μCAD) for colorimetric detection of glucose [65], and (c) thread-based Analytical Devices (μTAD) for the development of a sensitive and selective immunoassay [64].

For the design of capillary-type microfluidic devices, it is necessary, first of all, to understand the fluidic characteristics of the material used for their manufacture. Additionally, another essential aspect to implement the necessary analytical strategy in the device is flow control. This allows operations such as flow mixing, flow interruption, or slowing down to facilitate chemical reactions or separations, dissolution and transport of encapsulated reagents, immobilisation of reagents, and sequential injections or dilutions, among others.

Considerable effort has been invested in comprehending the dynamics of liquid imbibition through porous media, owing to the three-phase complex formation of solid–liquid and liquid–gas interfaces. In 1856, Darcy conducted the first experimental investigation of liquid flow in porous media [73]. His model assumes that flow within a porous medium is driven solely by capillary pressure gradient. In 1921, two researchers established a relationship between the capillary height and the rising time of a liquid in porous media, popularly known as the Lucas–Washburn (LW) equation [74,75].

According to the most recent μPAD flow model that includes a term for evaporation, the distance $l(t)$ travelled by a liquid flowing under capillary pressure in a channel is given by:

$$l(t) = \sqrt{\frac{\gamma r \varphi h \cos\vartheta}{4\mu q_0}\left(1 - e^{\frac{2q_0}{\varphi h}t}\right)}$$

To control the flow, the paper porosity φ can be influenced from a chemical point of view, apart from geometrical issues. The other parameters are the surface tension γ, the effective paper pore radius r, the microfluidic channel thickness h, the contact angle ϑ, the dynamic viscosity of the liquid μ, the evaporation rate q_0, and the time t. When q_0 tends to zero, the classical Lucas-Washburn equation is recovered:

$$l(t) = \sqrt{\frac{\gamma r \cos\vartheta}{2\mu}t}$$

As recent reviews indicate [72,76,77], paper porosity, and consequently flow control, has been modulated by both geometrical or mechanical methods and chemical methods, where the most commonly employed are geometrical or mechanical. The first reported designs for flow control in paper devices were achieved by modifying the length and width of the μPAD channels [78]. Subsequently, mechanical designs were used, for example, by using tabs on the paper itself that act as on/off valves operated by the user [79], or by including a magnetised paper valve operated by an electromagnet [80]. Another alternative is the mechanical modification of the porous material; polyethylene sheets pressurised in certain areas have been used, which reduce the porosity and allow both flow and flow mixing to be controlled [81]. Lamination of paper between films of different wetting angles also allows flow control [82]. The inclusion of adsorbent pads in the fluidic channel has also been reported to allow reproducible flow slowdowns [83].

Chemical procedures are based on the inclusion of additives in the μPAD that modify the fluidic characteristics of the device. Such is the use of soluble barriers of different materials whose dissolution modulates the flow, such as sucrose [84], pululan [84], or trehalose [85]. Other alternatives are the use of hydrophobic materials such as paraffin, which slow down the movement [86], or wax, whose melting allows the passage of fluid [87]. Other materials used are ionogels, which modify the flow and allow its modulation [88,89].

Materials with interesting properties are Stimuli-Responsive Materials (SRMs), also known as 'smart polymers'. These are polymers that respond to their environment by changing their physical or chemical properties. These SRMs have found application in different fields such as controlled release of substances, pharmaceuticals, sensitive coatings, shape memory materials, or sensors and biosensors. Most of these materials respond to stimulations such as temperature, light, and pH, although others respond to less common stimuli such as magnetic fields, mechanical forces, or small molecules. Many of their properties stem from a transition in solubility or conformation of a macromolecule in the presence of a solvent under the effect of a stimulus. In this way, transitions at the molecular level can be amplified as a consequence of a change in the nanostructure or properties of the materials [90].

These types of materials are promoting an incipient inclusion of electronic elements to produce the necessary stimulation for flow control: i) light by LEDs, aligned by micro-masks; ii) heat through the inclusion of deposited heaters, based on the Joule effect of metallic materials conducting current [91,92]. Therefore, as electronics have started to be included together with such analytical devices for signal conditioning, the way is open to use it also for stimulus control and thus to develop mixed systems that allow analysis on textile fibres including more complex analytical operations by means of intelligent flow control. This trend will provide systems with low cost and environmental impact, yet capable of increasingly complex in-situ analysis.

2.3.1 Microfluidic monitoring platform

For real-time and wireless flow monitoring of liquid wicking in paper strips a portable, compact, and cost-effective electronic platform was designed (Figure 11). The developed microcontroller-based system enables flow and flow rate monitoring based on the capacitance measurement of a pair of electrodes patterned beneath the paper strip along the liquid path, with an accuracy of 4 fF and a full-scale range of 8 pF. Additionally to the wired transmission of the monitored data to a computer via USB, the liquid wicking process can be followed in real-time via Bluetooth using a custom-developed smartphone application. A more detailed description of this platform can be found in Section 4.1.3.

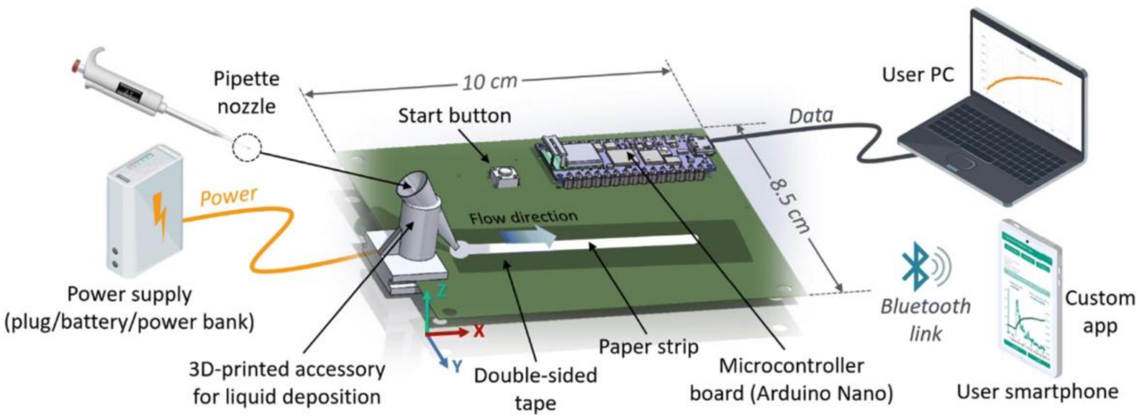

Figure 11. *Overview of the capacitive platform for liquid wicking monitoring [97].*

In addition, filter paper Whatman grade 1 (Merck KGaA, Sant Louis, USA) was selected for all experiments of this. Different paper strip shapes were obtained using a laser cutting machine (Rayjet 50 Laser Engraver, Austria). Hydrophobic double-sided adhesive tape Tesa 64621 (Tesa, Hamburg, Germany) was used to affix the paper strip to the capacitive electrodes. Purified water was produced by a TKA Microlab type II (TKA Wasseraufbereitungssysteme GmbH, Niederelbert, Germany) for the experiments to evaluate the sensing platform's performance. High molecular weight chitosan, NaCl, and sucrose were provided by Sigma-Aldrich Merck (Madrid, Spain) for the chemical experiments. All the dilutions used in the tests were prepared at the Department of Analytical Chemistry of the University of Granada.

2.4 Common Software

Considering the nature of the microcontrolled sensing solutions developed in this work, the software section encompasses the description of the programs used for PCB design, microcontroller programming, and the development of applications for both PCs and smartphones.

- **Electronic simulation software**

In the electronic design process, the initial step involves the simulation of the designed circuit to verify its functionality before implementation. For this purpose, LTSpice® software (Analog Devices, Inc.) has been used. LTspice® is a robust, powerful, fast, and freely available SPICE simulator software with schematic capture and waveform viewer capabilities. It offers enhancements and models to improve the simulation of analog circuits. Its graphical schematic capture interface enables users to analyse schematics and generate simulation results.

- **Engineering & Computer Aided Design (ECAD) software**

Following simulations, ECAD software enables electronics designers to develop a printed circuit board (PCB) layout based on the schematic of their circuit design, as well as generate a virtual representation of the designed PCB displaying component placement with 3D models and generate/display 2D circuit board manufacturing documentation. There is a great variety of software in this area; in our case, the chosen platform was KICAD® due to its availability as free software distribution.

- **3D modelling**

Occasionally, custom parts need to be included in the creations that will be designed and printed in 3D. Blender, an open-source, multi-platform software primarily used for creating 3D graphics, modelling, animation, simulation, rendering, compositing, and video editing, was utilized for this purpose. It is developed by the Blender Foundation.

- **Microcontroller programming**

As discussed in this chapter, given the microcontrollers chosen for each application, two software packages were used for programming the sensing platforms: MPLAB® X Integrated Development Environment (IDE) and Arduino IDE.

MPLAB X IDE, developed by Microchip Technology, is used for programming and debugging microcontrollers and microcontroller-based devices from the PIC family. It is a powerful tool to write, compile, debug, and emulate code for a wide range of Microchip devices. On the other hand, Arduino IDE is employed to program microcontroller-based boards such as Arduino.

- **User interface development**

Additionally, considering that the developed platforms are intended for end-user usage, it is necessary to implement the different user interfaces. In this case, two platforms through which users can interact with the sensors are smartphones and computers.

Android™ applications for the different smartphone-based sensor systems have been developed using the Android Studio IDE, while the graphical user interfaces (GUI) for PCs have been developed using Python.

2.5 Characterization and manufacturing equipment

- **Thermal and humidity measurements**

For temperature and humidity-controlled tests, the climate chamber VCL4006 (Vötsch Industrietechnik, Balingen-Frommern, Germany) was used (Figure 12). This equipment allows a temperature range from -40 °C to 180 °C in steps of 0.1 °C. Relative humidity can be set from 10% to 98%. The rate of change is 3.5 °C/min for heating and 5 °C/min for cooling.

Figure 12. *VCL4006 climate chamber.*

- **Semiconductor analyser**

Current–voltage characteristic curves of some devices were measured with the Semiconductor Analyzer B1500A (Keysight Technologies, Santa Clara, USA) (Figure 13). It provides exceptional precision in electrical measurements, with accuracy levels reaching as low as 0.1 femtoamps (fA) for current measurements, and 1 microvolt (μV) for voltage measurements. It offers high resolution, with the capability to measure currents as lo

w as 1 femtoampere (fA) and voltages as low as 100 nanovolts (nV). The analyzer boasts impressive repeatability, with deviations typically below 0.01% for both current and voltage measurements.

- **Power analyser**

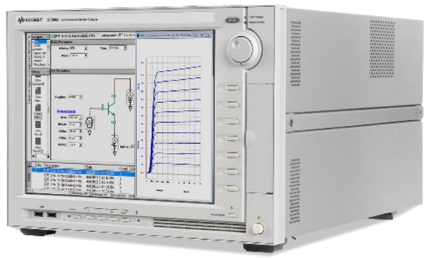

Figure 13. *Semiconductor Analyzer B1500A*

A DC Power Analyzer model N6705A (Keysight Technologies, see Figure 14) was used as a source/measure unit (SMU) to monitor the electrical consumption of the sensing platforms. This equipment combines the functions of a DC voltage source with the capability of an oscilloscope and data logger. It has four modules with the following specifications:

- Module 1: DC Power N6743B. 100 W output rating (20 V, 5 A).
- Module 2: DC Power N6746B. 100 W output rating (100 V, 1 A).
- Module 3: High-Perform N6751A. 50 W output rating (50 V, 5 A).
- Module 4: Precision N6761A. 50 W output rating (50 V, 1.5 A).

Figure 14. *DC Power Analyzer model N6705A*

- **Surface analyser**

The physical study, including the surface morphology and texture changes, was carried out using the 3D optical profilometer SNeox (Sensofar, Barcelona, Spain).

Figure 15. *Sensofar S neox 3D optical profilometer*

The Sensofar S neox 3D optical profilometer is an advanced metrology instrument designed for high-precision surface characterization across a wide range of applications. With sub-nanometer vertical resolution and rapid scanning capabilities, it offers precise and efficient measurement of surface topography and features. Combining confocal and interferometric imaging techniques, the S neox provides enhanced sensitivity and versatility, making it suitable for various sample types and surface properties. Its non-contact measurement approach ensures sample integrity, while automated measurement routines enhance productivity and reproducibility. The user-friendly software interface allows for easy setup, operation, and analysis of measurement data, facilitating streamlined workflows. Compatible with diverse sample sizes, shapes, and materials, the Sensofar S neox is a versatile solution for research, development, and quality control in industries such as semiconductor, automotive, and medical devices.

- **Precision LCR meter**

Figure 16. *LCR meter E4980AL.*

Capacitive measurements were performed with the LCR meter E4980AL (Keysight Tech., Santa Rosa, CA, USA). It is a precision impedance and capacitance meter, with a typical accuracy of up to 0.05% for impedance measurements, and 0.2% for capacitance measurements. It can operate at frequencies ranging from 20 Hz to 2 MHz, and its ability to perform automatic calibrations helps to maintain measurement accuracy over time, ensuring consistent quality results.

- **PCB prototyping**

Figure 17. *ProtoMat S100.*

For the prototyping of electronic systems on rigid substrates such as FR-4, the ProtoMat S100 (LPKF Laser & Electronics AG, Garbsen, Germany) was utilized (Figure 17). The ProtoMat S100 is a precision milling machine specifically designed for rapid prototyping of PCBs on various substrate materials, including FR-4. It offers precise positioning accuracy, typically within the range of ±5 microns (0.005 mm). This level of accuracy ensures that intricate PCB layouts and fine-pitch components can be accurately milled onto the substrate. The machine boasts fine resolution capabilities, with the ability to mill features and traces with a resolution as high as 0.1 mil (0.00254 mm). The ProtoMat S100 maintains tight tolerances on tool diameters, ensuring consistent milling performance. The machine supports a range of milling tools with diameters as small as 0.1 mm, allowing for precise milling of narrow traces and fine details.

- **3-D printing**

The Creality CR-X 3D printer (Creality, Shenzhen, China) is a versatile and user-friendly desktop additive manufacturing system. Featuring a dual-extrusion system, the CR-X allows for the simultaneous use of two different filaments or colours, enabling the creation of multi-material and multi-colour prints with ease. With a large build volume of 300 x 300 x 400 mm, it offers ample space for producing large-scale prototypes. This 3D printer was used for printing custom parts for the different platforms using Polylactic Acid (PLA) and Acrylonitrile Butadiene Styrene (ABS) filaments.

Figure 18. *Creality CR-X 3D printer.*

3 Results and Discussion

This chapter presents the results obtained during the research carried out. Three main sections focusing on the different lines of this research can be found with a detailed exposition of the developed microcontroller-based sensing platforms, followed by the results obtained by using them. Thus, we will begin with the dosimetry line, starting with the studies carried out to characterise the devices as radiation sensors. This extensive research was carried out during three short stays at the following institutions: the Centro Nacional de Aceleradores (CNA) in Seville, Spain; the Centro de Investigaciones Energéticas, Medioambientales y Tecnológicas (CIEMAT) in Madrid, Spain; and the Paul Scherrer Institute (PSI) in Villigen, Switzerland. In addition, the different irradiation sessions carried out at the Hospital Universitario Clínico San Cecilio are detailed.

Proceeding further, the application of the inertial measurement platform in the field of sports monitoring is discussed, especially the results obtained in the study of the time and height of vertical jumps using the sensor platform developed and the third publication of the compendium that delves into the development and application of an inertial measurement platform for the monitoring of skiing (sports research line).

Following this, the progress made on the capacitive platform and the corresponding tests conducted to evaluate its efficacy with it are presented. This section provides valuable insights into the functionality and potential applications of this technology.

At the end of each main section, the four publications that make up the thesis as a compendium of publications are included. These publications span diverse fields, reflecting the versatility of the microcontroller-based sensor platforms. In this way, the first two publications focus on the study of photodiodes under radiation typically used in radiotherapy treatments (dosimetry research line); the following publication delves into the development and application of an inertial measurement platform for skiing monitoring (sports research line); and the last publication details the development and testing of a capacitive sensor platform for real-time wireless monitoring of liquid wicking in a paper strip (microfluidics research line)

By organizing the outcomes of the thesis in this manner, we aim to offer a comprehensive overview of the results obtained, elucidating the multifaceted contributions of the conducted research endeavours.

3.1 Dosimetry

3.1.1 Dosimetric reader unit

In this section, the reader unit designed to measure the response of the photodiodes, diodes, and phototransistors under different sources of radiation is presented (Figure 19).

To control the bias of the DUTs a Digital to Analog Converter (DAC) DAC8552 (Texas Instruments, Dallas, TX, USA) was used. With this 16-bit, dual channel DAC and the electronic necessary to conditioning the output, we are able to obtain a bias voltage from -12 V to +12 V. The current-voltage converter is based on the operational amplifier TL072 (Texas Instruments, Dallas, TX, USA) with a feedback resistor of 4.7 MΩ. The output is low-pass filtered (with a parallel capacitor of 220 pF and a RC filter calculated to has a cut-off frequency at 16 Hz). After that, the 16-bit Analog to Digital Converter (ADC) ADS8326 (Texas Instruments, Dallas, TX, USA) was the model selected to be the interface between the output voltage and the microcontroller based on the excellent linearity and very low noise. Although the PIC18F46K42 (Microchip Technology Inc.) selected for the design, has an internal DAC (5-bit) and ADC (12-bit), the external components were used to enhance the performance of the reader unit. The PIC18F46K42 microcontroller, belonging to the PIC-18 family, that exhibits a suite of features tailored to meet the demands of diverse embedded applications. Built on a foundation of reliability and versatility, it serves as a cornerstone for projects requiring robust performance and seamless integration.

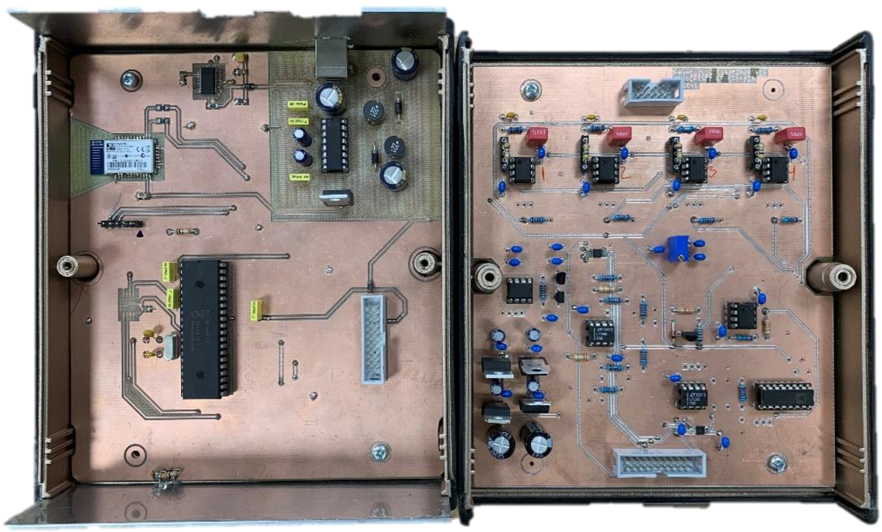

Figure 19. *Reader unit developed.*

Temperature is the major source of uncertainty in solid-state dosimetric devices, and especially in reverse currents where it can affect exponentially. Therefore, it is a critical parameter in our study due to the thermal dependence of the reverse dark current (Is) [87-90] which is the baseline of the radiation-induced photocurrent and the main contributor to its thermal drift. For this reason, the reader unit was provided with a sink current connected to one diode implemented with an LM334 using the Zero Temperature Coefficent Current Source configuration. It was configured to 35.58 ± 0.25 μA to forward bias the diode obtaining the forward voltage (Vγ), which is directly related to the diode temperature. In addition, a complete characterization of the sensors at different temperatures is mandatory to obtain the parameters for the thermal correction.

Therefore, this system can register the response of four devices at the same time and send directly to a PC via USB. This capability minimizes the time spent in irradiation facilities, reducing research costs. For this purpose, the analog multiplexer ADG408 (Analog Devices) was used. It has eight channels with one output allowing connect the four DUTs and the temperature sensor. Finally, in the microcontroller, a digital median filter is applied to reduce the noise of the measurements and it is sent to the PC thought a FTDI chip FT232R (Future Technology Devices International).

Central to the PIC18F46K42 is its powerful processing core, capable of executing complex instructions with precision and efficiency. This ensures smooth operation in demanding environments, making it well-suited for applications demanding real-time responsiveness and computational accuracy. The microcontroller offers a rich assortment of integrated peripherals, including multiple serial communication interfaces such as UART, SPI, and I2C. This facilitates seamless connectivity with a wide range of external devices and sensors, enabling efficient data exchange and system integration.

In terms of memory, the PIC18F46K42 provides ample resources for code storage and data manipulation. Its Flash memory capacity allows for storing application code and firmware updates, while its SRAM and EEPROM modules offer flexible options for temporary data storage and non-volatile parameter storage. Furthermore, the PIC18F46K42 is engineered with power efficiency in mind, featuring various power-saving modes and low-power operation capabilities. This makes it suitable for battery-powered and energy-conscious applications, extending battery life and minimizing overall power consumption. The microcontroller benefits from a comprehensive ecosystem of development tools and software libraries, facilitating rapid prototyping and streamlined application development. Its compatibility with industry-standard development environments and programming languages simplifies the development process, allowing developers to leverage existing resources effectively. In summary, the PIC18F46K42 microcontroller embodies the hallmark features of PIC microcontrollers, offering a potent combination of performance, reliability, and energy efficiency. Its robust design and versatile feature set make it an excellent choice for a wide range of embedded applications, from consumer electronics to industrial automation systems.

This system was used to characterise diodes, photodiodes and phototransistors as dosimetric sensors. Publications 1 and 2, as well as the other results presented below on these devices, were obtained with this reader unit.

3.1.2 Characterisation of commercial devices as radiation sensors

Next, the research conducted to characterise photodiodes, diodes, RADFETs, and LDRs under different ionizing radiation will be described. All tests were carried out in the facilities described in the methodology section 3.3.1 and the readout units previously described were used to measure the response of the devices. To make the reading more comprehensive, the results will be divided by device type.

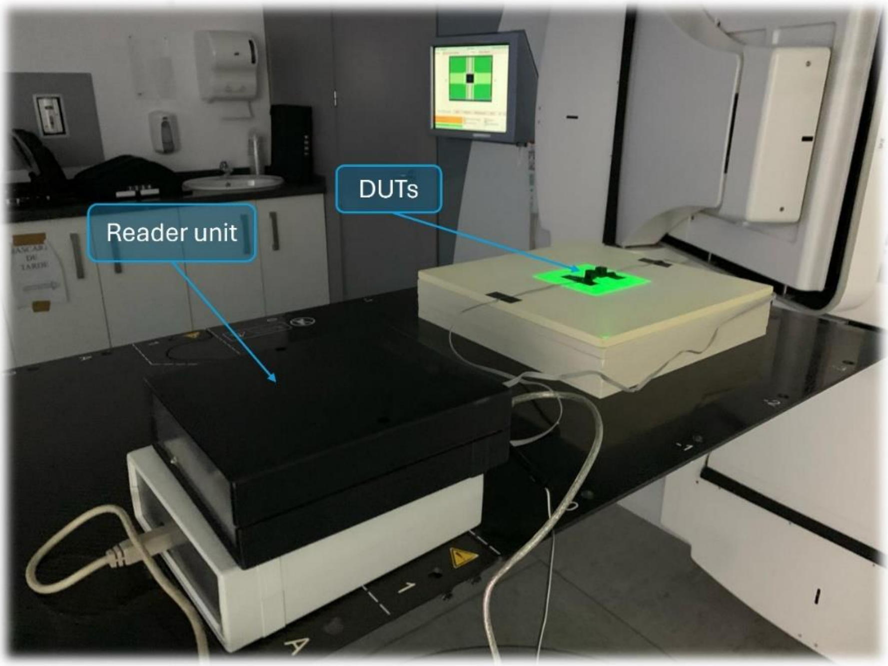

Figure 20. *Irradiation setup for the angular dependence study.*

3.1.2.1 Photodiodes as dosimetric sensors

3.1.2.1.1 Photon beam response

The characterisation of the best candidate dosimetric sensor by comparing three photodiodes and three phototransistors, as well as an in-depth study of the thermal dependence and how to correct it, can be found in publications 1 and 2, at the end of this section.

In addition to the previous described characterization, an angular dependence study of the BPW34S photodiode and the proposed solution based on a three-dimensional sensor will be presented. This study was carried out at the "Hospital Universitario Clinico San Cecilio". To increase the number of samples under characterization in each irradiation session, the reader unit was duplicated to perform the tests in parallel. Although the photodiode BPW34S has been studied in the present thesis as dosimetric sensor and the potential of the device will be presented in two of the publications part of the compendium, it is worth mentioning that it also presents some disadvantages.

First, an angular characterization of the individual model was performed. Irradiation tests were conducted with a linear accelerator (LINAC) Elekta Versa HD (Elekta Solutions AB, Stockholm, Sweden). The photon beam was produced with an electric potential of 6 MV. DUTs were located in the radiation isocenter (at 100 cm) and were irradiated with a field of 10x10 cm2 (see Figure 20). Fifteen irradiation sessions, at different incident angle, were programmed with an average dose rate of 6 Gy/min to provide an accumulate dose of 3 Gy (Si) per angle. The devices were irradiated from -180° to 180° in steps of 15°, obtaining a total accumulate dose of 45 Gy. Reference irradiation sessions at 0º were conducted every 9 Gy in order to minimize the degradation effect. However, the degradation must be taken into account for the calculation of angular dependency due to the sensitivity loss based on the accumulated

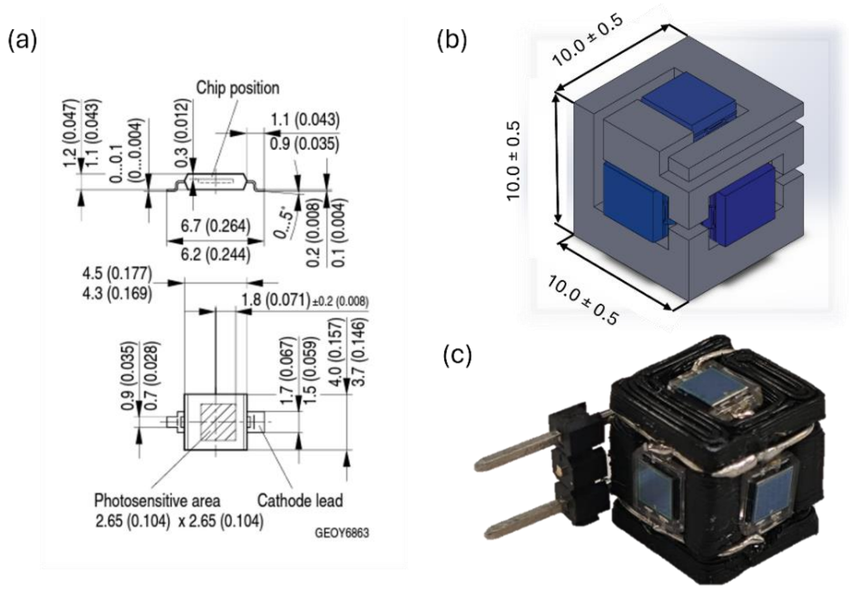

__Figure 21.__ BPW34S photodiode. (a) device dimensions; (b) design and dimensions of the 3D sensor; (c) real device. All the dimensions are in mm.

dose. It was found after 21.4 Gy for this device was bellow to 2% [93].

After that, a 3-D sensor was designed. A six-sided cube with a photodiode on each face was the proposed solution. All the photodiodes were connected in parallel, with this configuration, the current generated by each individual photodiode due to radiation will be combined with the current generated by each photodiode. The base on which the sensors rest was designed and fabricated with a 3-D printer using ABS (Acrylonitrile Butadiene Styrene). ABS is a popular material in 3D printing due to its strength, durability and good thermal resistance, making it suitable for a variety of applications. In addition, its ease of post-processing, wide colour availability, compatibility with acetone for a smooth finish, good mechanical properties, low cost, and a similar density to the water make it an attractive option. In Figure 21 a schematic with the dimensions of each sensor, the 3D design and the real sensor are shown.

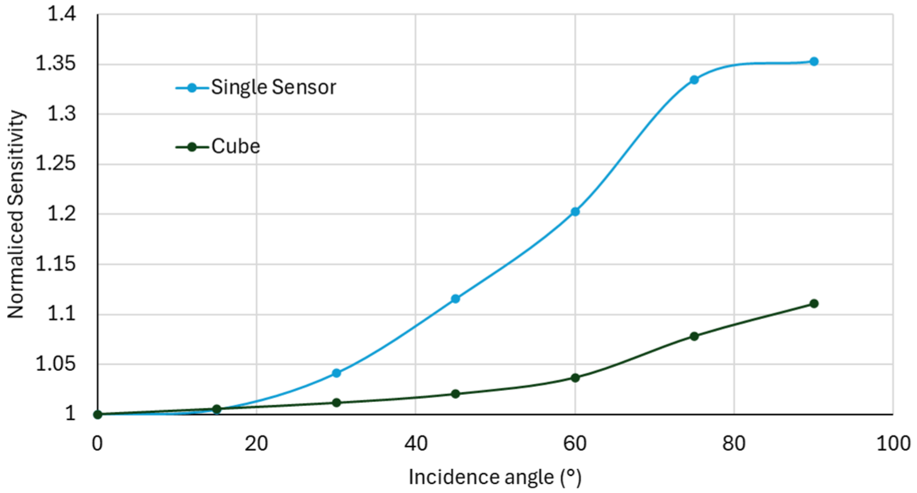

Figure 22. *Sensitivity obtained in the angle dependence tests for the devices tested. Comparison between single sensor and 3D sensor.*

Finally, a maximum sensitivity dependence of 35.3% was found for the induvial photodiode. In contrast, for the proposed sensor, this dependence was reduced to 10.6% (Figure 22).

3.1.2.1.2 Proton beam response

For the characterization of the BPW34S as a proton detector, it was tested under high and low energy proton beams. These tests were performed at the CNA (low energy) and at the PSI (high energy).

In this work the BPW34S photodiode was discarded as a sensor for low energy proton beams (up to 5.36 Mev) because it showed a lack of response. To check whether this was due to the depth of penetration of the protons into the coating material, the device was sanded and tested again, and this time a response to radiation was obtained. Even so, decapsulating the photodiodes for use was rejected, since the material they are made of is unknown and a repetitive method to perform this procedure was not achieved.

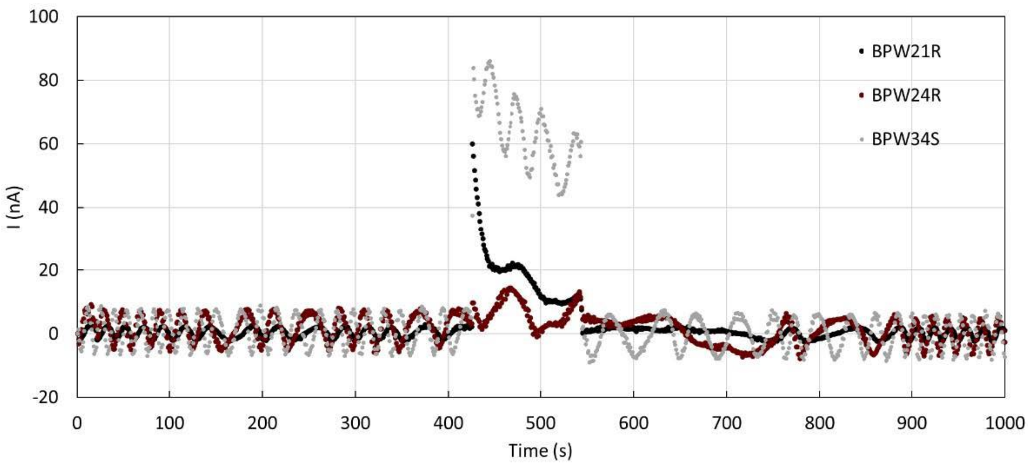

Figure 23. *Pre-irradiation study to choose the best dosimetric sensor among the photodiodes proposed.*

While the dosimetric parameter in the transistors is the threshold voltage shift, for photodiodes the radiation-induced photocurrent is related to the dose rate. Therefore, a real time measurement (continuously) was conducted every second and the current integration over the time was used to obtain the accumulated dose. Both, dose rate and total dose can be obtained from these devices. Finally, the radiation-induced current was used for diodes as a dosimetric parameter.

On the other hand, at the PSI the response of the different photodiode models (BPW21R, BPW24R, and BPW34S) was study at the highest energy available in PSI (230 MeV) to select the best candidate as dosimeter. To do it, preliminary irradiation sessions of 10 Gy were conducted. In Figure 23 a comparison of the response obtained from the three photodiodes tested is displayed. As it can be seen, the best candidate was the BPW34S due to its higher achieved photocurrent than the BPW21R and BPW24R. This model presents higher sensitivity and in addition less degradation with dose. Consequently, the candidate as radiation sensor for high energy proton beams was de BPW34S and the study was focused to its characterization.

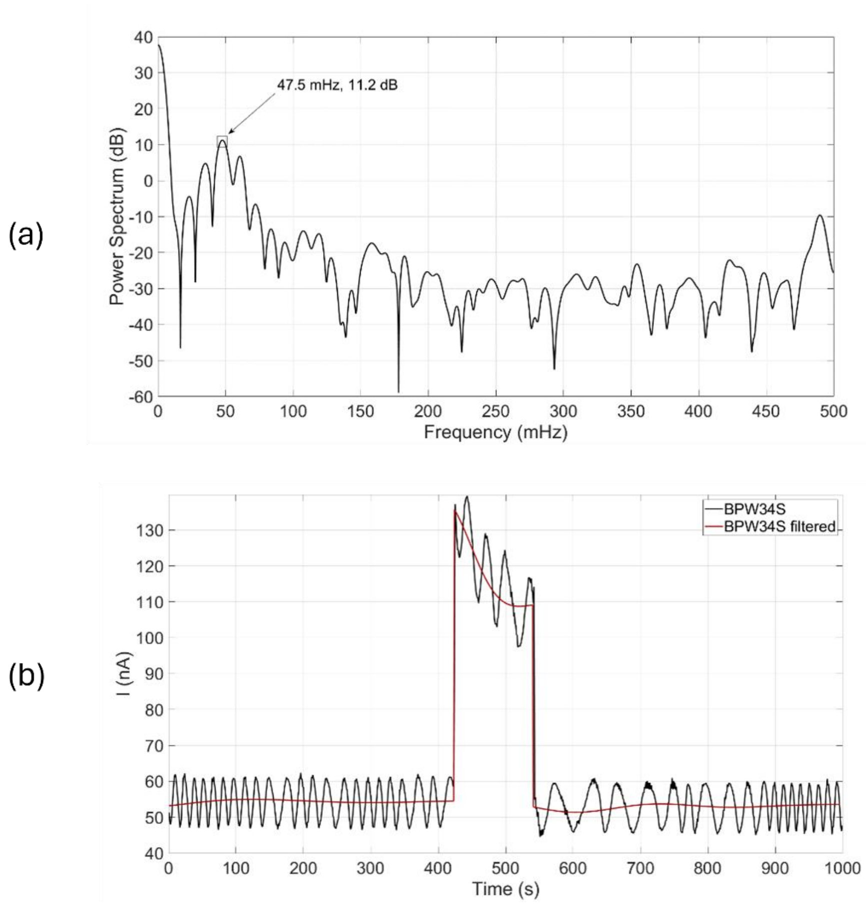

Figure 24. *(a) Signal Spectrum before applying LPF, and (b) Signal before and after filtering.*

Table 6. *Sensitivity obtained in function of the accumulated dose at three different energies for the photodiode BPW34S.*

<table>
<tr><th></th><th colspan="2">70 MeV</th><th colspan="2">150 MeV</th><th colspan="2">230 MeV</th></tr>
<tr><th>Accu. Dose (Gy)</th><th>S (nC/cGy)</th><th>SD (nC/cGy)</th><th>S (nC/cGy)</th><th>SD (nC/cGy)</th><th>S (nC/cGy)</th><th>SD (nC/cGy)</th></tr>
<tr><td>10.01</td><td>5.54</td><td>0.09</td><td>4.71</td><td>0.03</td><td>7.54</td><td>0.09</td></tr>
<tr><td>20.03</td><td>4.51</td><td>0.09</td><td>4.15</td><td>0.03</td><td>5.27</td><td>0.09</td></tr>
<tr><td>30.03</td><td>3.91</td><td>0.09</td><td>3.61</td><td>0.03</td><td>5.07</td><td>0.10</td></tr>
<tr><td>40.12</td><td>3.20</td><td>0.08</td><td rowspan="4">3.14</td><td rowspan="4">0.03</td><td rowspan="4">3.57</td><td rowspan="4">0.10</td></tr>
<tr><td>50.15</td><td>3.25</td><td>0.09</td></tr>
<tr><td>60.17</td><td>2.99</td><td>0.08</td></tr>
<tr><td>80.23</td><td rowspan="2">2.80</td><td rowspan="2">0.09</td></tr>
<tr><td>100.18</td><td rowspan="2">2.71</td><td rowspan="2">0.03</td><td rowspan="2">3.05</td><td rowspan="2">0.10</td></tr>
<tr><td>130.24</td><td>-</td><td>-</td></tr>
</table>

Table 6 shows the BPW34S response to radiation at proton beams of 70 MeV, 150 MeV, and 230 MeV. The zeroing process was preliminary undertaken in the initial instants, before starting the irradiation. Thus, the dark current is obtained as the average of the base line (averaged value of the current before the irradiation). To determinate the initial and the end of the irradiation the threshold current, I_{TH}, was set calculated as the dark current plus 3 standard deviations. In order to improve the measurement accuracy, the dark current was also registered between consecutive irradiation steps and at the end of the irradiation cycle. This dark current drift was removed from the total response for the final sensitivity calculations.

Also noteworthy is the noise that appears in the photocurrent output, increasing the uncertainty. The noise effect could be minimized with postprocessing the acquired signals. Using the Signal Analyzer tool in MATLAB the main noise component in frequency is located at 47.5 mHz (see Figure 24a). A low pass filter (LPF) would reduce the noise increasing the SNR, however the fast transient at the beginning and the end of irradiation would be smoothed. To avoid the smoothing, the LPF was applied in the three periods independently: pre-irradiation, irradiation, and post-irradiation periods. As an example, a comparison of filtered and original signal is displayed in Figure 24b.

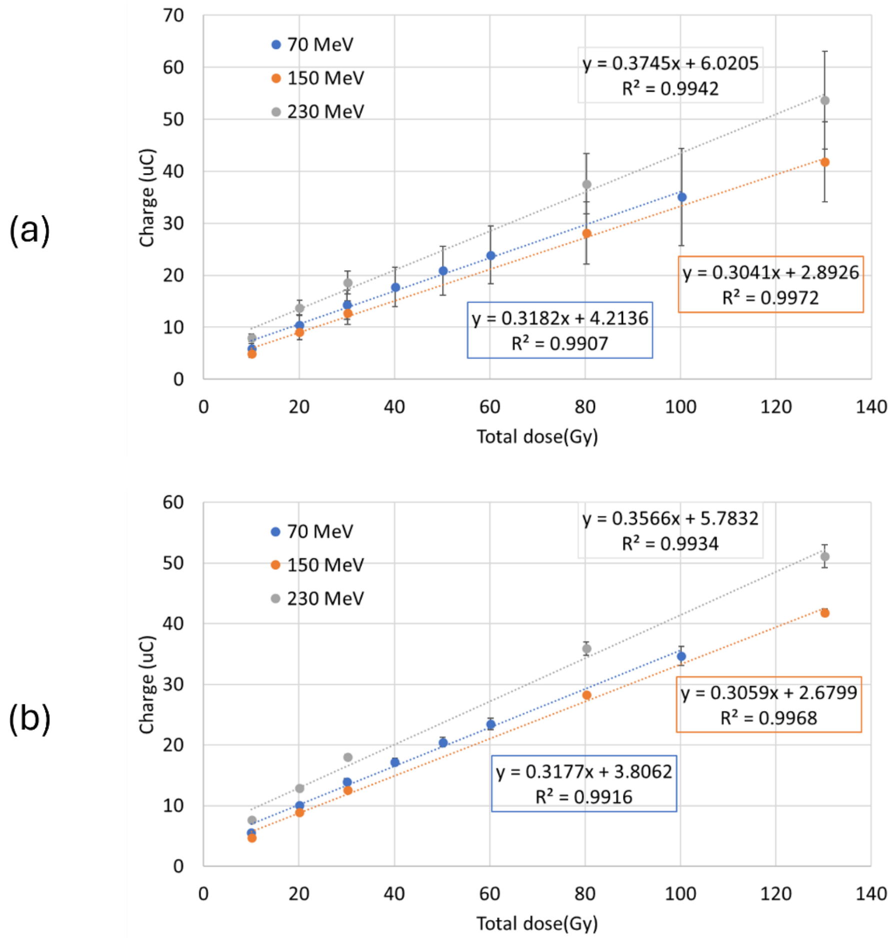

Figure 25. *Sensitivity of the BPW34S, calculated as the ratio between the charge generated by the ionizing radiation and the dose delivered per shot with three different energies. (a) results pre-filtering; (b) results after applying the filter.*

The sensitivity, calculated as the ratio between the charge generated by the ionizing radiation and the dose delivered per shot with three different energies can be found in Figure 25. The charge was obtained integrating the photocurrent that was determinate as the current during irradiation compensating the dark current drift (initial current before irradiation). These results have been calculated after applying the previously mentioned filter. A comparison between the charge obtained with the accumulated dose before (Figure 25a) and after (Figure 25b) applying the filter is shown.

Finally, the degradation was analysed after an accumulated dose of 30 Gy. At 230 MeV the degradation was the highest with a decreasing of 49% in sensitivity, following with the next energy studied, at 150 MeV the decrease in sensitivity was the lowest with 30% and with the last energy (70 MeV), the degradation was 42%. Figure 26 shows the response under 230 MeV proton beams after applying the digital filter. Only three runs are displayed, with this irradiation procedure, an accumulated dose of 30 Gy was applied (10 Gy per run). This image clearly shows the high degradation suffered by the device.

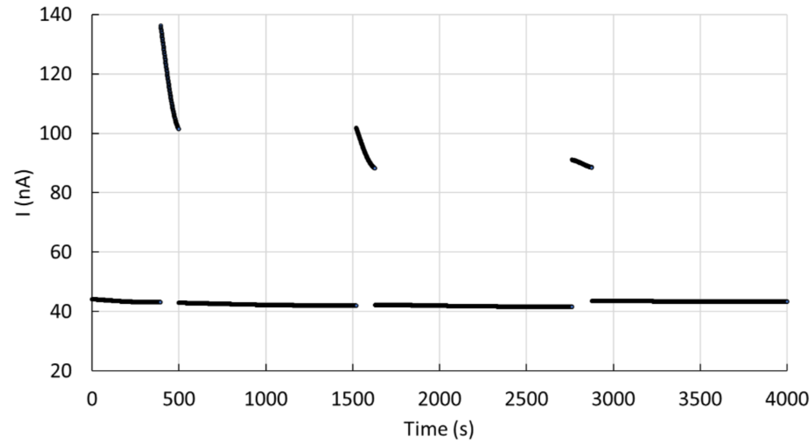

Figure 26. *BPW34S induced photo-current for 230 MeV proton beam after applying the digital filter designed.*

In conclusion, the BPW34S photodiode, although it has a high degradation under proton beams, its response is repetitive and could be used as a dosimetric sensor for this type of radiation as long as this degradation is modelled in depth. The experimental setup required a connection of 35 m with unshielded cable, that implied the used of amplified channel of the reader unit that includes a low pass filter to increase the SNR.

3.1.2.2 Diodes as high dose rate sensor

Continuing with the search of the best dosimetric sensor low-cost for different radiation beam, four models of commercial diodes were tested as high dose-rate sensors for gamma. Tests were also made with photon beams, but the sensitivity obtained was lower than that of photodiodes, so they were discarded for this type of radiation. Moreover, two of these devices (UF4007 and GP02-40) were also tested under high energy proton beam. The irradiation sessions under gamma beam were take place at CIEMAT and tests with protons were carried out at PSI. These proton tests served to discard the diodes as proton beam sensors as they were irradiated at 230 MeV and the response from the rectifier diodes studied was less than the noise power, therefore they were discarded, and we will focus on the characterisation of these devices under gamma beam.

For this research four PIN diode models with different breakdown voltages were used. UF4007 from On Semiconductor with a maximum reverse voltage (V_R) of 1000 V, 1N4007 from Vishay and V_R = 1000 V, GP02-40 from Vishay and V_R = 4000 V, and BY203 from Vishay and V_R = 2000 V. The sensitivity, repeatability, temperature during irradiations and degradation of each model were studied. Taking advantage of the fact that our reader unit has the possibility of reading the response of 4 dosimetric sensors and 1 temperature sensor in parallel, the irradiations were performed in such a way that each time the sample holder was opened, 4 devices of the same model and a fifth diode as a temperature sensor were placed. The complete irradiation setup can be seen in Figure 27.

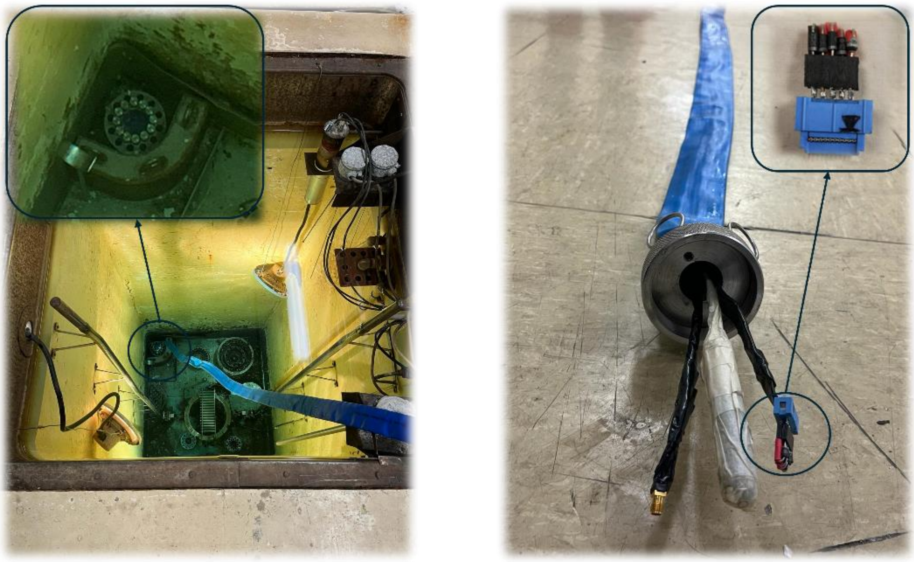

(a) (b)

Figure 27. *Setup for irradiation test at CIEMAT. (a) NAYADE facility. The samples are placed in the source, connected to the outside with the cable protected by the blue tube, in the detail you can see the distribution of the sources; (b) DUTs before closing the*

A preliminary characterization to select the bias voltage to obtain the highest sensitivity. For this purpose, one device per model was irradiated, during irradiation a bias voltage sweep from 0.5 V to -11 V was made. For this characterization the diodes were irradiated for 30 seconds at each bias voltage. Considering the dose rate was 365.17 Gy/min, 182.58 Gy were delivered to each device for each polarization voltage. Taking into account that eleven different voltages were studied, a total accumulated dose above 2 kGy per device was delivered.

As Figure 28 shows, the polarization voltage is directly related to the sensitivity of the devices. The data obtained confirm that this relationship is linear; therefore, for our study, the highest available reverse voltage in the reading unit (-11 V) was chosen. It is worth noting that greater sensitivity is expected if this polarization voltage is increased, but this has not been studied due to limitations of the reading unit.

After this preliminary characterization, the main study was performed. Four samples of each model were irradiated under the same conditions. All devices were exposed to a total accumulated dose of 22 kGy divided into short-duration irradiations. Additionally, the UF4007 was exposed to a total dose of 32 kGy. The total dose was divided into short exposure periods to study the recovery of the devices after each irradiation. Sensitivity was calculated as the collected charge per accumulated dose (μC/kGy) on average for the set of samples studied. To obtain the collected charge, the radiation induced current is integrated over the exposure time. In **¡Error! No se encuentra el origen de la referencia.**a, an example of one 1N4007 sample behaviour under the ionizing radiation can be seen. During the entire duration of the test, the dose rate remained constant. The decrease observed in the induced current is due to sensor degradation. This parameter will be analyzed later for each of the device models. Additionally, in **¡Error! No se encuentra el origen de la referencia.**b, a

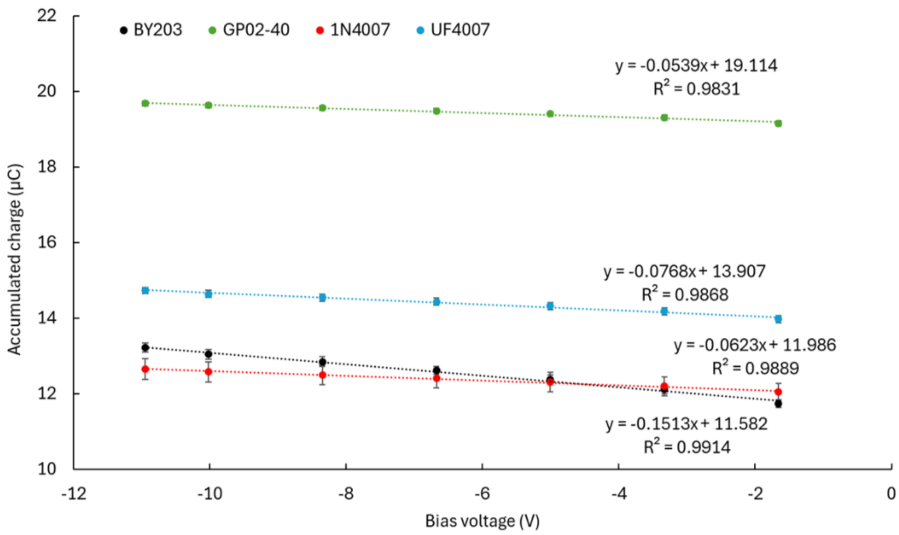

Figure 28. *Preliminary study. Polarization voltage sweep to select the one offering the highest sensitivity.*

summary of the sensitivity obtained for each diode model can be observed.

Degradation and temperature of the devices during irradiation were studied too. The sensitivity calculated is related to these two parameters. For the thermal study, a pre-characterization of the diode used as temperature sensor (UF4007) was made. To perform this characterisation, the VCL4006 climatic chamber was used. The value of forward voltage (V_F) was studied in the range of 50 to 0 Celsius degrees, this voltage is directly related to the temperature. Self-heating during irradiations will affect the current measured during the periods between irradiations, therefore, is very important to study the temperature of the devices. These periods correspond to the baseline that will be used to correct the dose measurements. The factors obtained from this characterization are displayed in Table 7. Once the parameters of the thermal dependence of the inverse voltage are obtained, it is possible to estimate the temperature reached by the diodes during irradiations.

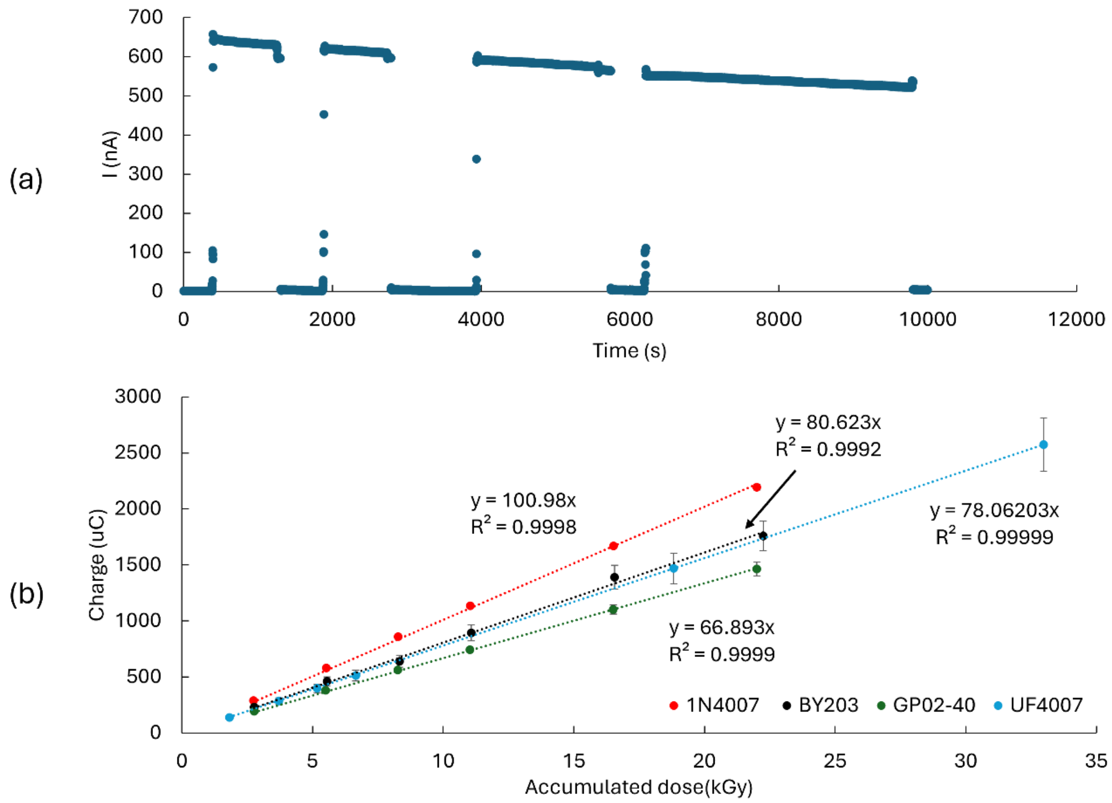

Figure 29. *(a) Response under the radiation for one sample of the diode model 1N4007. (b) Comparison of sensitivity obtained for the four models under study.*

Table 7. *Parameters of thermal characterization for diode UF4007*

	$m\ (mV)$	$n\ (mV)$
$y = m * x + n$	-2.17 ± 0.06	426.82 ± 1.38

After the main characterization, the thermal effect produced by the radiation on the devices was studied. Figure 30 shows how the temperature of the UF4007 diode increases from about 17 °C to 27 °C during a long irradiation. The periods between the red bars correspond to the irradiations. As it can be seen, the radiation induced current increases at the beginning of being exposed to radiation, stabilizing at the same time as the temperature does. This initial transient in the induced current during radiation exposure can be explained due to temperature increment. This drift can be minimized applying a post-processing to obtain the real dose.

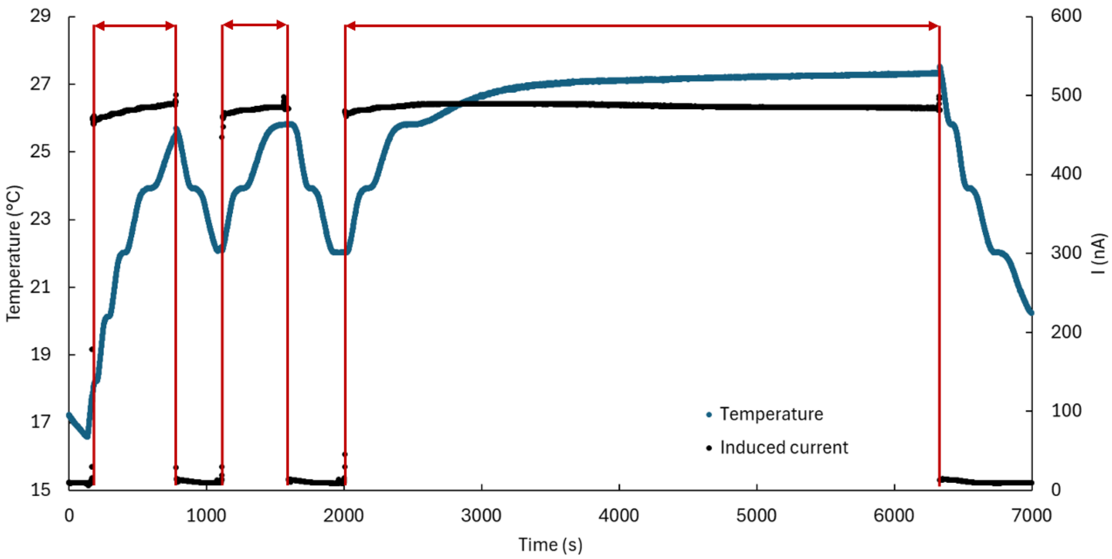

Figure 30. *Temperature of the UF4007 diode during 3 runs (blue dots) and the current induced by the radiation (black dots). The red bars delimit the periods during which the devices were irradiated.*

It should be noted that dose correction with temperature must be applied to obtain the correct sensibility and degradation, this will be done in future work. In the preliminary degradation study, degradation levels were found to be below 2% for all devices. These results were obtained using induced current collected data when the temperature was already stable to avoid the dependence found. Table 8 shows the degradation obtained in the diode models studied for a cumulative dose of 6.08 kGy and the sensitivity of the different device models.

Table 8. *Sensibility for a cumulative dose of 22 kGy and degradation for a cumulative dose of 6.08 kGy. The data used for the degradation study were chosen when the temperature was already stable to avoid errors due to the thermal dependence of the induced current.*

	Sensibility (µC/kGy)	*Degradation (%)*
1N4007	101.0 ± 0.7	1.4 ± 0.3
UF4007	78.06 ± 0.12	0.54 ± 0.04
BY203	80.6 ± 1.1	-0.13 ± 0.15
GP02-40	66.9 ± 0.3	0.0 ± 0.7

In conclusion, an in-depth study of the thermal dependence must be completed to correct the results obtained in this work. The data obtained without taking into account the dependence of the measured current on temperature show that all the diode models studied are candidates as dosimetric sensors for high dose rate gamma beams. The 1N4007 is the most sensitive but also shows the highest degradation. On the other hand, the BY203 and GP02-40 models, although they have lower sensitivity to radiation, the degradation they present is close to zero percent.

3.1.2.3 RADFETs as proton beams radiation sensor

In this section, the study of the RADFET VT06 from Varadis as dosimetric sensor for proton beam was conducted. This work was performed with low energy protons at the CNA and with high energy protons at the PSI. The degradation with cumulative dose and the dependence of sensitivity on energy were the parameters analysed. For this purpose, the reader unit previously developed in our research group [37] was used. As explained in previous chapters, in the case of MOSFETs and RADFETs the dosimetric parameter that is related to the cumulative dose is the increase of the threshold voltage.

First, to characterize the RADFETs at low energy, six runs of up to 200 Gy in Si were performed at energies of 1, 2, and 3 MeV. A printed circuit board (PCB) with three chips, two RADFETs per chip, were irradiated per energy. Therefore, six devices were irradiated simultaneously at the same energy. The RADFETS were assembled without lids to allow the proton beam to reach the sensitive material (silicon dioxide). The PCBs were placed into the irradiation chamber and connected with an external switcher that permits to connect sequentially the transistors one by one to the reader unit. Thus, up to six transistors can be read per irradiation session. The source voltage is measured biasing the transistor at I_{ZTC} current (17 μA). The measurement process consists of three phases:

1. Zeroing: The initial source voltage is recorded.
2. Irradiation: The devices were irradiated.
3. Measurement: The source voltage shift is measured and stored.

Five irradiation sessions were provided to reach a total irradiation dose higher than 210 Gy (218 Gy at 1 MeV; 217 Gy at 2 MeV; and 212 Gy at 3 MeV). After 15 hours, the source voltage was measured again to assess the fading effect.

On the other hand, for the high energy proton beam characterization at PSI, the experimental setup required a connection of 40 m with unshielded cable, that implied the used of amplified channel of the reader unit that includes a low pass filter to increase the SNR. Although in this case the amplified channel of the reader unit was used, the measurement process was the same as in the CNA. In this case, three chips, two RADFETs per chip, were irradiated per energy. Therefore, six devices were irradiated simultaneously at the same energy as well as in the study at low energies. Now, five runs of up to 130 Gy were performed at 151.23 and 230 MeV.

As conclusion of this study, the sensitivity showed an energy dependence around (0.122 ± 0.009) mV/(Gy*MeV) for low energies. The fading was evaluated recording during 165 hours after the last irradiation session, obtaining a decay of the source voltage of 3% for 1MeV and 6% for 3 MeV. Therefore a good stability of the dosimetric parameter was found. For high energies fading effect has not been studied because the irradiated samples became radioactive. Sensibility of the RADFET under different energies is show in Figure 31 and Table 9.

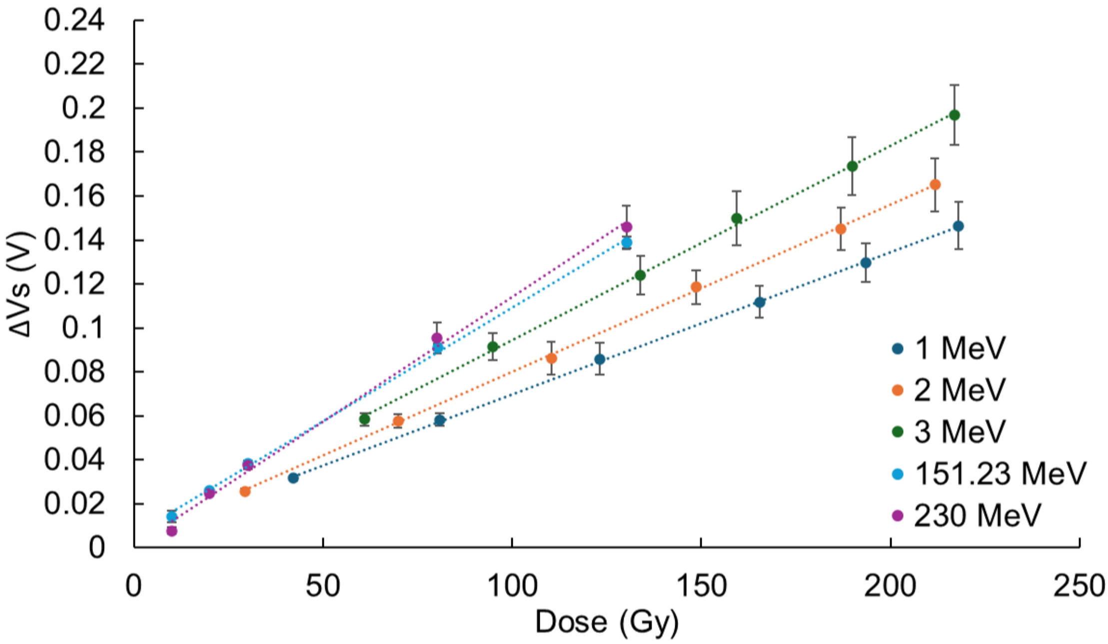

Figure 31. *Threshold voltage increase for the RADFET VT06 as a function of dose.*

In conclusion, the RADFET VT06 from Varadis shows a very suitable performance for high-dose measurements for different applications with low and high energy proton beams.

Table 9*. Sensibility obtained at different energies for the RADFET VT06 as proton beams sensor.*

Energy (MeV)	*Sensibility (mV/Gy)*
1	*0.679 ± 0.007*
2	*0.785 ± 0.006*
3	*0.922 ± 0.008*
151.23	*1.10 ± 0.03*
230	*1.143 ± 0.023*

3.1.2.4 Characterization of LDRs as photon beams dosimeters

A light-dependent resistor (LDR) (also called a photoresistor or photoconductive cell) is a light-controlled variable resistor whose resistance depends on the incident light intensity. It is a semiconductor device manufactured from compounds of CdSe, CdS, InSb or PbS [94]. When photons with energy higher than the semiconductor band gap are absorbed by the material, electron–hole pairs are generated both by band-to-band transitions and by transitions involving forbidden gap energy levels (also named trap levels). The resulting free charge carriers conduct electricity, thereby reducing the resistance. An LDR is typically applied in light-sensitive detector circuits and light-switching circuits. It is widely known that LDRs reduce their resistance with the increasing light intensity following a non-linear trend close to a 1/R dependence. A similar non-linear behaviour has been measured with dose rates under ionizing radiation as well [95]. In addition, if the radiation response of LDRs could be measured using a clinical electrometer such as those commonly used for reading ionizing chambers, the cost of the complete measurement system would be significantly reduced by removing the need for a specific reader system.

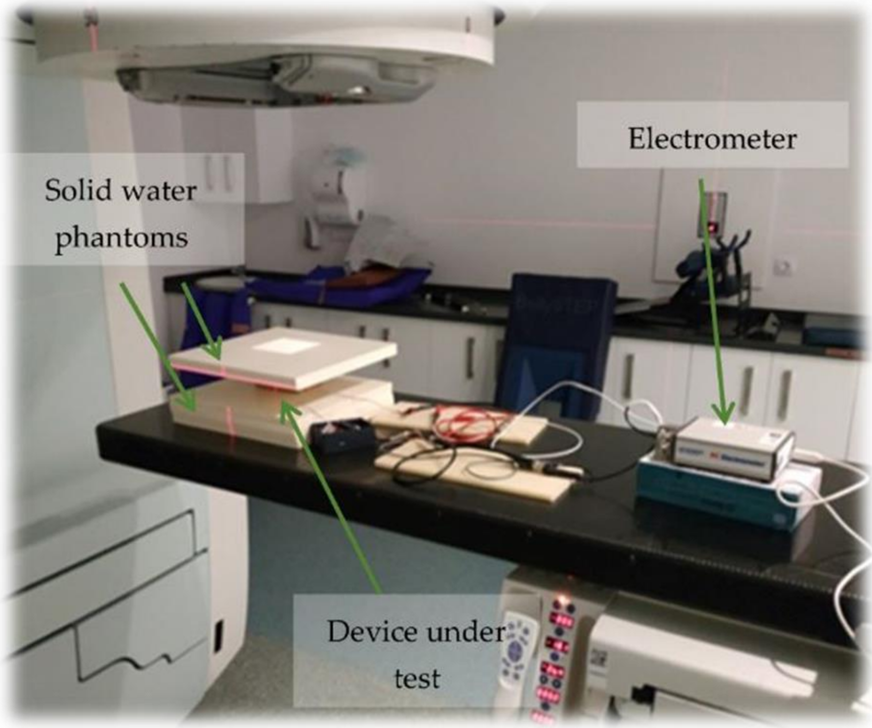

Figure 32*. Experimental setup for the characterization of the LDRs radiation response [99].*

Two commercial light-dependent resistor models have been characterized as dosimetric sensors for radiation X-ray beams typically used in radiotherapy. Three samples of each model have been studied. The experimental characterization included the measurement of their response to radiation in terms of resistance variation and current/charge generated under bias voltage. Moreover, LDR temperature dependence has also been analyzed as the main interferent with the goal of achieving thermal compensation of the measured parameters. The selected LDRs were the NSL-19M51 (Luna Optoelectronics, USA) and the VT43N2 (Excelitas Technologies, USA), both made of CdS, encapsulated in a moisture-resistant coating and enclosed in a plastic casing. Farmer-type ionization chamber PTW 30010 (PTW, Freiburg, Germany), very common in radiotherapy dosimetry, with a volume of 0.6 cm^3, was used as the reference dosimeter for benchmarking.

A clinical electrometer (PC Electrometer, Sun Nuclear, USA) was employed as the readout system, originally designed to operate with ionization chambers. The electrometer used can provide a bias voltage between –400 V and +400 V in steps of 1 V and has a measured current range up to 50 nA with a charge resolution of 15 fC. Irradiation sessions were carried out with a different linear accelerator, Artiste (Siemens AG, Germany). The LDRs were located at the isocenter of the radiation under solid water to reach electronic equilibrium. They were irradiated with a 6 MV X-ray beam and dose rates from 50 cGy/min to 300 cGy/min. The devices under test were also biased by the electrometer to study the effect of the bias voltage on their response to radiation. A TNC connector was employed to connect the LDRs to the electrometer and polarize the devices with voltages from 30 V to 150 V. The electrometer was placed inside the treatment room to reduce the noise produced by the wiring. It was controlled by a computer connected with a USB extension cable and placed out of the treatment room. Five solid water phantoms with a thickness of 1 cm each were placed under the box containing the LDRs, two more solid water phantoms over it to reach the electronic equilibrium conditions for 6 MV, as it is shown in Figure 32.

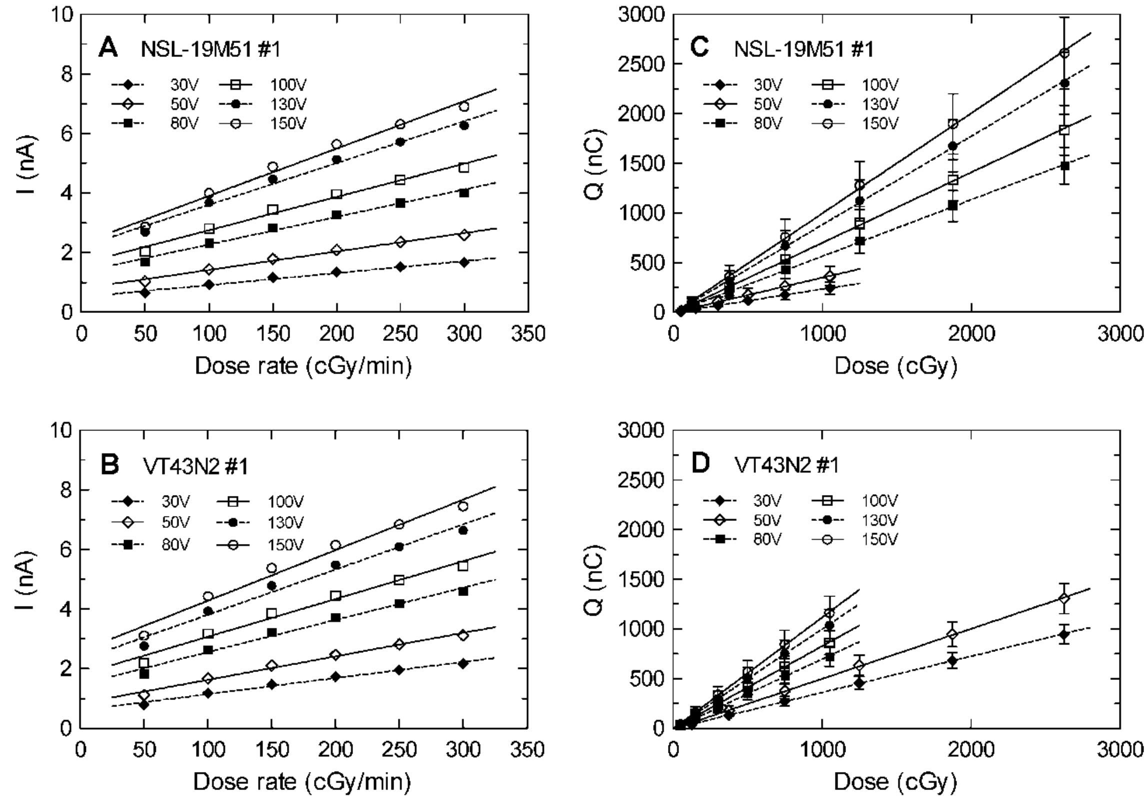

Figure 33. (A) and (B) Average steady-state current, ASC, versus dose rate; and (C) and (D) generated charge, CPI, versus accumulated dose for both models (NSL-19M51 number #1 and VT43N2 number #1) and with different bias voltages [99].

When incident X-rays fall on the LDR surface, carriers are generated either by band-to-band transitions or by transitions involving forbidden gap energy levels (also named trap levels), resulting in a conductivity increase. We have experimentally found that the initial amplitude of the response shows a peak. It increases with the polarization voltage and is different from one LDR device to another. This suggests that these peaks are due to generated carriers from trap levels. The peak decays are showing the emptying of these traps. When they are fully discharged, the steady-state current generated by band-to-band transitions remain. The peak amplitude dependence on the polarization voltage can be explained by the more efficient electron/hole separation before recombination at higher voltages than for the steady-state induced current.

Dose rate can be calculated from the average steady-state current (ASC), defined as the current increment from the base-line without irradiation to the steady-state value in the flat region during irradiation. In addition, accumulated dose can be extracted from the charge produced by irradiation (CPI) calculated as the time integral of the current in the irradiation period defined above. LDR sensitivity to radiation was defined as the ratio between the generated charge and absorbed dose in nC/cGy.

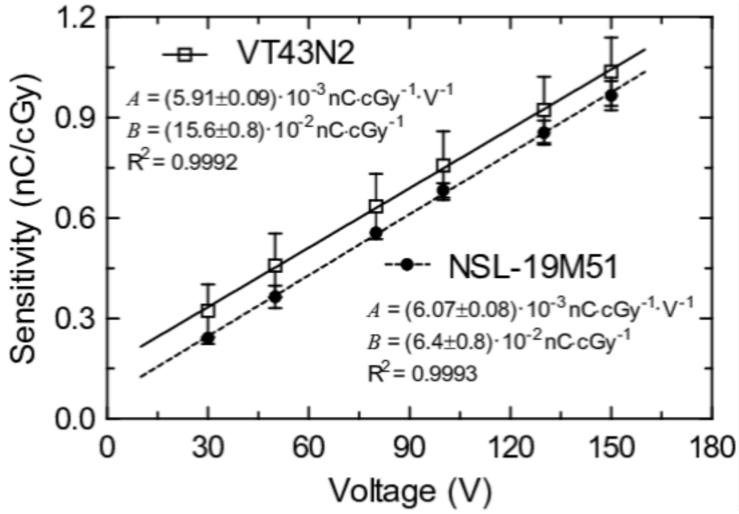

***Figure 34**. LDR sensitivity versus bias voltage for both studied models (NSL-19M51 number #1 and VT43N2 number #1). Experimental data are represented by symbols and linear trend lines (y = A·x + B) are also shown [99].*

Figure 33 shows the results of the average steady-state current and the dose rate at different bias voltages for the two LDRs under study. Higher slopes with the bias voltage are also observed. This can be explained due to a lower photocarrier recombination at higher voltages (higher electric field), allowing higher free carrier concentration and therefore a higher output current. In conclusion, Figure 34 depicts the dependences of the sensitivity with the bias voltage showing excellent linear behaviour. LDR devices presented a reproducibility error around 10%. However, their sensing areas are different. The sensing area of the VT43N2 model is bigger than the sensing area of the NSL-19M51, therefore it can provide a higher current with the same bias voltage.

3.1.3 Publication 1

Commercial photodiodes and phototransistors as dosimeters of photon beams for radiotherapy

Isidoro Ruiz-García[1,], Juan Román-Raya[2,], Jesús Banqueri[1], Alberto J. Palma[1], Damián Guirado[2,3,4], Miguel .A. Carvajal[1,*]

[1]ECSens, CITIC-UGR, Department of Electronics and Computer Technology. University of Granada, Granada, Spain

[2] San Cecilio Clinical University Hospital, Granada, Spain

[3]Instituto de Investigación Biosanitaria (ibs.GRANADA), Hospital Universitario Clínico San Cecilio Unidad de Radiofísica, Granada, Spain.

[4]CIBER de Epidemiología y Salud Pública (CIBERESP), Granada, Spain.

***Corresponding author**: Miguel A. Carvajal, carvajal@ugr.es

- Medical Physics, 2021, 48: 5440-5447. https://doi.org/10.1002/mp.14921
- Journal Impact Factor (2021): 4.506
- Rank by Journal Citation Indicator (JCI): Q1 in category *RADIOLOGY, NUCLEAR MEDICINE & MEDICAL IMAGING* (34/200)

Abstract

Purpose: The response to radiation typically used in radiotherapy treatments has been experimentally evaluated for three samples of two phototransistors (BPW85B and OP505A) and two PIN photodiodes types (VTB8440BH and BPW34S). *Methods:* To that end, a staggered irradiation cycle has been applied which included dose rate values from 0.81 to 4.87 cGy/s, achieving a total absorbed dose of 21.4 Gy. The samples have been irradiated with a linear accelerator and the relations between the induced photocurrent and the average and instantaneous dose rates, and between the accumulated charge and the absorbed dose, have been determined. The radiation-induced output currents were measured by means of an external interface of the devices to a previously designed readout unit. *Results:* Experimental results of Si PIN photodiode BPW34S have shown a sensitivity of (13.9 ± 0.5) nC/cGy, slight sensitivity dependence on dose rate, and a high linearity of the current with the average and instantaneous dose rate, requiring only 10 V of reverse bias voltage. This device thermal drift has characterized and modelled for temperature effect compensation. *Conclusions:* Silicon PIN photodiode BPW34S, previously tested for X-rays and Co-60 gamma ray source, can also be a reliable candidate for dose rate and absorbed skin dose determination in typical radiotherapy treatments irradiations. A low sensitivity loss below 2% up to 21.4 Gy has been measured, allowing its use as an affordable reusable skin dosimeter. Moreover, no significant difference has been observed between its response to dose-per-pulse and changing pulse repetition frequency in terms of sensitivity and dependence with dose-rate value.

Keywords: Radiation detectors, radiotherapy, optoelectronic devices, average/instantaneous dose rate

Introduction

Radiotherapy is one of the most common techniques to treat solid tumours. It is essential to ensure that the energy absorbed is enough to kill the tumour cells but does not exceed the threshold level to induce new damage in healthy tissues. Therefore, an accurate monitoring of delivered dose is mandatory in radiotherapy treatments. The most common dosimetric sensors are those providing current output such as ionization chambers, and dedicated silicon PN and PIN diodes, or threshold voltage shifts of MOSFET (Metal- Oxide-Semiconductor Field Effect Transistor) dosimeters. The ionizing radiation produces electron-hole pairs in their detection volume which are separated by an electric field. In the case of an ionization chamber, the electron-hole pairs are produced in the air volume content into the chamber, and the pairs are separated by an external high electric field between two metallic electrodes. Silicon diodes work in a similar way, but the main detection volume is the device depletion region. Now, electric field for charge separation can be internally (photovoltaic mode) or externally applied (photoconductive mode). The induced current is collected and usually measured with an electrometer. This current is proportional to the radiation dose rate, and the integration of the current over the exposure time gives the value of the accumulated charge that is proportional to the absorbed dose [1,2,3]. Both biasing and readout systems are provided by dedicated electrometers [4]. In the case of ionization chambers, high voltages, usually several hundred volts, are required to achieve enough sensitivity in the mentioned detectors. Commercial dosimetric systems based on diodes are always polarised at 0 V. Detectors and electrometers, although very reliable equipment, can be considered expensive items with costs well above several thousands of dollars depending on the model.

These limitations have been addressed by proposing the use of low-cost commercial optoelectronic detectors such as light-dependent resistors [5,6,7] and, considering current-mode devices, phototransistors and photodiodes, in some cases along with custom-made affordable readout systems [8]. Despite the vast majority of analysed detectors are silicon-based devices, diamond detectors and SiC Schottky diodes present good dosimetric performance as well [9,10,11,12,13,14]. At any rate, to provide a performance and reliability comparable to commercial dosimetry systems, these optoelectronic devices should have low dark current, show a high induced current when exposed to radiation (high sensitivity), low dose rate dependence, and low sensitivity decay with absorbed dose. In addition, other features which are suitable in radiation detectors are high reproducibility, low angular dependence, small sensitive volume, low energy dependence and equivalence to water, including the packaging device.

In fact, much work and notable results have been reported on the characterization of the response radiation of commercial phototransistors and photodiodes since pioneering in the last forty years[15,16]. Regarding commercial phototransistors, Dhole et al. have shown that the phototransistors can be used for measuring doses from 1 to 100 Gy under 1 MeV electron radiation. Collector current at various bias voltage levels between collector and emitter, for different fluences of electron irradiation, were measured and they observed a collector current decrease with increase of radiation dose delivered, i.e. radiation sensitivity degradation [15]. On the other hand, Santos et al. have analysed commercial phototransistors both for radiodiagnostic applications employing low energy X-ray radiation, as well as for radiotherapeutic applications utilizing high energy photon beams from linear accelerators [17,18,19,20,21]. They have shown that the phototransistors have stable sensitivity for low energy irradiation, but significant sensitivity degradation during high energy irradiation up to 100 Gy. More recently, only one type (BPW85B by Vishay) of four analysed phototransistors could be a suitable candidate for gamma radiation dosimetry employing Co-60 source, showing the highest current sensitivity, best linearity of the induced current with respect to dose rate and smallest performance degradation biased at relatively low voltage [22].

As for phototransistors, most research for commercial PIN photodiodes has consisted in studying their response under X-ray radiation for diagnostic radiology, reporting mostly stable response and suitable performance for dose rate and absorbed dose monitoring [23,24,25,26,27]. Commercial PIN photodiodes have also been analysed under gamma ray beams of Co-60 sources. Depending on the photodiode type, high linearity of radiation-induced current with dose rate has been measured up to 67 Gy/h [28], and low sensitivity degradation of 5% has also been observed for a high dose range, up to 15 kGy [29].

Current external radiotherapy treatments are usually applied with linear accelerators (LINACs). That is why, this work has been focused to analyse the response of several commercial phototransistors and PIN photodiodes in typical conditions of radiotherapy with this equipment. Irradiation cycles have been designed and applied to these selected devices aiming to encompass dose rate and absorbed dose values usually employed with LINACs in standard treatments. Different dose rates have been produced with the LINAC by two methods: i) average dose rate (ADR) by changing the pulse repetition frequency which is the procedure typically applied in LINAC-based external-beam radiation therapy, and ii) instantaneous dose rate (IDR, also referred as dose-per-pulse) by changing the source-surface distance (SSD)[30]. Moreover, our previously developed readout unit, initially intended for MOSFET-based dosimeters, has been redesigned for reading these current mode devices in real time [31]. Average dose rate linearity and sensitivity degradation have been studied for four types of optoelectronic devices, two PIN photodiodes and two NPN phototransistors, selecting the best suitable candidate according to these features. The response of the selected device will be compared for ADR and IDR. In addition, thermal drift of the selected device has been analysed for its possible use for compensation of the temperature effects on the dark current.

Materials and methods

2.1. Devices and irradiation setup

Four commercial optoelectronic device types have been characterized as radiation detectors for irradiations typically applied in radiotherapy treatments, two silicon photodiodes and two NPN phototransistors. Table 1 summarizes their main characteristics.

Table 1. Characteristics of the devices under test.

	Type	**Active area (mm^2)**	**Central wave lenght (nm)**	**Case**	**Manufacturer**
VTB8440BH	PIN photodiode	5.16	580	Case 21F Ceramic	Excelitas Technologies, Waltham, Massachusetts, USA
BPW34S	PIN photodiode	7.5	900	SMT DIL, Epoxy	Vishay, Malvern, Pennsylvania, USA
BPW85B	Phototransistor	--	850	T-1 plastic package	Vishay, Malvern, Pennsylvania, USA
OP505A	Phototransistor	--	850	T-1 plastic package	Optek, Essen, Germany

Three samples of each device under test (DUT) were irradiated with a linear accelerator (LINAC) Siemens Artiste (Siemens Healthcare GmbH, Erlangen, Germany), placed at the "Hospital Universitario Clínico San Cecilio" (Granada, Spain). The photon beam was produced with an electric potential of 6 MV. DUTs were located in the radiation isocentre (at 100 cm), and were irradiated with a field of 10x10 cm^2. To reach the electronic equilibrium, two solid water phantoms of 1 cm each were placed over the DUT. In addition five solid water phantoms were placed under the DUT, as Figure 1 shows. With these irradiation conditions, with regard to delivered dose, one monitor unit (MU) corresponds to 0.973 cGy (calibrated at 300 MU/min with a pulse duration of 3 μs and a pulse repetition frequency of 222 Hz). The constancy checks performed on the LINAC ensure that the absorbed dose per monitor unit varies less than 0.5% during the complete tests. With this initial irradiation setup, two experimental studies have been carried out to determine the device response with the average dose rate and the instantaneous dose rate respectively.

A Farmer-Type Ionization Chamber PTW 30010 (PTW, Freiburg, Germany) with a volume of 0.6 cm^3, was used as the reference dosimeter for benchmarking. The temperature of the treatment room was stabilized at 23ºC in all irradiation sessions. To shield from the ambient light, each DUT was painted with black nail polish and introduced into a black plastic box. The response to radiation of the devices under test was studied in terms of linearity, sensitivity, S (in nC/cGy), stability and reproducibility.

Average dose rate (ADR) study.

Varying LINAC pulse repetition frequency, dose rates of 50, 100, 150, 200, 250 and 300 MU/min (0.81 cGy/s, 1.62 cGy/s, 2.43 cGy/s, 3.24 cGy/s, 4.05 cGy/s and 4.87 cGy/s) were applied to characterize the response to radiation of the four DUT. To do that, a symmetrical staggered irradiation cycle was designed. The irradiation cycle of 90 minutes of duration is composed by two consecutive flights:

- A six-step decreasing ADR rate staircase from 4.87 to 0.81 cGy/s, and
- a six-step increasing ADR rate staircase from 0.81 to 4.87 cGy/s,

allowing to complete characterization in both raising and decreasing ADR. This irradiation cycle started at the highest dose rate value to provide an early pre-irradiation step in order to reduce the variability among samples. In all cases, each dose rate step duration was calculated to deliver a constant value of 200 MU. To deliver this accumulated dose, different time durations were required for each average dose rate, ranging from 40 to 240 s. With the sampling period of 2.15 s of our readout system, the uncertainties were calculated as the standard deviation over from 18 to 100 samples per average dose rate. The period unirradiated between each step was two minutes to baseline tracking which will be described in the next section. Moreover, DUTs were always biased at V_R = 10 V in accordance with a previous study[22].

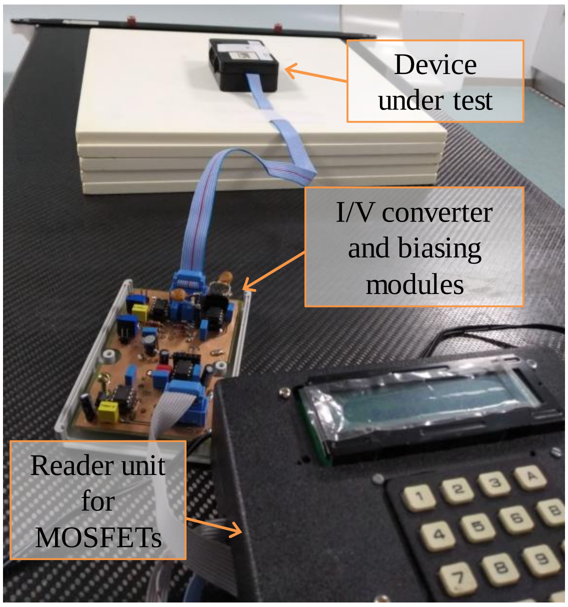

Figure 1. Experimental setup for DUT's current measurement, showing the device under test, the interface module, and the reader unit.

Instantaneous dose rate (IDR) study

Three replicas of the selected DUT as suitable dosimeter were irradiated. In this case, LINAC quality was configured with a dose-rate of 4.87 cGy/s (pulse repetition frequency corresponding to 300 Mu/min). SSD was changed from 95 to 236 cm in six different positions, obtaining an instantaneous dose-rate range from 5.5 to 0.92 cGy/s. Irradiation steps from high to low dose rates and from low to high dose rates were also applied.

2.2. Current conditioning interface

With the aim to keep wiring as short as possible to minimize electromagnetic interference on device's output current, the readout system was placed into the treatment room but out of the irradiation field (see Figure 1). This system was shielded by a 3 mm thick lead layer for radiation protection and connected to a computer, placed out of the treatment room, by an USB cable. The readout system consisted of two modules: an interface module between the DUT and our previously developed device reader extensively described elsewhere [31]. This ad hoc designed interface module accomplished two functions: i) To bias the DUT with a buffered voltage divider and, ii) to convert to voltage the device´s output current with a transimpedance amplifier based on the operational amplifier TL072 (Texas Instruments, Dallas, TX, USA) with a feedback resistor of 4.7 MΩ, see Figure 2. The output is low pass filtered (with a parallel capacitor of 220 pF) and level adapted to our reader unit input.

The biasing voltage, V_R = 10 V, was obtained from the output voltage of a DC-DC inverter based on the PWM controller MC3463 (Texas Instruments, USA). This module provided a voltage of -12 V that is divided, filtered and buffered with the operational amplifier LM358 (Texas Instruments, Dallas, TX, USA).

The reader unit previously developed is provided with a Sensor Front End (SFE) that is basically a Source Monitor Unit. SFE injects a drain current (I_D) to the input terminal and measures voltage (V_S), as shown in Figure 2. The current source was set at the minimum value (10 μA) and this intensity was absorbed by the operational amplifier without influence on voltage measurement. The source voltage (V_S) was digitalized with the 16- bit analog-to-digital converter ADS8320 (Texas Instruments, Dallas, TX, USA), achieving a resolution of 0.4 mV for the standard channel and 0.02 mV for the amplified channel. Taking into consideration that the feedback resistor was 4.7 MΩ in the interface module as current-voltage converter, the theoretical current resolution would be 80 pA. However, the circuital electronic noise avoids achieving this theoretical value. Therefore, continuous current measurements were carried out in the experimental conditions and the experimental uncertainty was calculated as two standard deviations, resulting in an experimental resolution current of 200 pA, enough for this study.

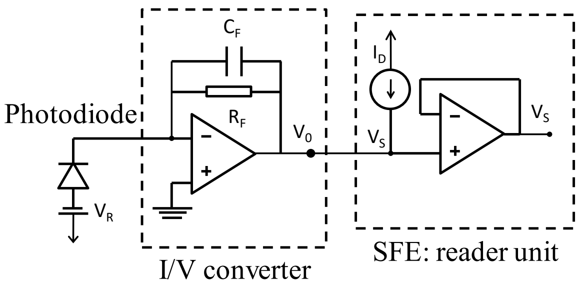

Figure 2. Scheme of current-voltage converter of the interface module and the Sensor Front End of the reader unit.

2.3. Thermal characterization setup

Temperature effect on electronic semiconductor devices is a well-known interference on their sensing applications. In this case, dark current thermal drift is rather significant. Therefore, the candidate to be used as dosimeter should be thermal characterized. In order to minimize the external electromagnetic interference, devices were introduced in a Faraday cage, and covered with aluminium foil during this experimental task. The semiconductor analyser B1500 (Agilent Technologies, Santa Clara, CA, USA) was used for devices biasing at V_R = 10 V and to measure the dark current. This instrument has a measurement range from 0.1 fA to 1 A, and from 0.5 μV to 200 V. Temperature sweeps from 15 to 50 ºC were conducted with a climatic chamber VCL4006 (Vötsch Industrietechnik, Balingen-Frommern, Germany), capable of varying the temperature from −40 to 180 ºC with a temperature deviation in time of ±0.3–1.0 K and a temperature homogeneity in space of ±0.5–2.0 K. To monitor the temperature more accurately, a digital thermometer RS 408-6109 (Amidata S.A., Madrid, Spain) with an accuracy of 0.1 ºC was placed inside the chamber close to the DUTs.

Results and discussion

3.1 Average dose rate study

The experiments carried out in the present study were aimed to study the sensitivity, linearity, stability, and reproducibility of the response of the DUT with average dose rate, aiming to select the best candidate among VTB8440BH, BPW34S, BPW85B and OP505A for the control of radiotherapy treatment irradiations. The degradation of the response with accumulated dose was evaluated as well, to study the possibility of avoiding a previous irradiation session before usage and to be suitable for high dose rate measurements and high accumulated doses, as it has been previously recommended [22].

According to the mentioned irradiation cycle, the current provided by the sample VTB8440BH#1 is displayed in Figure 3. The first maximum current (around 60 nA) corresponds to the first irradiation step with dose rate of 4.87 cGy/s, and the last maximum (around 50 nA) to the second irradiation at 4.87 cGy/s, showing a sensitivity drop around 17%. Therefore, with this experimental procedure the device degradation can be evaluated as well as its sensitivity.

The zeroing process was preliminary undertaken in the initial instants, before starting the irradiation, in the "base line calculation" zone (see Figure 3). In fact, the dark current is obtained as the average of the base line. The threshold current to effectively delimit the irradiation periods, I_{TH}, was set as this calculated dark current plus three standard deviations. In Figure 3, the different levels and experiment zone are displayed, and the threshold is displayed in the zoomed plot. In order to improve the measurement accuracy, the dark current was also registered between consecutive irradiation steps and at the end of the irradiation cycle, as Figure 3 shows.

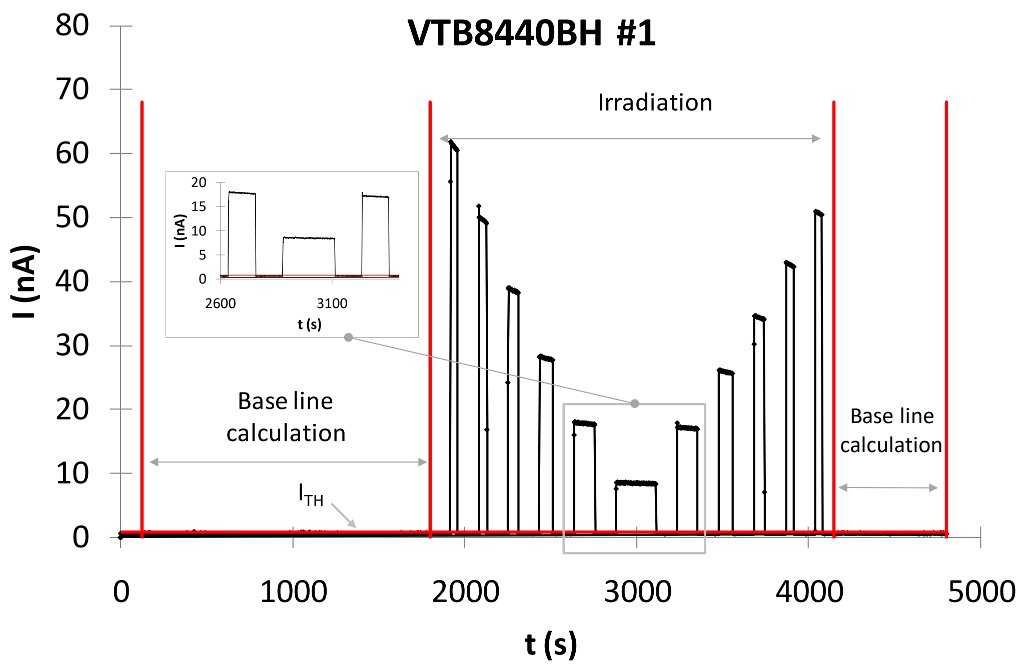

Figure 3. Measured current during the characterization of the sample number #1 of the model VTB8440BH showing the proposed complete irradiation cycle.

DUT linearity was evaluated by measuring the current during irradiation. The average value of the current was calculated during the irradiation periods, detected automatically as the periods when the photocurrent was higher than the defined current threshold, I_{TH}. The sensitivity was obtained as the slope of the linear fit with the dark current as the intercept. As it can be observed in Figure 4, the current produced by the irradiation is proportional to dose rate, as it was expected[22,27]. Due to their internal current amplification, phototransistors BPW85B and OP505A, presented higher sensitivity (slope of the linear fit) than photodiodes, VTB8440BH and BPW34S. Let us remember that the slope units are charge divided by dose, nC/cGy in this case.

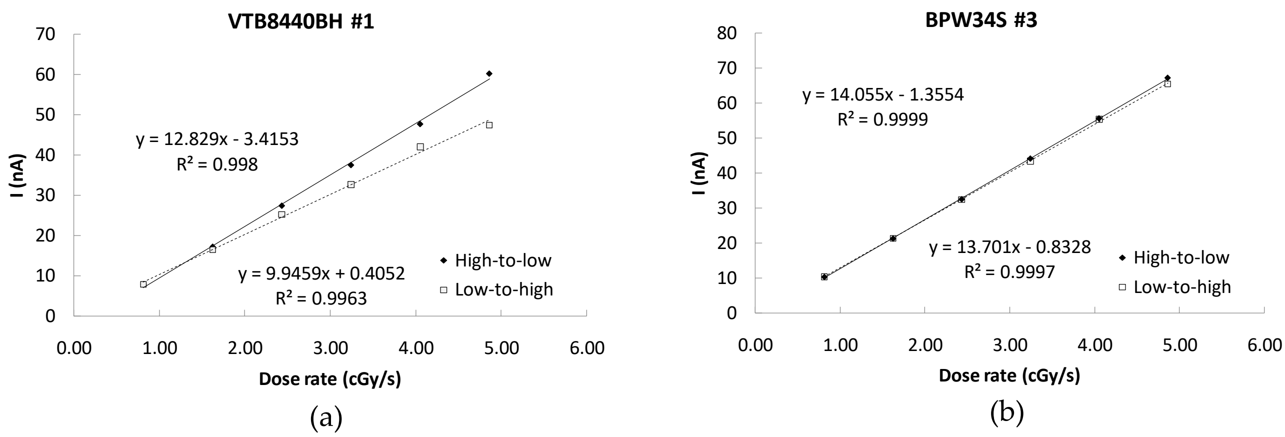

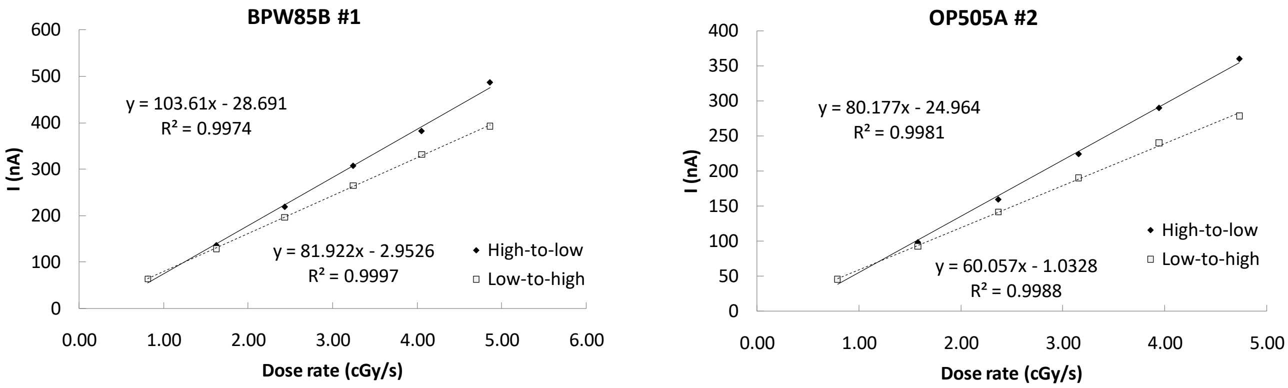

(c) (d)

Figure 4. ADR study: experimental results of the linearity study of one sample per analysed model. Solid symbols show the decreasing dose rate flight and empty symbols the rising one. Lines show the linear tendencies. Experimental data uncertainties are smaller than the symbols used to represent them (coverage factor k=1).

To determine the repeatability and stability of the sensor response, two different linear fittings were calculated, the first one from high to low dose rates (first flight of the irradiation cycle), and the second one from the decreasing dose rate stretch. Lower sensitivities have always been measured in the second case but with different trends depending on the device. Two different methods have been proposed to quantify such sensitivity loss: i) Method 1: the relative decreasing of both slopes in percentage as an average measure of the device performance degradation in the whole irradiation cycle, and ii) Method 2: to evaluate the degradation at one dose rate value, the collected charge at dose rate of 4.87 cGy/s at the beginning and at the end of the experiment was calculated as the time integration of the current during these two irradiation steps.

The results of these calculations for the four DUT models are summarized in Table 2. Firstly, due to low repeatability (high standard deviation) an individual calibration is required for an accurate dose determination. Secondly, according to the sensitivity loss due to accumulated dose, all studied models presented a degradation higher than 20% (calculated using both methods), with the exception of the silicon PIN photodiode BPW34S. For this model, sensitivity loss was below 2% in the dose range up to 21.4 Gy. Results of the analysed phototransistors are in good agreement with those previously reported [22].

Table 2. Average dose rate sensitivities, S_{ADR}, and their degradation with accumulated of the set of devices (three samples) ADR for the four DUTs. σ is the standard deviation among samples.

Model	Parameter	Mean	σ
OP505A	Slope high-to-low (nC/cGy)	64	21
	Slope low-to-high (nC/cGy)	48	20
	Degradation (method 1)	26.4%	10.9%
	SADR (nC/cGy) at 1.94 Gy	61	20
	SADR (nC/cGy) at 21.4 Gy	48	20
	Degradation (method 2)	24.3%	11.6%
BPW85B	Slope high-to-low (nC/cGy)	91	17
	Slope low-to-high (nC/cGy)	71	13
	Degradation (method 1)	21.9%	1.4%
	SADR (nC/cGy) at 1.94 Gy	91	19
	SADR (nC/cGy) at 21.4 Gy	70	15
	Degradation (method 2)	22.5%	2.9%
VTB8440BH	Slope high-to-low (nC/cGy)	12.86	0.10
	Slope low-to-high (nC/cGy)	10.17	0.21
	Degradation (method 1)	21.0%	1.3%
	SADR (nC/cGy) at 1.94 Gy	12.3	0.3
	SADR (nC/cGy) at 21.4 Gy	9.6	0.9
	Degradation (method 2)	21.5%	8.2%
BPW34S	Slope high-to-low (nC/cGy)	14.0	0.1
	Slope low-to-high (nC/cGy)	13.9	0.2
	Degradation (method 1)	1.1%	1.6%
	SADR (nC/cGy) at 1.94 Gy	13.8	0.4
	SADR (nC/cGy) at 21.4 Gy	13.8	0.1
	Degradation (method 2)	0.2%	2.7%

As a result, the BPW34S PIN photodiode was selected as the candidate dosimeter due to its very low sensitivity degradation with the absorbed dose. This good performance has also been reported for this device under Co-60 gamma rays and X-rays for radiodiagnosis [28,24,25,26,27]. In fact, an average sensitivity can be calculated, obtaining S_{ADR} = 13.8 ± 0.4 nC/cGy (coverage factor k=1). This value is similar to around 17 nC/cGy previously reported under Co-60 gamma rays with lower dose rates from 1.86 to 0.026 cGy/s [28]. Different measured sensitivity can be attributed to the higher energy of the X-ray beam of our experiment [3].

Instantaneous dose rate study

In order to extend the characterization of the BPW34S as dosimeter, its response to IDR was analysed. Three unirradiated BPW34S samples (named #P1, #P2 and #P3) were irradiated obtaining an average sensitivity, S_{IDR} = 14.0 ± 0.4 nC/cGy, which is in close agreement with the value obtained in the ADR study. For comparison purposes, the ionization chamber PTW 30010, with a volume of 0.6 cm^3, provides an average sensitivity of 0.2 nC/cGy biased at 400 V. Figure 5 presents one example of measured diode currents from low to high and from high to low dose rates, showing high similarity with Figure 4. A combined average sensitivity, S_{avg}, from ADR and IDR studies can be calculated with samples #1, #2, #3; and, #P1, #P2, and #P3, obtaining S_{avg} = 13.9 ± 0.5 nC/cGy. With this uncertainty, an individual sample calibration would be mandatory for accurate dosimetry.

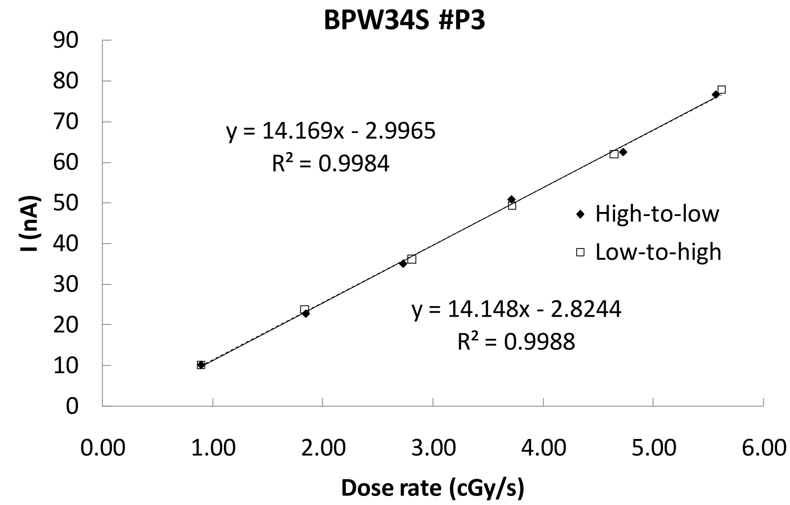

Figure 5. BPW34S #P#3 response versus instantaneous dose rate from high to low IDR (solid symbols) and from low to high IDR (empty symbols). Lines show the linear tendencies. Experimental data uncertainties are smaller than the symbols used to represent them (coverage factor k=1).

In Figure 6, the influence of the dose rate value on the sensitivity for ADR and IDR studies is compared. An increasing sensitivity versus dose rate was measured for both studies, showing similar trends. At 0.81 cGy/s S_{ADR} is an 85% of its value at 4.87 cGy/s. This relative difference is equal between sensitivities of the lowest and the highest IDR. This behaviour has been extensively observed and modelled for the response of this kind of devices to both, instantaneous[32,33,34] and average dose rate[35]. Recently, a kinetic model of diode detector response to pulsed radiation beams has been reported, claiming that this behaviour can be properly modelled whatever the method to generate dose rate variations[36]. In few words, the sensitivity increase has been explained for the decrease of recombination rate of radiation-induced minority charge due to the saturation of the recombination centre at higher dose rates[32]. According to our results, the comparative experimental data of Figure 6 demonstrated that PIN diode BPW34S shows light differences between methods IDR and ADR in terms of average sensitivity with the dose rates typically applied in external-beam radiation therapy.

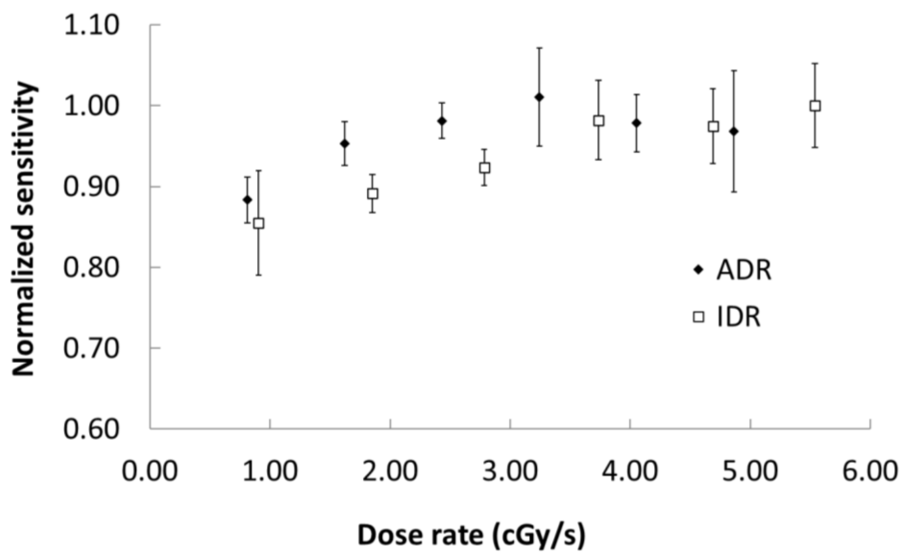

Figure 6. Normalized average sensitivity versus dose rate of BPW34S: ADR with solid symbols and IDR with empty symbols. Uncertainties represent the standard deviation of the three samples per set.

Influence of the temperature

Regarding the thermal effects on detector performance, the dark current in photodiodes depends exponentially on temperature, therefore, base line will be strongly affected by the temperature in dose rate and absorbed dose measurements. In the present work, all dose measurements were carried out at constant temperature, however, if this were not the case, a thermal compensation should be mandatory. To quantify it, a thermal characterization of the dark current was carried out for three unirradiated samples (#T1, #T2, #T3) biased at V_R = 10 V from 15 to 50 ºC of the selected PIN photodiode BPW34S. As shown in Figure 7, an exponential dependence was found, resulting in an average dark current, Iavg, at 25 ºC of 17 ± 3 nA. This value is in agreement with that provided by the manufacturer at V_R = 10 V and T = 25 ºC of 2 nA and a maximum value of 30 nA [37]. The error bars in Figure 7 represent the standard deviation (k =1) of the three samples under study. The high uncertainty found at 10ºC can be explain as follows: At low temperatures the dark current is extremely low, therefore the relative effect of ambient light interference is much higher than other temperatures. The behaviour of the three samples was similar, and the fit of average currents, Iavg, with temperature was calculated obtaining a slope of m = (0.61 ± 0.04) log(nA)/ºC and an intercept n = (-0.25 ± 0.13) log(nA) (Figure 7). Therefore the thermal drift of the dark current at 10 V can be modelled as I (T) = 10^ [m·T+n].

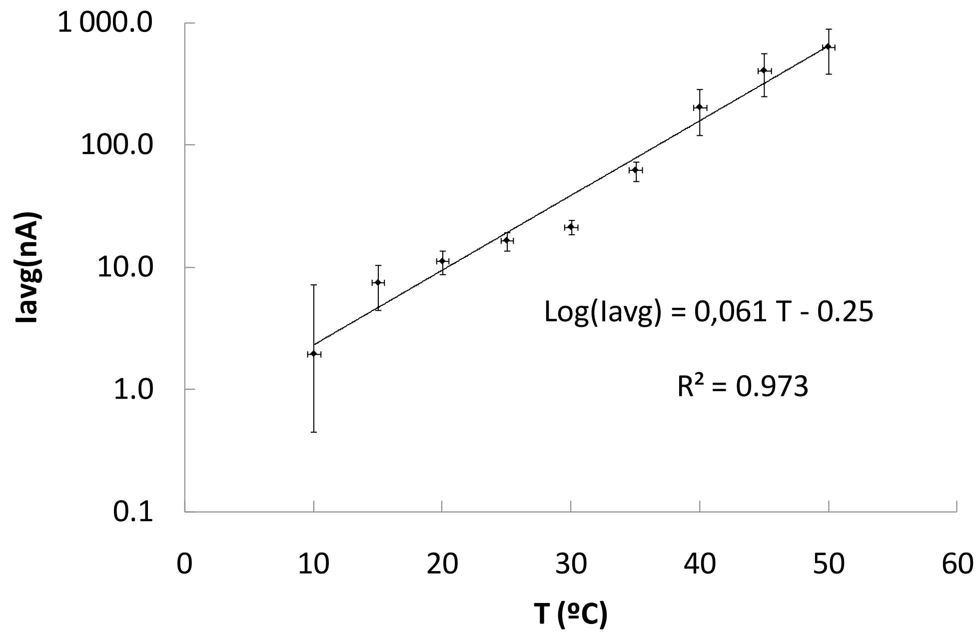

Figure 7. Experimental results of the thermal characterization: Average experimental data of the set of three transistors (coverage factor k=1).

Conclusions

The response to radiation of two commercial photodiodes (VTB8440BH and BPW34S) and two phototransistors types (OP505A and BPW85B) has been evaluated in typical conditions of current radiotherapy treatments. A custom-made reader has also been proposed adapting a previously developed readout system for MOSFET dosimeters. All devices showed a very good linearity of the radiation-induced current with the average dose rate. However, sensitivity degradation higher than 20% was found for all types when the maximum analysed absorbed dose (21.4 Gy), except for the PIN photodiode BPW34S. Therefore, this model has been selected as a suitable candidate to be used as dosimetric sensor. Sensitivity dependences with the average and instantaneous dose rate were analysed, resulting in lower sensitivity at low dose rate values. A sensitivity reduction of 15% was found for the lowest dose rate irradiation session with respect to the sensitivity achieved at the highest dose rate irradiation session. Average sensitivity of (13.9 ± 0.5) nC/cGy with a bias reverse voltage of 10 V was measured showing no significant difference with average (ADR) or instantaneous dose rate (IDR). Moreover, the sensitivity loss due to accumulated dose was below 2% up to 21.4 Gy. Given all this features, this device is suitable for being used as a low-cost and reusable skin dosimeter for radiotherapy treatments.

Acknowledgments

This research has been partially funded by Junta de Andalucía (Spain), projects numbers PI-0505-2017 and FEDER/Junta de Andalucía-Consejería de Economía y Conocimiento Project B-TIC-468-UGR18.

References

1. Knoll GF. *Radiation Detection and Measurement*. 3rd Ed. John Wiley & Sons, Inc; 2000.

2. Barthe J. Electronic dosimeters based on solid state detectors. *Nucl Instruments Methods Phys Res Sect B Beam Interact with Mater Atoms*. 2001;184(1-2):158-189. doi:10.1016/S0168-583X(01)00711-X

3. Rosenfeld AB. Electronic dosimetry in radiation therapy. *Radiat Meas*. 2006;41(SUPPL. 1):134-153. doi:10.1016/j.radmeas.2007.01.005

4. Mather SJ, Mansi L. IAEA Technical Report Series. *Eur J Nucl Med Mol Imaging*. 2008;35(5):1030-1031. doi:10.1007/s00259-008-0767-4

5. Deev IS. The Use of Cadmium Sulphide Photo-Conductors in Radiation Dosimetry. *J Nucl Energy Part B React Technol*. 1960;1(3):204-210. doi:10.1016/s0368-3273(15)30029-8

6. Soliman FAS, Ashry HA. Radiation effects on non-linear resistances. *J Mater Sci Mater Electron*. 1993;4(4):293-300. doi:10.1007/BF00179227

7. Román-Raya J, Ruiz-García I, Escobedo P, Palma AJ, Guirado D, Carvajal MA. Light-dependent resistors as dosimetric sensors in radiotherapy. *Sensors (Switzerland)*. 2020;20(6):1568. doi:10.3390/s20061568

8. Damulira E, Yusoff MNS, Omar AF, Taib NHM. A review: Photonic devices used for dosimetry in medical radiation. *Sensors (Switzerland)*. 2019;19(10):1-28. doi:10.3390/s19102226

9. Bertuccio G, Puglisi D, Macera D, Di Liberto R, Lamborizio M, Mantovani L. Silicon carbide detectors for in vivo dosimetry. *IEEE Trans Nucl Sci*. 2014;61(2):961-966. doi:10.1109/TNS.2014.2307957

10. Trettnak W, Kolle C, Reininger F, Dolezal C, O'Leary P, Binot RA. Optical oxygen sensor instrumentation based on the detection of luminescence lifetime. *Instrum Monit Control Celss*. 1999;22(10):1465-1474. isi:000079454700009.

11. Metzger S, Henschel H, Köh O, Lennartz W. Silicon carbide radiation detector for harsh environments. *Proc Eur Conf Radiat its Eff Components Syst RADECS*. 2002;1(2):51-56. doi:10.1109/radecs.2001.1159258

12. Pini S, Bruzzi M, Bucciolini M, et al. High-bandgap semiconductor dosimeters for radiotherapy applications. *Nucl Instruments Methods Phys Res Sect A Accel Spectrometers, Detect Assoc Equip*. 2003;514(1-3):135-140. doi:10.1016/j.nima.2003.08.095

13. Marczewska B, Nowak T, Olko P, et al. Synthetic diamonds as active detectors of ionising radiation. *Diam Relat Mater*. 2004;13(4-8):918-922. doi:10.1016/j.diamond.2003.09.010

14. Spadaro S, Conte G, Pimpinella M, Guerra AS. Electrical and dosimetric characterization of a CVD diamond detector with high sensitivity. *Radiat Meas*. 2013;48(1):1-6. doi:10.1016/j.radmeas.2012.11.017

15. Dhole SD, Bhoraskar VN. *Use of Phototransistor as a Radiation Monitor*. United States; 1994. http://inis.iaea.org/search/search.aspx?orig_q=RN:26046948.

16. Lanza JJ, Mauderli W, Fitzgerald L, Roessler G. AN AUTOMATED DOSIMETRY SYSTEM FOR COMPUTED TOMOGRAPHY X-RAY SCANNERS USING SILICON P-I-N DIODES.: P/63. *Health Phys*. 1980;39(6). https://journals.lww.com/health-

physics/Fulltext/1980/12000/AN_AUTOMATED_DOSIMETRY_SYSTEM_FOR_COMPUTED.85.aspx.

17. Santos LAP, da Silva EF, Vilela E. Filtered X ray beam dosimetry from 10(-3) to 10(2) Gy dose range by using phototransistors. *Radiat Prot Dosimetry*. 2002;101(1-4):145-148. isi:000178899900027.

18. Santos LAP, Barros FR, Filho JA, da Silva EF. Precise dose evaluation using a commercial phototransistor as a radiation detector. *Radiat Prot Dosimetry*. 2006;120(1-4):60-63. doi:10.1093/rpd/nci608

19. Santos LAP, Magalhães CMS, Silva JO, Filho JA, Silva EF, Santos WM. A feasibility study of a phototransistor for the dosimetry of computerized tomography and stereotactic radiosurgery beams. *Radiat Meas*. 2008;43(2-6):904-907. doi:10.1016/j.radmeas.2007.11.065

20. Magalhães CMS, Sobrinho ML, Souza DN, Filho JA, Da Silva EF, Santos LAP. A novel dosimetry system for computed tomography using phototransistor. *Radiat Meas*. 2012;47(1):30-33. doi:10.1016/j.radmeas.2011.10.014

21. Paschoal CMM, Souza DN, Santos LAP. Characterization of three photodetector types for computed tomography dosimetry. *World Acad Sci Eng Technol*. 2011;80(8):92-95.

22. Andjelković MS, Ristić GS. Current mode response of phototransistors to gamma radiation. *Radiat Meas*. 2015;75:29-38. doi:10.1016/j.radmeas.2015.03.005

23. Romei C, Di Fulvio A, Traino CA, Ciolini R, d'Errico F. Characterization of a low-cost PIN photodiode for dosimetry in diagnostic radiology. *Phys Medica*. 2015;31(1):112-116. doi:10.1016/j.ejmp.2014.11.001

24. Oliveira CNP, Khoury HJ, Santos EJP. PiN photodiode performance comparison for dosimetry in radiology applications. *Phys Medica*. 2016;32(12):1495-1501. doi:10.1016/j.ejmp.2016.10.018

25. Paschoal CMM, Ferreira FCL, Souza DN, Santos LAP. Comparison of dose measurements in CT using a photodiode and a small ion chamber. *Radiat Meas*. 2016;91:50-53. doi:10.1016/j.radmeas.2016.05.002

26. Nazififard M, Suh KY, Mahmoudieh A. Experimental analysis of a novel and low-cost pin photodiode dosimetry system for diagnostic radiology. *Rev Sci Instrum*. 2016;87(7). doi:10.1063/1.4955170

27. Santos EJP, Oliveira CNP, Khoury HJ. Energy and air kerma dependence of response of a photodiode-based dosimetric system for radioprotection. *Radiat Meas*. 2019;122(November 2018):73-79. doi:10.1016/j.radmeas.2019.01.017

28. Andjelković MS, Ristić GS. Feasibility study of a current mode gamma radiation dosimeter based on a commercial PIN photodiode and a custom made auto-ranging electrometer. *Nucl Technol Radiat Prot*. 2013;28(1):73-83. doi:10.2298NTRP/1301073A

29. Goncalves JAC, Mangiarotti A, Bueno CC. Current response stability of a commercial PIN photodiode for low dose radiation processing applications. *Radiat Phys Chem*. 2020;167(April 2019):108276. doi:10.1016/j.radphyschem.2019.04.026

30. Rosenfeld AB, Biasi G, Petasecca M, Lerch MLF, Villani G, Feygelman V. Semiconductor dosimetry in modern external-beam radiation therapy. *Phys Med Biol*. 2020;65(16). doi:10.1088/1361-6560/aba163

31. Carvajal MA, Martínez-García MS, Guirado D, Banqueri J, Palma AJ. Dose verification system based on MOS transistor for real-time measurement. *Sensors Actuators, A Phys*. 2016;247. doi:10.1016/j.sna.2016.06.009

32. Shi J, Simon WE, Zhu TC. Modeling the instantaneous dose rate dependence of radiation diode detectors. *Med Phys*. 2003;30(9):2509-2519. doi:10.1118/1.1602171

33. Saini AS, Zhu TC. Dose rate and SDD dependence of commercially available diode detectors. *Med Phys*. 2004;31(4):914-924. doi:10.1118/1.1650563

34. Jursinic P. PIN diodes for radiation therapy use: Their construction, characterization, and implementation. *Phys Medica*. 2019;59(February):86-91. doi:10.1016/j.ejmp.2019.02.021

35. Jursinic PA. Dependence of diode sensitivity on the pulse rate of delivered radiation. *Med Phys*. 2013;40(2):1-9. doi:10.1118/1.4788763

36. Neira S, Brualla-Gónzalez L, Prieto-Pena J, Gómez F, Pardo-Montero J. A kinetic model of diode detector response to pulsed radiation beams. *Phys Med Biol*. 2019;64(20). doi:10.1088/1361-6560/ab4460

37. Semiconductors V. Vishay Semiconductors Silicon PIN Photodiode , RoHS Compliant TEST CONDITION SYMBOL Silicon PIN Photodiode , RoHS Compliant SYMBOL. 2002:386-390.

3.1.4 Publication 2

Thermal Drift Reduction in Photodiode Dosimeters with Switching Bias

I. Ruiz-García[1], J. Román-Raya[2], P. Escobedo[1], M. Andjelkovic[3], D. Guirado[4,5], A.J. Palma[1], M.A. Carvajal[1,*]

[1] *ECsens, Department of Electronics and Computer Technology, Sport and Health University Research Institute (iMUDS-UGR), Research Centre for Information and Communications Technologies (CITIC-UGR), University of Granada, 18071 Granada, Spain; isirg@ugr.es; ajpalma@ugr.es; pabloescobedo@ugr.es; carvajal@ugr.es*

[2] *Instituto de Investigación Biosanitaria, ibs.Granada. Hospital Universitario Virgen de las Nieves, Granada, Spain; juan.roman.raya.sspa@juntadeandalucia.es*

[3] *IHP – Leibniz-Institute für innovative Mikroelektronik, Frankfurt (Oder), Germany; andjelkovic@ihp-microelectronics.com*

[4] *Instituto de Investigación Biosanitaria, ibs.Granada. Hospital Universitario Clínico San Cecilio, Granada, Spain; dguirado@ugr.es*

[5] *CIBER de Epidemiología y Salud Pública (CIBERESP), Granada, Spain*

* *Corresponding author: Miguel Ángel Carvajal-Rodríguez (carvajal@ugr.es)*

- Measurement, Volume 199, 2022, 111538, ISSN 0263-2241. https://doi.org/10.1016/j.measurement.2022.111538
- Journal Impact Factor (2022): 5.6
- Rank by Journal Citation Indicator (JCI): Q1 in category INSTRUMENTS & INSTRUMENTATION (9/63)

Abstract

The effect of temperature on dosimetric measurements is a major limitation of solid-state dosimeters. This is especially true for PIN photodiode dosimeters, where the dark current depends exponentially on temperature. To minimize this effect, a compensation method is presented that relies on the diode structure itself without the need for an external sensor or device. During irradiation, the photodiode is periodically switched from reverse to forward polarization to determine the temperature of the device. This measurement is based on the linear dependence between the temperature and the forward voltage of the diode when it is operated at constant current. An electronic circuit implementing this procedure was developed and used for experimental characterization of the response to radiation of the BPW34S Si PIN photodiode. The proposed procedure reduced the uncertainty due to thermal drift by a factor of 7.5. In addition, an average dose rate sensitivity of 12 ± 2 nC/cGy was measured, with a sensitivity degradation below 2% for the irradiation cycle of 21.4 Gy performed under a 6 MV photon beam. We have shown that a p-n junction can be successfully used to compensate for the temperature effect on the dosimetric measurement.

Keywords: PIN Photodiode, dosimeter, thermal compensation, forward voltage.

Introduction

Radiotherapy is one of the most common and effective treatments for solid cancers. In radiotherapy, it is essential to adequately determine the absorbed dose to ensure a proper tumour cells damage while preserving healthy cells as much as possible. Ionization chambers are the most commonly used devices for radiotherapy dosimetry. The ionization chamber is connected to an electrometer both to apply the required electric field by means of a bias voltage and also to measure the charge induced by the radiation, integrating the current. This system presents some limitations compared to semiconductor-based systems, such as comparatively higher cost, larger size, and high voltage requirement for biasing. As an alternative or complement, some current-mode semiconductor devices have been studied for the same purpose, such as photodiodes and phototransistors [1–3]. Silicon diodes work in a similar way as ionization chambers. In this case, the detection volume is the depletion region, and it can operate in two different modes: photovoltaic mode, when the electric field for charge separation is internal, or photoconductive mode, when an electric field is externally applied. The induced photocurrent is usually measured with an external electrometer as well. This magnitude can be related to the radiation dose rate, and the absorbed dose is proportional to the integral of the current over the exposure time [4–6].

Some authors have proposed the use of low-cost commercial optoelectronic detectors such as light-dependent resistors (LDR) as dosimetry detectors [7–9]. The LDR operation is based on the resistivity change due to the generation of electron-hole pairs as a result of the absorption of photons. Other devices used in radiotherapy, particularly for in vivo dosimetry, are MOSFETs (metal-oxide-semiconductor field effect transistors). MOSFETs offer several advantages for dosimetry applications, such as immediate and non-destructive readouts, low power consumption, easy calibration, and reasonable sensitivity and reproducibility [10–13]. Because the sensitivity of MOSFET dosimeters in the unbiased mode is low, and at high dose rates the linearity of their response is reduced, efforts to increase the sensitivity of MOSFET dosimeters have involved their manufacture with a special technological process to achieve a thick gate oxide (more than 200 nm). The resulting devices are known as RADFETs (Radiation Field Effect Transistor) [14–16].

However, semiconductor-based systems generally present an important limitation due to their temperature dependence, hindering an accurate dose measurement. This issue has been tackled by some authors in different solid-state dosimeters. For thermal correction in RADFETs, different strategies have been described. The most direct one is to set it at the bias point with the minimum temperature coefficient, in the so-called drain current condition, I_{ZTC} [17]. Another thermal compensation method is based on differential measurements of the source–drain voltage of two identical MOSFETs. These transistors are biased using the same current during readout but irradiated at different gate–source voltages. Consequently, they have different sensitivities to radiation, which produces different source–drain voltage shifts. Nevertheless, thermal fluctuation is the same in the two transistors and the difference is minimized by applying a differential measurement [18]. Another strategy was proposed using a custom read-out system applying two or three drain currents to the same RADFET [19]. Furthermore, the same authors developed a thermal compensation technique using the parasitic diode for DMOS transistor dosimeters [20].

In this work, based on a similar idea to the one used for thermal compensation of DMOS transistors, a PIN photodiode is thermally studied, and a thermal compensation method is hereby presented and applied. Our proposal consists in periodically measuring the forward voltage (V_F) as a method to measure the temperature of the device. This value is employed for the thermal correction of the reverse dark current (I_S), which is the baseline of the radiation-induced photocurrent and the main contributor to its thermal drift. Therefore, as a prerequisite, the temperature dependence of both the forward voltage [21–24] and the photodiode dark current must be accurately characterised. In short, the PIN photodiode will be forward biased for temperature measurement mode, and reverse biased for dose rate determination mode. Moreover, a thermal compensated read-out unit has been redesigned to implement the proposed procedure [25].

Materials and methods

PIN photodiode BPW34S (Vishay, Malvern, Pennsylvania, USA) was selected as the dosimetric sensor. The reason for this choice was that this optoelectronic device has already been characterised as radiation detector for irradiations typically applied in radiotherapy treatments, showing a promising response in terms of sensitivity and reproducibility [3,26]. Two experimental characterizations were conducted: (i) a complete modelling of the dependence with the temperature in reverse (dark current) and under forward biasing, and (ii) its response to ionizing radiation in reverse biasing. In both cases, each device under test (DUT) was painted with black nail polish and, in addition, they were placed into a box to shield it from environmental light.

A total of eleven samples were employed for the thermal characterization. Six samples were divided in two groups of three devices. One group was used for the thermal modelling of forward biased DUT at constant current, and the other for the validation of the proposed model. Moreover, thermal dependence of the dark current under reverse biasing was measured in five samples. For temperature-controlled tests, samples were placed inside a climate chamber VCL4006 (Vötsch Industrietechnik, Balingen-Frommern, Germany). To monitor the temperature more accurately, a digital thermometer RS 408-6109 (Amidata S.A., Madrid, Spain) with an accuracy of 0.1 °C was placed inside the chamber close to the photodiodes. To minimize the infrared radiation produced by the chamber while heating, the photodiodes box was also covered with aluminium foil. Then, current-voltage characteristic curves were measured at different temperatures with the Semiconductor Analyzer B1500A (Agilent Technologies, Santa Clara, USA). To perform the thermal characterization, temperature sweeps from 10 to 35 °C in steps of 5 °C were conducted, and the photodiodes were forward biased in the range from 0 to 2 mA by the Semiconductor Analyser.

In the second step, the dosimetric characterization of the photodiodes was performed. Eight samples of the BPW34S were irradiated with a linear accelerator (LINAC) Siemens Artiste (Siemens Healthcare GmbH, Erlangen, Germany), placed at the "Hospital Universitario Clínico San Cecilio" (Granada, Spain). The photon beam was produced with an electric potential of 6 MV. DUTs were located in the radiation isocenter (at 100 cm away from the source) and were irradiated with a field size of 10x10 cm^2. To achieve the electronic equilibrium, two solid water phantoms of 1 cm each were placed over the DUT. In addition, five solid water phantoms were placed under the DUT, as Figure 1 shows. The majority of radiation detectors, including PIN photodiodes, measure the energy inside the volume of matter by the charge created inside it. That is the reason why a suitable measurement must be done with the detector in electronic equilibrium condition, where the charge entering the volume by external process would be approximately equal to the loss of charge created by internal process [4].

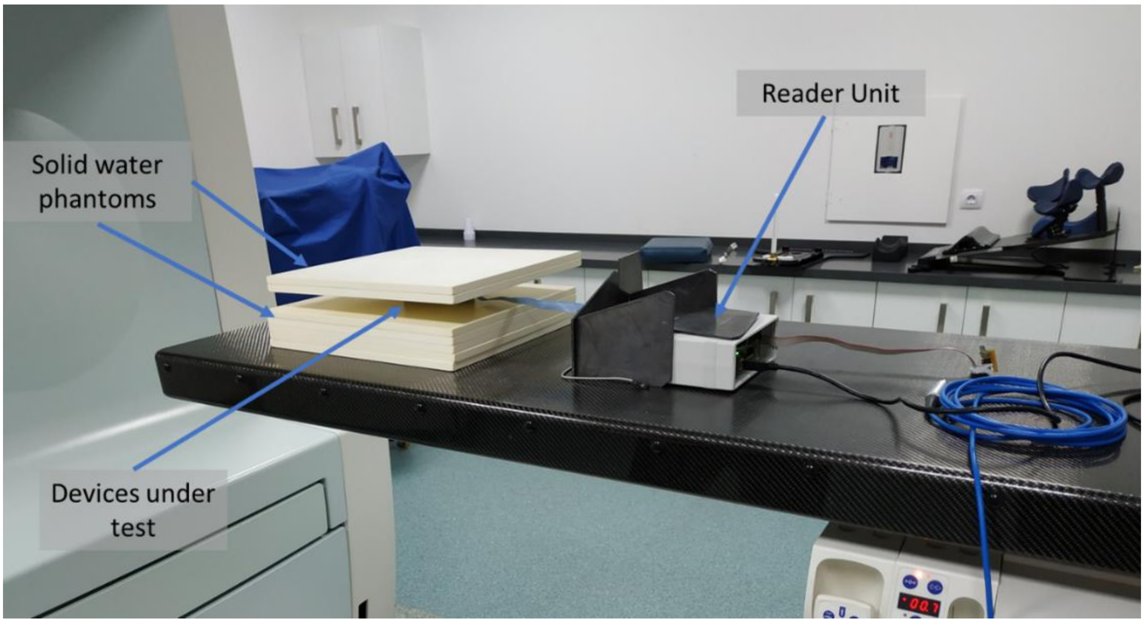

Figure 1. Experimental setup for the dosimetric characterization of the photodiode radiation response. Solid water layers are shown under and over the box containing the devices under test.

With these irradiation conditions, in terms of delivered dose, one monitor unit (MU) of the LINAC corresponds to 0.973 cGy (calibrated at 300 MU/min with a pulse duration of 3 μs and a pulse repetition frequency of 222 Hz). The constancy checks performed on the LINAC ensure that the absorbed dose per monitor unit varies less than 0.5% throughout the tests. Using this configuration and varying pulse repetition frequency, instantaneous dose rates of 50, 100, 150, 200, 250 and 300 MU/min (0.81 cGy/s, 1.62 cGy/s, 2.13 cGy/s, 3.24 cGy/s, 4.05 cGy/s, and 4.87 cGy/s respectively) were applied to characterize the photodiodes response to radiation. The 90-minute irradiation cycle consists of a six-step decreasing instantaneous dose rate staircase from 4.87 to 0.81 cGy/s, a six-step increasing instantaneous dose rate staircase from 0.81 to 4.87 cGy/s, and a last step of 0.81 cGy/s. Between each step, a period without irradiation of 2 minutes was applied. In all cases, each dose rate step duration was calculated to deliver a constant value of 200 MU.

To measure the induced photocurrent, photodiodes were always reverse biased at -10 V. To avoid electromagnetic interference on the photodiode's output current, the readout system was placed into the treatment room but out of the irradiation field. Moreover, the system was shielded by a 3-mm-thick lead layer to protect it from radiation and connected to a computer, placed outside of the treatment room, through an USB cable. More details of the experimental setup and conditions can be consulted elsewhere [26]. For both experimental characterizations, relative uncertainties were obtained as the quadratic propagation of experimental data and one standard deviation of each individual result. Data will be graphically presented as mean with a covering factor k =1 (1 standard deviation).

Results and Discussion

Thermal compensation technique

Our proposal relies on the linear relationship between the forward voltage, V_F, of a p-n junction and temperature [27] as a means to monitor the device temperature. Let us consider the current-voltage curve of a forward biased diode:

$$I = I_S \cdot \exp(qV_F/2kT), \quad (1)$$

where I is the junction current, I_s is the saturation current, q is the absolute value of the charge of an electron, V_F is the diode forward voltage, k is the Boltzmann constant and T is the absolute temperature. It can be shown that the temperature-dependent voltage across the junction can be expressed as:

$$V_F = \frac{E_g}{q} - \frac{2kT}{q}(lnK - lnI), \quad (2)$$

where E_g is the energy band gap for silicon at 0 K, and K is a temperature independent constant. Therefore, when the diode is operated under constant current, the voltage is linearly dependent on temperature, with a typical slope around -2 mV/K.

Once this linear temperature coefficient has been modelled, just with the experimental measurement of V_F, temperature can be measured in the volume device at any time. Therefore, thermal drift of the dark current can be corrected with this calculated temperature. Provided the periodic V_F monitoring, this methodology can be applied to monitor device temperature in real time. Therefore, both forward and reverse biasing must be alternatively applied to the device under irradiation to conduct this procedure as it will be explained below in the readout system description.

Thermal dependence of V_F at constant current was measured by biasing at 1 mA to reduce device self-heating by Joule effect. In Figure 2a, the linear dependence of V_F

with the temperature is clearly obtained for the modelling group. The average linear temperature coefficient, α, was calculated as the average of the thermal coefficient of the three photodiodes studied, resulting α = (-2.32 ± 0.01) mV/K. Therefore, this linear model provides us an accurate determination of the device temperature, just measuring V_F, that is objectively simpler than measuring the temperature itself. Moreover, we get an additional advantage: this is the temperature in the detector volume. This thermal model has been validated with the validation group in Figure 2b. In this Figure 2b, both the average temperature dependence of the three diodes (black symbols) and their correction with the fitting from Figure 2a are shown (grey symbols). On the other hand, Figure 2c depicts, with squared symbols, the temperature dependence of the dark current measured in the same conditions as during irradiation, that is, with a reverse voltage of -10 V. We can see the expectable exponential behaviour according to the theoretical model of this parameter [28]. Figure 2b also shows the excellent exponential fitting (dotted line) of experimental data. Both the theoretical models and the fitting parameters are shown in Table 1. These results will ensure an accurate temperature correction of the dark current and, therefore, of the baseline of the induced photocurrent of this device used as a dosimetric sensor, as it will be shown below. Moreover, we have to remark the fact that under irradiation, the induced photocurrent is in the hundreds of nA, which is negligible with respect to the forward current (1 mA) in the temperature measurement mode and, therefore, it has no effect in the temperature compensation procedure.

Table 1. Modelling of V_F and I_S dependences with the temperature.

	V_F vs. T	**I_S vs. T**
Theoretical model	$V_F = \alpha \cdot T + \beta$	$I_S = A \cdot e^{B \cdot T}$
Fitting parameters	α = (-2.32 ± 0.01) mV/K β = (614 ± 2) mV R^2 = 0.9999	A = (1.7 ± 0.3) A B = (0.096 ± 0.007) K^{-1} R^2 = 0.9977

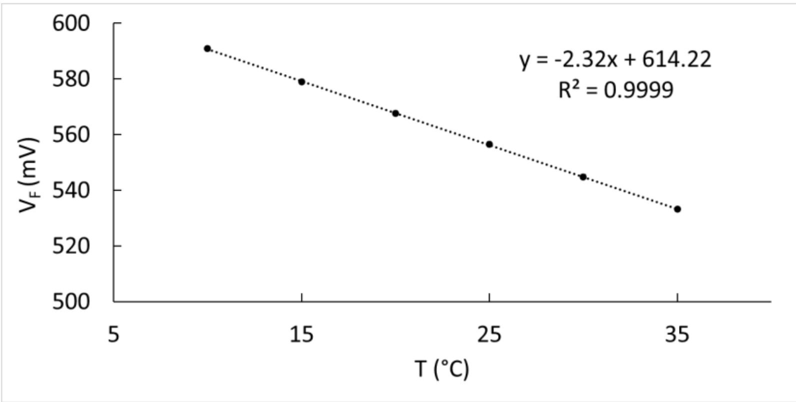

(a)

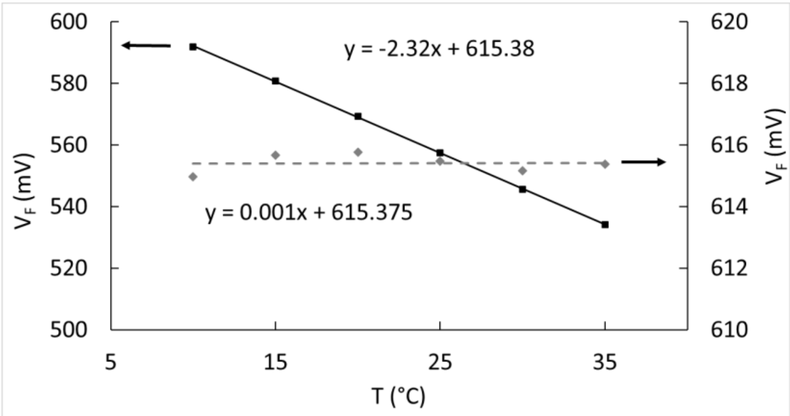

(b)

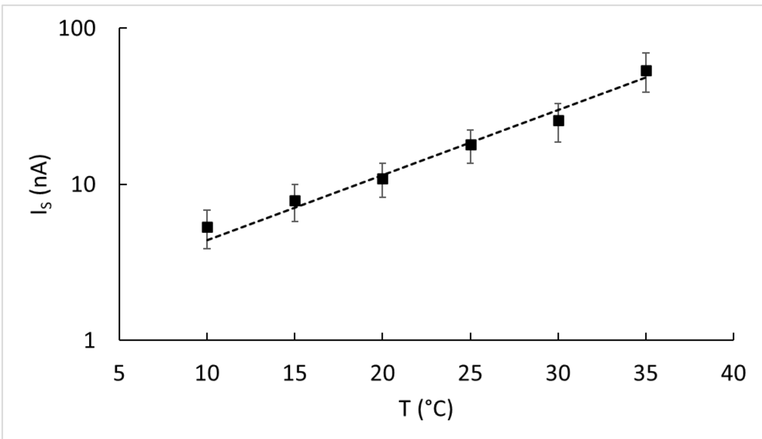

(c)

Figure 2. (a) V_F at constant drain current (I_D = 1 mA) vs. temperature for the modelling group. Experimental data are shown with symbols and linear fitting with the dotted line. Average values of the three sensors are presented. Error bars are smaller than symbols (b) V_F vs.

temperature at 1 mA for the validation group of sensors. Black symbols and line are the experimental data and the linear fitting respectively, and grey ones represent the temperature correction given by the modelling from Figure 2a. Error bars are smaller than symbols (c). Dark current, I_S, showing experimental data (squared symbols) and the exponential fitting (dotted line symbols) at reverse bias of 10 V.

System description and operation

The described two-phase procedure, reverse- and forward-biasing of the PIN photodiode, has been periodically conducted throughout all the dosimetric characterisation previously described. This has provided a continuous and accurate monitoring of the device temperature and a real-time thermal drift compensation method. To do so, we have developed a dosimetric system consisting of a reader unit with the bias module, which is connected to a personal computer for data transfer and unit powering. This device is based on a previous design [20]. Figure 3 shows the complete architecture of the reader unit, pointing out the selectable photodiode biasing. With this same purpose, the analog switch ADG419 (Analog Devices, Massachusetts, USA) has been included in the reader unit. Its purpose is to disconnect the sensors from the reverse bias voltage (V_R) and connect them between ground and current sink, thus allowing the measurement of the forward voltage. With this topology, it is possible to alternatively measure both V_F and the induced photocurrent.

When the topology to measure induced current by radiation is selected by the microcontroller, the photodiode is biased at -10 V and the current generated is related to the dose rate (top signal path in Figure 3a). After that, the reader unit switches to measure V_F. To do this, the analog switch disconnects the photodiode from bias voltage and I/V converter and connects them between ground and sink current. Now, V_F is measured through the buffer and the amplifier, both based on the operational amplifier TL072 (Texas Instruments, Dallas, TX, USA) (bottom signal path in Figure 3a). A configurable sink current designed with LM334 chip (Texas Instruments, Texas, USA) was also added to bias the photodiodes in the forward region (Figure 3b). The current sink, I_D, was selected to minimize the temperature coefficient (LTC) of the LM334 [29]. The circuit shown in Figure 4 balances the positive LTC of the LM334 with the negative LTC of the forward-biased silicon diode. The diode used was 1N4148 (Vishay, Malvern, Pennsylvania, USA), and the resistors R_1 and R_2 were configured to select the desired current, 3.3 kΩ and 33kΩ, respectively. With this configuration I_D was set to 1 mA, to reduce diode self-heating.

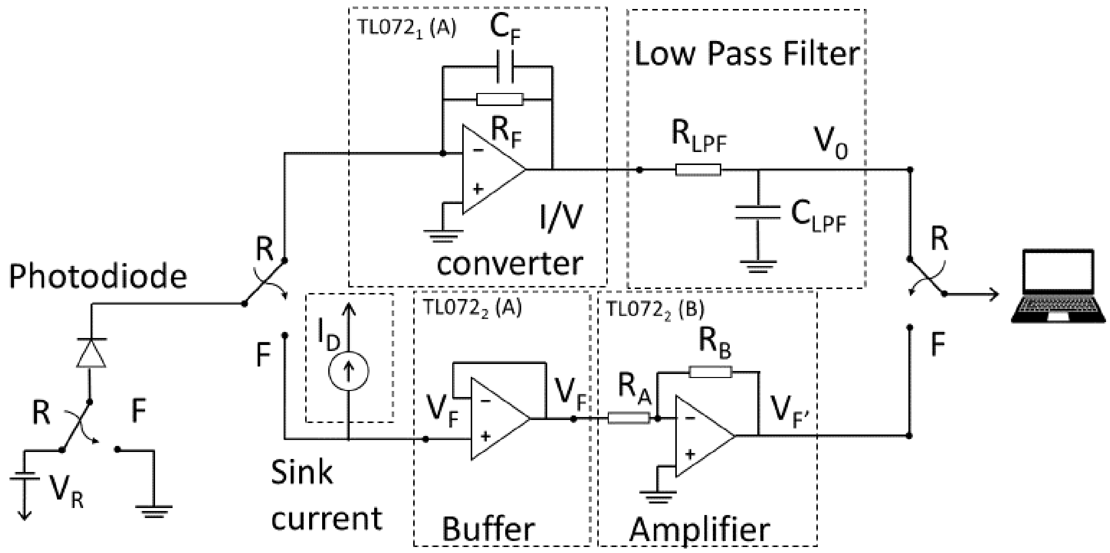

(a)

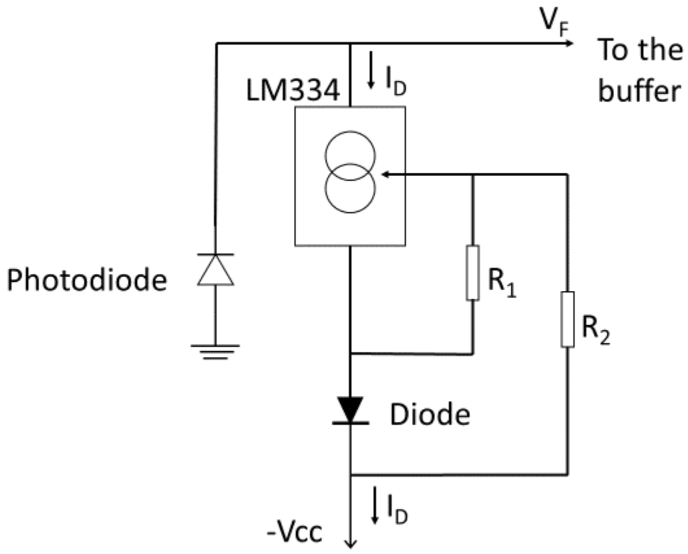

(b)

Figure 3. (a) Schematic of the reader unit showing the signal path for forward bias (F) and for reverse bias and irradiation mode (R). In this circuit, the reverse voltage is V_R = -10 V and forward current I_D = 1 mA. Final connection to computer is also shown. (b) Current sink circuit for forward biasing the photodiode based on LM344 chip with compensation of the temperature effect.

The two operation modes can be observed in the timing chart depicted in Figure 4. Time period of this two-phase procedure was 1 s to ensure signal stabilisation. During phase I, the photodiode is forward-biased to measure V_F and then, to calculate the device temperature. Afterwards, the dosimetric behaviour can be measured with the photodiode reverse-biased in phase II.

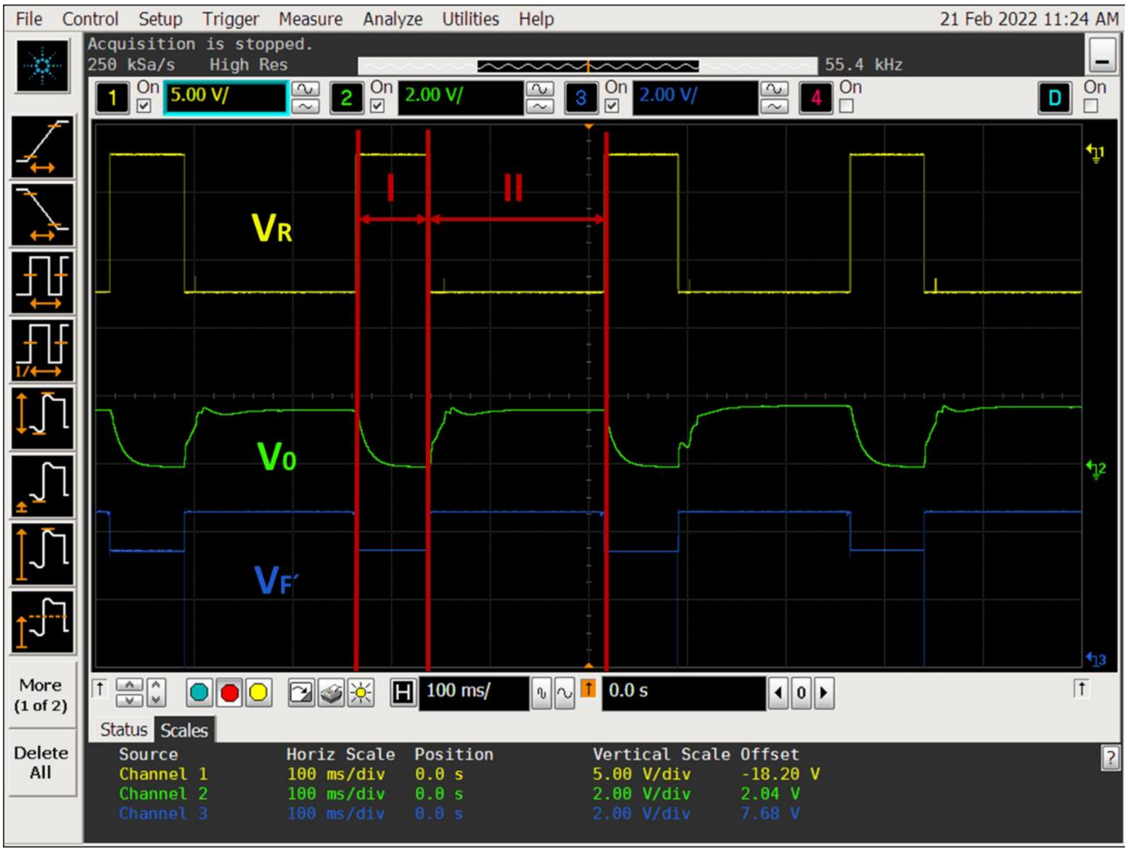

Figure 4. Screenshot from an oscilloscope of the system operation. Yellow and blue lines show reverse and forward voltages respectively, that are applied in phases I and II. Phase I stands for temperature measurement in forward bias and phase II for photocurrent measurement, including compensation of the temperature effect. Green line, V_0, is the output voltage in Figure 3a.

Thermal compensation of the response to the radiation

Using the procedure of temperature determination described in Section 3.1, Figure 5 shows the temperature drift of the sample #4 under the irradiation experiment described above. As mentioned above, acquisition frequency of the device temperature was 1 Hz, demonstrating that it is suitable to monitor this slow changing magnitude in this experimental condition. A heating of 0.35 °C can be measured due to the energy deposition by the photon beam and self-heating. Considering the exponential temperature trend of the dark current, this thermal drift results in a non-negligible baseline drift. Therefore, it should be corrected to obtain an accurate dose rate determination.

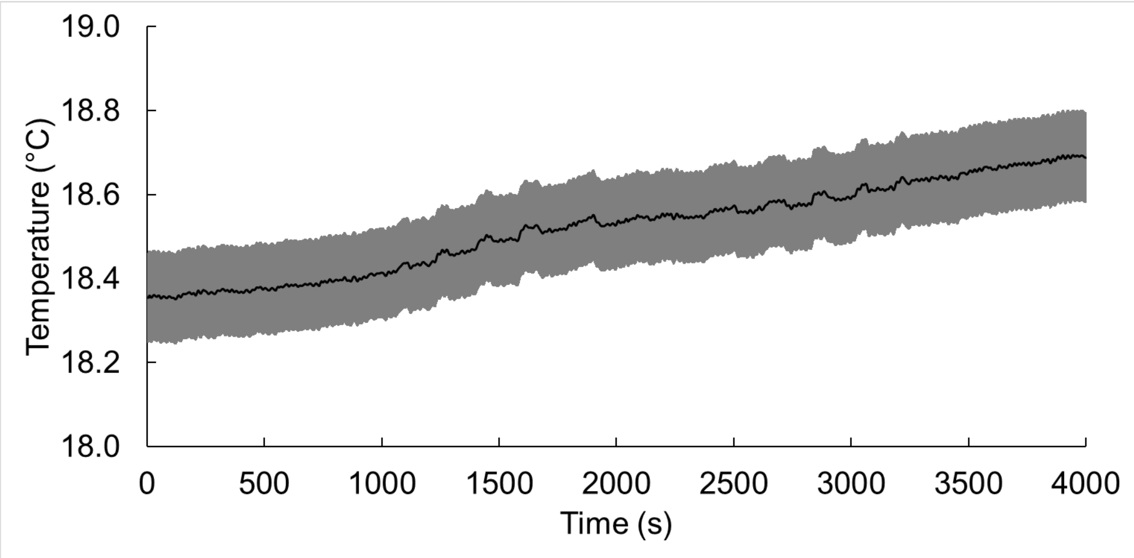

Figure 5. Temperature drift of the sample #4 during the irradiation experiment with the proposed procedure. Shaded interval represents experimental data uncertainties (coverage factor k=1).

Figure 6 displays the photodiode current of the complete irradiation cycle of the sample #4. Figure 6 inset zooms the baseline data, that is, the dark current. Blue dots depict the uncompensated baseline with a total drift of 0.20 nA. This value represents a relative error of 1.5% in the worst case (for the lower dose rate, 0.81 cGy/s). Once our compensation method is applied, red dots are obtained, resulting in a maximum relative error of 0.2%, thus achieving a significant reduction of the baseline linear thermal drift by a factor of 7.5. As a consequence, these figures prove the effectiveness of the proposed procedure by taking advantage of a p-n junction as an accurate and linear temperature sensor. With this temperature correction, the photodiode sensitivity, S, was obtained as the slope of the linear fit of the induced current (nA) as a function of dose rate (cGy/s) for each device. Figure 7 shows the radiation sensitivity of each irradiated photodiode. The average sensitivity can be calculated, obtaining S = 12 ± 2 nC/cGy (coverage factor k = 1). This result is similar to the previously obtained value of 13.8 ± 0.4 nC/cGy [26]. The slightly lower measured sensitivity can be explained because the photodiode is forward biased for a fraction of time to implement the temperature compensation procedure, instead of being always reversed while the irradiation. Therefore, when the device is not reverse biased, its sensitivity decreases because of a lower capability of electron-hole separation before recombination, generating lower photocurrent.

As shown in Figure 6, to determine the repeatability and stability of the sensor response, high to low and low to high dose rate irradiation cycles were applied and sensitivity degradation was found below 2% in the dose range up to 21.4 Gy. The degradation was calculated as the relative decrease of both slopes in percentage in the whole irradiation cycle (see Figure 8). Table 2 shows the fitting parameters of curves from Figure 8, obtaining the mentioned slight decrease of the sensitivity in the second part of the irradiation cycle (from low to high dose rate).

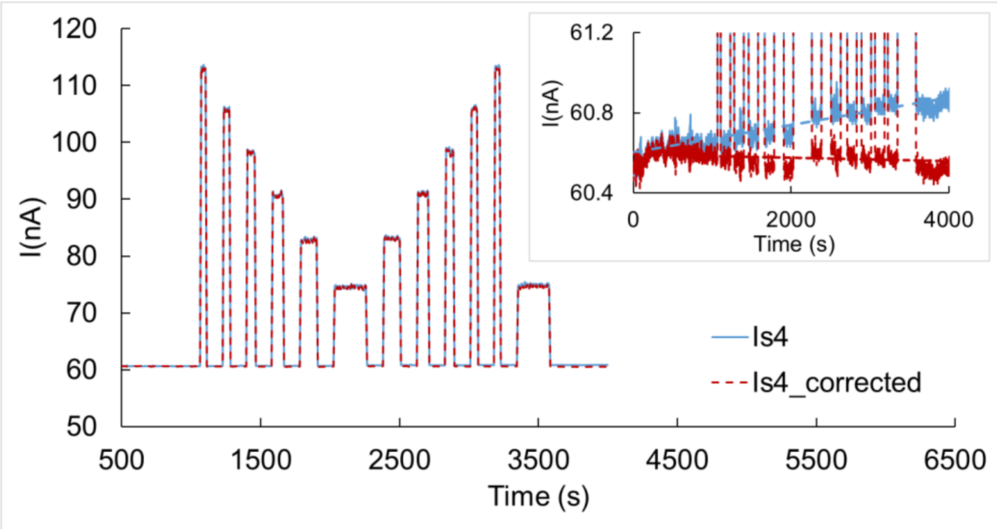

Figure 6. Experimental photocurrent during the dosimetric characterization of the sample #4 showing the proposed complete irradiation cycle. Inset shows the zoomed dark current before (I_{s4}, blue dots) and after ($I_{s4\_corrected}$, red dots) thermal compensation.

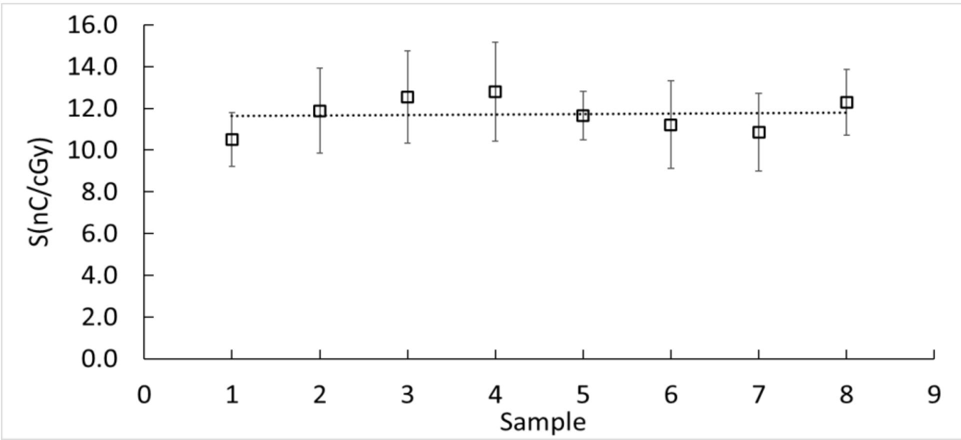

Figure 7. Photodiode sensitivity to instantaneous dose rate. Experimental data uncertainties correspond to a coverage factor k=1. Line shows the average sensitivity.

Table 2. Modelling of sensitivity with dose rate.

	High to low dose rate $\boldsymbol{A \cdot x + B}$	**Low to high dose rate** $\boldsymbol{C \cdot x + D}$
Fitting parameters	A = (9.47 ± 0.11) nC/cGy B = (6.7 ± 0.3) nA	C = (9.7 ± 0.3) nC/cGy D = (6.6 ± 0.5) nA

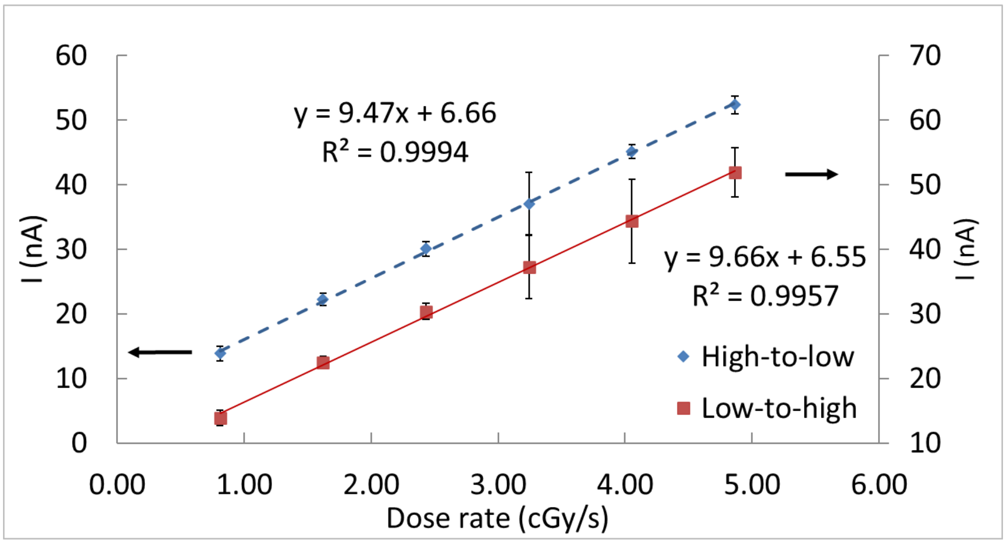

Figure 8. Photocurrents versus high to low (diamond symbols) and low to high (square symbols). Lines show the linear tendencies. Experimental data uncertainties are shown with bars (coverage factor k = 1).

Conclusions

A method for thermal compensation of radiation-induced current in photodiodes has been presented and experimentally tested. It is based on the linear dependence between temperature and forward voltage (V_F) of a p-n junction. In fact, measuring this forward voltage, we can monitor the device temperature and correct the highly thermal sensitive dark current. It has the advantage that no external sensors are needed to obtain the temperature. To do that, only a few modifications have been introduced in the reader unit previously developed by our research group.

To check the algorithm, the BPW34S Si PIN photodiode was used as a current-mode radiation sensor. Applying the compensation algorithm implemented in the reader, the thermal drift of the photodiode dark current was reduced from 1.5% to 0.2% for the lower dose rate. Moreover, with an accumulated dose of 21.4 Gy of photon beams of 6 MV, a sensitivity degradation below 2% and an average sensitivity of 12 ± 2 nC/cGy were obtained, which is in agreement with previous results. Therefore, the procedure presented in this work is suitable to model and reduce the thermal dependence in measured radiation-induced current of photodiodes.

Acknowledgments.

This research has been partially funded by Junta de Andalucía (Spain), projects numbers PI-0505-2017 FEDER/Junta de Andalucía-Consejería de Economía y Conocimiento Project B-TIC-468-UGR18, Proyecto del Plan Nacional I+D: PID2019-104888GB-I00 and Proyectos I+D+i Junta de Andalucía 2018: P18-RT-3237. This work was also conducted in the framework of H2020 ELICSIR project (grant No. 857558). P. Escobedo thanks grant IJC2020-043307-I funded by MCIN/AEI/ 10.13039/501100011033 and by "European Union NextGenerationEU/PRTR".

References

[1] L.A.P. Santos, E. F. da Silva Jr, E. Vilela, Filtered X Ray Beam Dosimetry from 10-3 to 102 Gy Dose Range by using Phototransistors, Radiat. Prot. Dosimetry. 101 (2002) 145–148. https://doi.org/10.1093/oxfordjournals.rpd.a005956.

[2] C. Romei, A.D. Fulvio, C.A. Traino, R. Ciolini, F. d'Errico, Characterization of a low-cost PIN photodiode for dosimetry in diagnostic radiology, Phys. Med. 31 (2015) 112–116. https://doi.org/10.1016/j.ejmp.2014.11.001.

[3] Andjelković MS, Ristić GS. Feasibility study of a current mode gamma radiation dosimeter based on a commercial PIN photodiode and a custom made auto-ranging electrometer. *Nucl Technol Radiat Prot*. 2013; **28**: 73– 83. https://doi.org/10.2298/NTRP1301073A

[4] G.F. Knoll, Radiation detection and measurement, 3rd Ed., John Wiley & Sons, Inc, 2000.

[5] J. Barthe, Electronic dosimeters based on solid state detectors, Nucl. Instrum. Methods Phys. Res. Sect. B Beam Interact. Mater. At. 184 (2001) 158–189. https://doi.org/10.1016/S0168-583X(01)00711-X.

[6] A.B. Rosenfeld, Electronic dosimetry in radiation therapy, Radiat. Meas. 41 (2006) 134–153. https://doi.org/10.1016/j.radmeas.2007.01.005.

[7] I.S. Deev, The Use of Cadmium Sulphide Photo-Conductors in Radiation Dosimetry, J. Nucl. EnergyPart BReactor Technol. 1 (1960) 204–210. https://doi.org/10.1016/s0368-3273(15)30029-8.

[8] F.A.S. Soliman, H.A. Ashry, Radiation effects on non-linear resistances, J. Mater. Sci. Mater. Electron. 4 (1993) 293–300. https://doi.org/10.1007/BF00179227.

[9] J. Román-Raya, I. Ruiz-García, P. Escobedo, A.J. Palma, D. Guirado, M.A. Carvajal, Light-dependent resistors as dosimetric sensors in radiotherapy, Sens. Switz. 20 (2020). https://doi.org/10.3390/s20061568.

[10] M. Soubra, J. Cygler, G. Mackay, Evaluation of a dual bias dual metal oxide-silicon semiconductor field effect transistor detector as radiation dosimeter, Med. Phys. 21 (1994) 567–572. https://doi.org/10.1118/1.597314.

[11] A. Holmes-Siedle, L. Adams, RADFET: A review of the use of metal-oxide-silicon devices as integrating dosimeters, Int. J. Rad. Appl. Instr. C. Radiat. Phys. Chem. 28 (1986) 235–244. https://doi.org/10.1016/1359-0197(86)90134-7.

[12] R.C. Hughes, D. Huffman, J.V. Snelling, T.E. Zipperian, A.J. Ricco, C.A. Kelsey, Miniature radiation dosimeter for in vivo radiation measurements, Int. J. Radiat. Oncol. 14 (1988) 963–967. https://doi.org/10.1016/0360-3016(88)90019-3.

[13] R.A. Price, C. Benson, M.J. Joyce, K. Rodgers, Development of a RadFET linear array for intracavitary in vivo dosimetry during external beam radiotherapy and brachytherapy, - IEEE Trans. Nucl. Sci. 51 (2004) 1420–1426. https://doi.org/10.1109/TNS.2004.832570.

[14] D. Georg, B.D. Ost, M.-T. Hoornaert, P. Pilette, J.V. Dam, M.V. Dycke, D. Huyskens, Build-up modification of commercial diodes for entrance dose measurements in 'higher energy' photon beams, Radiother. Oncol. 51 (1999) 249–256. https://doi.org/10.1016/S0167-8140(99)00058-4.

[15] V. Panettieri, M.A. Duch, N. Jornet, M. Ginjaume, P. Carrasco, A. Badal, X. Ortega, M. Ribas, Monte Carlo simulation of MOSFET detectors for high-energy photon beams using the PENELOPE code, Phys. Med. Biol. 52 (2006) 303–316. https://doi.org/10.1088/0031-9155/52/1/020.

[16] M.A. Carvajal, S. García-Pareja, D. Guirado, M. Vilches, M. Anguiano, A.J. Palma, A.M. Lallena, Monte Carlo simulation using the PENELOPE code with an ant colony algorithm to study MOSFET detectors, Phys. Med. Biol. 54 (2009) 6263–6276. https://doi.org/10.1088/0031-9155/54/20/015.

[17] M. Osullivan, A. Kelleher, J. Ryan, B. Oneill, B. Lane, Temperature compensation of PMOS dosimeters, in: AA(University Coll., Cork (Ireland).), AB(University Coll., Cork (Ireland).), AC(University Coll., Cork (Ireland).), AD(University Coll., Cork (Ireland).), AE(University Coll., Cork (Ireland).), 1991: pp. 281–285. https://ui.adsabs.harvard.edu/abs/1991ESASP.313..281O.

[18] I. Thomson, Direct reading dosimeter, EP0471957A2, 1991.

[19] M.A. Carvajal, A. Martínez-Olmos, D.P. Morales, J.A. Lopez-Villanueva, A.M. Lallena, A.J. Palma, Thermal drift reduction with multiple bias current for MOSFET dosimeters, Phys. Med. Amp Biol. 56 (2011) 3535–3550. https://doi.org/10.1088/0031-9155/56/12/006.

[20] M.A. Carvajal, M.S. Martínez-García, D. Guirado, J. Banqueri, A.J. Palma, Dose verification system based on MOS transistor for real-time measurement, Sens. Actuators Phys. 247 (2016) 269–276. https://doi.org/10.1016/j.sna.2016.06.009.

[21] A. Szmyrka-Grzebyk, L. Lipiński, Low temperature current - voltage characteristics of silicon diodes used as thermometers, Cryogenics. 33 (1993) 222–225. https://doi.org/10.1016/0011-2275(93)90141-A.

[22] R.O. Ocaya, A linear, wide-range absolute temperature thermometer using a novel p–n diode sensing technique, Measurement. 46 (2013) 1464–1469. https://doi.org/10.1016/j.measurement.2012.12.008.

[23] R.O. Ocaya, An experiment to profile the voltage, current and temperature behaviour of a P–N diode, Eur. J. Phys. 27 (2006) 625–633. https://doi.org/10.1088/0143-0807/27/3/015.

[24] G.C.M. Meijer, Thermal sensors based on transistors, Sens. Actuators. 10 (1986) 103–125. https://doi.org/10.1016/0250-6874(86)80037-3.

[25] M.A. Carvajal, F. Simancas, D. Guirado, M. Vilches, A.M. Lallena, A.J. Palma, A compact and low cost dosimetry system based on MOSFET for in vivo radiotherapy, Sens. Actuators Phys. 182 (2012) 146–152. https://doi.org/10.1016/j.sna.2012.05.024.

[26] I. Ruiz-García, J. Román-Raya, J. Banqueri, A.J. Palma, D. Guirado, M.A.Carvajal, Commercial photodiodes and phototransistors as dosimeters of photon beams for radiotherapy, Med. Phys. 48 (2021) 5440–5447. https://doi.org/10.1002/mp.14921.

[27] J. Fraden, Handbook of Modern Sensors, 2nd Edition, Springer, New York, 1996.

[28] S.M. Sze, Physics of Semiconductor devices, John Wiley&Sons, New York, 1969.

[29] T. Instruments, LM134/LM234/LM334 3-Terminal Adjustable Current Sources, (2013). https://www.ti.com/lit/ds/symlink/lm134.pdf?ts=1637595584814.

3.2 Sport monitoring

In this section we will report the results obtained in the research line of sports monitoring. The platform developed for these investigations as well as the results obtained with its use will be presented.

3.2.1 Inertial measurement system

The customized electronic board (Figure 35) integrates an MPU-9250 (Invensense, San Jose, CA, USA) 9-degree-of-freedom IMU, which encompasses a 3-dimensional accelerometer, gyroscope, and magnetometer. The inertial motion sensor comprises a TDK-INVN 6-axis IMU MPU-6500 with a configurable acceleration range from ±2 g to ±16 g and a configurable gyroscope range from ±250 to ±2000 degrees per second (dps). It also features an AKM-8963 magnetometer (AKM Semiconductor, Inc., Tokyo, Japan) with a range of 4800 μT connected through the AUX-I2C port of the MPU-6500. This inertial measurement unit includes digital motion processor (DMP) technology, capable of filter processing and accurate calculation of three-dimensional orientation, or the so-called Attitude Heading Reference System (AHRS), to determine the inertial angles of yaw, roll, and pitch. For three-dimensional orientation, a fusion of sensor data is performed in the DMP to obtain rotation quaternions. Rotation quaternions serve as a mechanism for representing rotations in three dimensions, and with a few simple calculations, Euler angles can be derived. This operation is performed by the microcontroller, which is connected to the inertial sensor using I2C communication. Subsequently, yaw, pitch, roll, and three-dimensional accelerations are transmitted to the user's smartphone via Bluetooth and saved in an onboard SD as a backup. Both the SD card and the BM78 Bluetooth module (Microchip Technologies Inc., Chandler, AZ, USA) are integral components of the custom-developed electronic board. To power the system, a 450 mAh battery is employed, providing autonomy for over ten hours in normal operating mode. It is worth mentioning that a sample rate of 112 Hz was selected, and the accelerometer and gyroscope were configured at their maximum ranges (±16 g and ±2000 dps, respectively). In addition, the IMU incorporates an internal temperature sensor utilized for monitoring the temperature of the system.

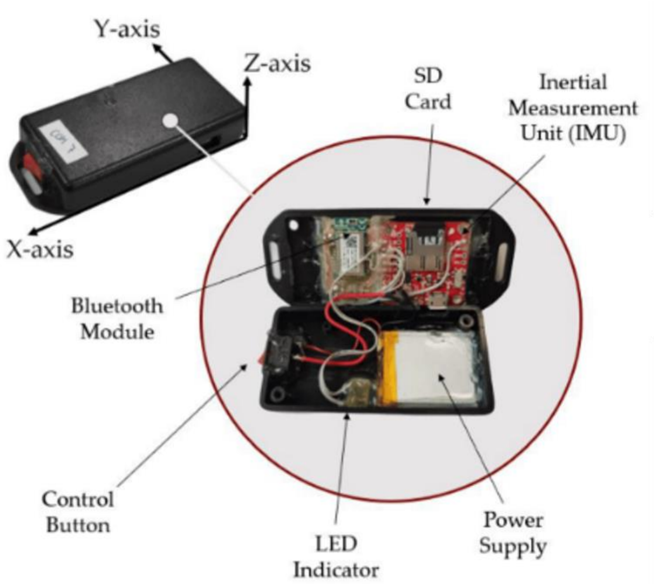

***Figure 35**. Inertial sensing platform developed.*

As a microcontroller the SAMD21G18 was selected. Part of the ARM family boasts a sophisticated set of features tailored for a diverse range of embedded applications. Its ARM Cortex-M0+ architecture, renowned for its efficiency and performance, serves as the backbone for a multitude of tasks requiring reliable and high-speed processing capabilities.

At the heart of the SAMD21G18 lies its powerful processing core, capable of executing complex instructions swiftly and accurately. This ensures seamless operation even in demanding environments, making it an ideal choice for applications requiring real-time responsiveness and computational efficiency. Furthermore, the SAMD21G18 offers a generous array of integrated peripherals, including multiple serial communication interfaces such as UART, SPI, and I2C, facilitating seamless connectivity with a wide range of external devices and components. Additionally, its advanced analog-to-digital converter (ADC) enables precise analog signal acquisition, ensuring accurate data capture in various sensing applications.

In terms of memory, the SAMD21G18 provides ample resources for code storage and data manipulation. With its sizable Flash memory capacity, developers have ample room to store application code and firmware updates, while its SRAM and EEPROM modules offer flexible options for temporary data storage and non-volatile parameter storage. Moreover, the SAMD21G18 is designed with energy efficiency in mind, featuring multiple power-saving modes and low-power operation capabilities. This makes it well-suited for battery-powered and energy-conscious applications, extending battery life and reducing overall power consumption.

The SAMD21G18 microcontroller is supported by a robust ecosystem of development tools and software libraries, facilitating rapid prototyping and streamlined application development. Its compatibility with industry-standard development environments and programming languages simplifies the development process, enabling developers to leverage existing resources and expertise effectively. In summary, the microcontroller embodies the hallmark features of ARM-based microcontrollers, offering a potent combination of performance, versatility, and energy efficiency. Its comprehensive feature set and robust design make it an excellent choice for a wide range of embedded applications, from IoT devices to industrial automation systems.

Finally, it should be noted that this sensor platform has been used in the third publication of the compendium, the study of jumps detailed below, and in a work in which artificial intelligence has been used to differentiate between different skiing techniques, a work that has been submitted for publication.

3.2.2 Flight time determination in vertical jumps

Monitoring jumping capacity stands out as a crucial aspect in some sports, enabling performance measurement, tracking progression, and injury prevention. Here, we introduce a system capable of measuring user flight time and reached height. The inertial system previously developed [96] was used for this study.

The force platform records a resting acceleration value of 1 g, showing no force during the flight phase, and a sharp peak during landing. Flight time and jump height are calculated using specialized software. Regarding the inertial system, it displays -1 g during rest, a drop before the jump, a spike at take-off, and stability during flight (see Figure 36). An algorithm identifies jump key points based on this data.

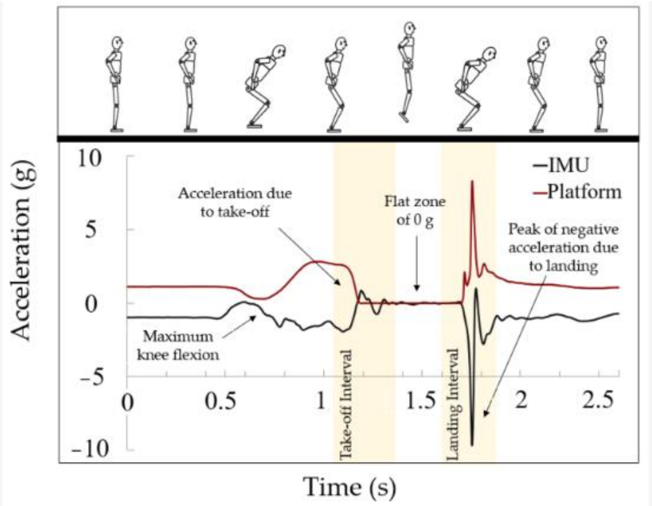

Figure 36. Experimental results of the jumping tests are depicted below. The data reported by the inertial system is represented by the black line, while data provided by the force platform is shown in red [49].

The algorithm for analyzing jump data (Figure 37) begins by identifying two crucial points: P1, marking the descent after the jump, and P2, indicating the jump's peak. These serve as reference points for defining intervals. Additionally, point P3 helps determine these intervals. Subsequently, the algorithm estimates the airborne interval by calculating the mean and standard deviation between points P4 and P5. Within these intervals, take-off (P6) and landing (P7) are identified based on acceleration thresholds, aided by linear interpolation for precise timing. The flight time (TOF) is then calculated as the difference between take-off and landing times. Lastly, using TOF, the algorithm estimates jump height (h) via a physical model, providing athletes with valuable insights to enhance their techniques.

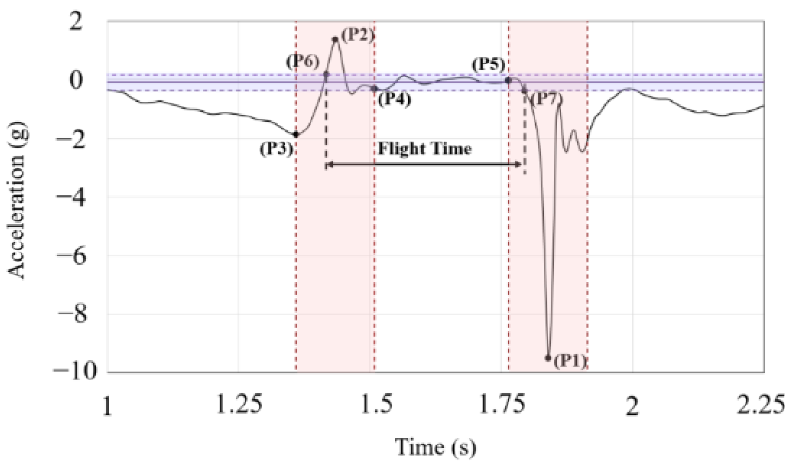

Figure 37. *Time-of-flight calculation algorithm from the IMU measurements [49].*

The collected data underwent processing, followed by a statistical analysis to evaluate the agreement between the force platform and the developed system. Measurement errors were determined as the discrepancies in flight time (TOF) values between the inertial system and the platform. The level of agreement was assessed through linear regression analysis, indicating excellent agreement with a regression equation of 0.99x + 0.00 and an R^2 factor of 0.96. Furthermore, deviation analysis concerning the average of both systems revealed that most cases fell within ±2 standard deviations (SD) range, with minimal deviations observed (up to 12 ms). Similarly, for jump height measurements, linear regression yielded 0.97x + 0.01 with an R^2 factor of 0.96. Deviation analysis showed values within ±2 SD, except for one case (0.011 m deviation). Maximum difference between the averages of three attempts and individual attempts was 0.028 m.

In conclusion, the system provides reliable and accurate measurements of flight time and jump height, making it highly appropriate for use in training sessions due to its compact size and portability. With minimal errors observed—just 0.35% for flight time and -1.84% for height measurement—after comprehensive testing, this system proves suitable for outdoor training sessions, facilitating real-time performance monitoring for both elite athletes and amateurs.

3.2.3 Publication 3

Development and Validation of a Low-drift Inertial Sensor-Based System for analysis of alpine skiing performance.

Isidoro Ruiz-García[1]**,** Ismael Navarro-Marchal [2,3], Javier Ocaña-Wilhelmi [2], Alberto J. Palma [1], Pablo J. Gómez-López [2] and Miguel A. Carvajal [1 *]

[1] ECSens, iMUDS, Department of Electronics and Computer Technology, ETSIIT, University of Granada, Granada (Spain); isirg@ugr.es; ajpalma@ugr.es; carvajal@ugr.es

[2] SkinngLab, iMUDS, Sport and Health University Research Institute (iMUDS, Department of Physical and sport education, University of Granada, Granada, (Spain); inv.ismaelnm96@ugr.es; jocana@ugr.es; pjgomez@ugr.es

[3] Human Lab, iMUDS - Sport and Health University Research Institute (iMUDS), Dpto. Physical Education and Sport, Faculty of Sport Sciences, University of Granada, (Spain); inv.ismaelnm96@ugr.es

* Correspondence: carvajal@ugr.es; Tel.: +34958242302 (M.A.C.)

- Sensors 2021, 21, 2480. https://doi.org/10.3390/s21072480
- Journal Impact Factor (2021): 3.847
- Rank by Journal Citation Indicator (JCI): Q2 in category INSTRUMENTS & INSTRUMENTATION (19/63)

Abstract: In skiing it is important to know how the skier accelerates and inclines the skis during the turn to avoid injuries and improve technique. The purpose of this work was to develop and validate a compact, wireless and low-cost system for detecting the inclination and acceleration of skis in the field based on inertial measurement units (IMU). To that end, a commercial IMU board has been placed on each ski behind the skier boot. With the use of an Attitude and Heading Reference System algorithm included in the sensor board, the orientation and attitude data of the skis was obtained (roll, pitch and yaw). This information has been compared with the data collected by a video-based 3D-kinematic reference system to validate its operation, obtaining the Pearson coefficient between 0.9959 and 0.922 when used in a ski simulator. Moreover, the results demonstrate that the proposed IMU-based system can provide reliable low-drifted data for more than 15 minutes of continuous usage in the worst case.

Keywords: Inertial sensor; accelerometer; kinematics, alpine skiing, kinetics, photogrammetry 3D

---

1. Introduction

Amateur and elite skiers of alpine skiing would be able to improve their technique with a reliable tool of quantitative performance evaluation. Moreover, this tool could provide injury prevention and coaching efficiency. Turns are basic units of alpine skiing performance, and the segmentation of skiing runs into turns would allow further knowledge of the skiing technique within and between them. Information about accelerations, angles and times are fundamental to assess each turn and the skiers' overall performance [1]. In this way, Spörri et al. showed the characteristics of a Top World Class Athlete in Giant Slalom [2].

Different systems have been proposed for monitoring the skiing performance. It was proposed a methodology based on video analysis with an objective criterium to turn detection, which was suggested to be independent of the skiing technique [3]. Moreover, a 3-dimensional video-based method was implemented to examine kinematic, kinetic, and energetic issues related to skier technique during slalom race simulations [1]. On the other hand, a high-precision kinematic global navigation satellite system (GNSS) was evaluated to detect cross-country skiing classical style technique [4]. Furthermore, Stöggl et al. reported the analysis of the type, number, and cycle duration of this skiing style, based on the motion of the head and net vertical displacement were derived from GNSS position data [5].

Wireless portable inertial sensors, the so-called inertial measurement units (IMUs), are currently employed for monitoring sport activity, not only in research works but also in commercial entertainment systems [5]. In addition, this technology can be used for injury prevention and skiing performance enhancement [6]. Camomilla et al., describe the different uses of inertial sensors in sport, which are: motor capacity assessment, technique analysis, activity classification, and physical demands assessment. The inertial sensors have been used in alpine skiing to study, forward displacement, speed and acceleration of the Centre of Mass (CoM), orientation (inclination) of rigid objects such as skis, speed and acceleration of rigid objects (skis), orientation of body segments, especially the lower limbs, kinematic parameters of lower limb angulation, dynamic calculations of external force such as dissipative forces, ground reaction force and power [7]. Martinez et al,. study's focuses on the development and validation of a methodology for the accurate detection of turns in the field as well as identifying different types of runs [8], as well as Neuwirth et al,. classified the different types of skiing styles, parallel (drifted or carved) and non-parallel (snowplow or snowplow-steering) turns, based on a global navigation satellite system (GNSS) and inertial sensors (IMU), 3D speed and acceleration data were obtained [9]. Snyder et al, validate a wearable system for edge angle estimation during simulated alpine skiing on a ski ergometer. The wearable system consisted of two IMU mounted to the upper posterior cuff of each ski boot using a custom housing and strap. [10]

This technology alone or combined with others previously mentioned has also been applied to alpine skiing, simplifying the data gathering and improving the skier comfort during tests [11][12][13]. Data from these systems along with the snow conditions, skier´s speed and slope´s inclination can provide valuable information for improve skiing technique and minimize injuries. In this line, Martínez et al. developed an automatic algorithm to detect skier's turns in an ergometer, with an IMU attached to the posterior upper cuff of each ski boot [12]. Yu et al. discussed different location for an IMU on the skier's body, and they identified the pelvis as the best location to attach the sensor [13].

All of these works provided remarkable insights into the monitoring of skiing performance. However, they still present some limitations to be used in actual ski trainings due to, for example, very limited capture volume, small number of turns, heavy data post-processing, complex sensor setup [13] or testing in far from real conditions [12].

The purpose of this work was to design and validate a reliable, simple, comfortable, and low-cost wireless system based on IMU, capable of providing useful data in real time that could be used in real conditions. The proposed system supplies all data required by skiers and coaches to improve skiing technique reducing the risk of injury: 3 dimensional accelerations, inertial angles (yaw, pitch and roll) and times. Figure 1 shows a comprehensive scheme of the full experimental setup for the IMU system validation based on an 3D photogrammetric system with infrared (IR) cameras as gold standard. Our proposed wireless system consisted of instrumented skis including each an IMU, pre-processing electronics, support for better video recording, and rechargeable power supply. Alpine skiing runs were carried out in a ski simulator. Aiming to overcome some previous limitations, reduced data drift was addressed to achieve long-lasting tests comparable to skiing runs in real conditions.

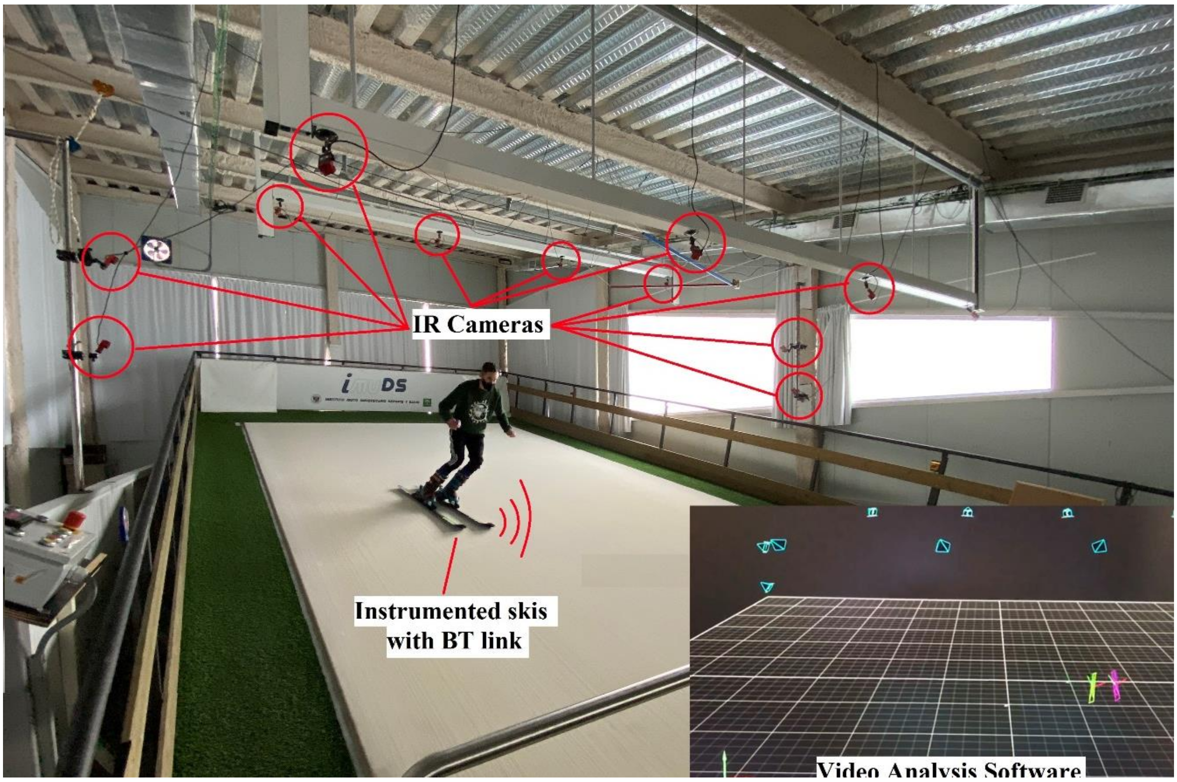

Figure 1. A skier during an experimental test in the ski simulator placed at the Sport and Health University Research Institute (iMUDS), University of Granada, Granada, Spain.

2. Materials and Methods

Tests were carried out in a MaxxTracks ISB2000 ski simulator (© MaxxTracks Indoor Skislopes, Beverwijk, The Netherland) designed for training, research and teaching purposes, whose dimensions are: 12.50x6.55 m (48 m^2) (see Figure 1). Its surface speed can be varied between 1-21 km/h and the slope ranges from 10º to 19º. Surface wetting is required for achieving a suitable skier's sliding. This ski simulator is placed at the Sport and Health University Research Institute (iMUDS), University of Granada, Granada, Spain.

For validation purposes, a 3D photogrammetric system (© 2020 NaturalPoint, Inc. DBA OptiTrack, Beaverton, OR, USA) was used as gold standard. It is composed of a ring of 12 infrared (IR) cameras Flex 3 (Resolution: 640x480, Frame rate: 100 FPS), oriented to the ski slope. The camera 3D system requires infrared markers attached to the skis to detect their positions. Usually employed passive markets cannot be used on the skis because their reflective surface would be shielded by the wet surface splashing, preventing a good sight of the ski's position. To overcome this limitation, as it will be explained below, active IR markers with light-emitting diodes (LED) were included in the skis. Data from cameras were processed by Motive, an optical motion capture software (© 2020 NaturalPoint, Inc. DBA OptiTrack, Beaverton, OR, USA). This software analyses the camera recordings and stores times, positions and inertial angles (pitch, yaw and roll) of each ski. Signals obtained by the camera system are interpolated and smoothed by a cubic spline, resulting in less than 0.2 mm of position's uncertainty.

2.1. Wireless portable system design

The 9DoF Razor IMU board (SparkFun Electronics, Niwot, CO, USA) was selected which is intended to obtain information attitudes and three-dimension orientation or so-called Attitude Heading Reference System (AHRS). This low-cost electronic board combines an MPU-9250 (Invensense, San Jose, CA, USA) 9 degree-of-freedom (3 dimensional accelerometer, gyroscope and magnetometer) IMU, and an onboard SAMD21 low-power microcontroller (Microchip Technologies Ic., Chandler, AZ, USA) with Digital Motion Processor (DMP) technology that can perform filter process and an accurate calculation AHRS to determine the ski orientation. IMU sensors were configured with the following ranges: the triple-axis MEMS gyroscope was set full-scale range at ±2000º/sec (±3%); the triple-axis MEMS accelerometer at ±2g (±3%) and corner frequency of the digitally-programmable low-pass filter at 5 Hz; and the triple-axis MEMS magnetometer at ±4800 μT. Moreover, this board is supplied with a micro SD memory card slot, allowing IMU data logging. The firmware provided by the IMU manufacturer was reprogrammed to synchronize the IMU and the camera system, setting 100 Hz as sampling rate. Skier orientation, inertial angle, and coordinate axes: x, y, and z, are shown in Figure 2.

Just after powering up, an initial accelerometer and gyroscope calibration procedure is undertaken consisting in IMU standing on a levelled flat surface for 10 seconds.

Gyroscope is adjusted to 0 º/s in all axes and the accelerometer to 1 g in the z axis and zeroing the rest of axis. No user assistance is required to start it.

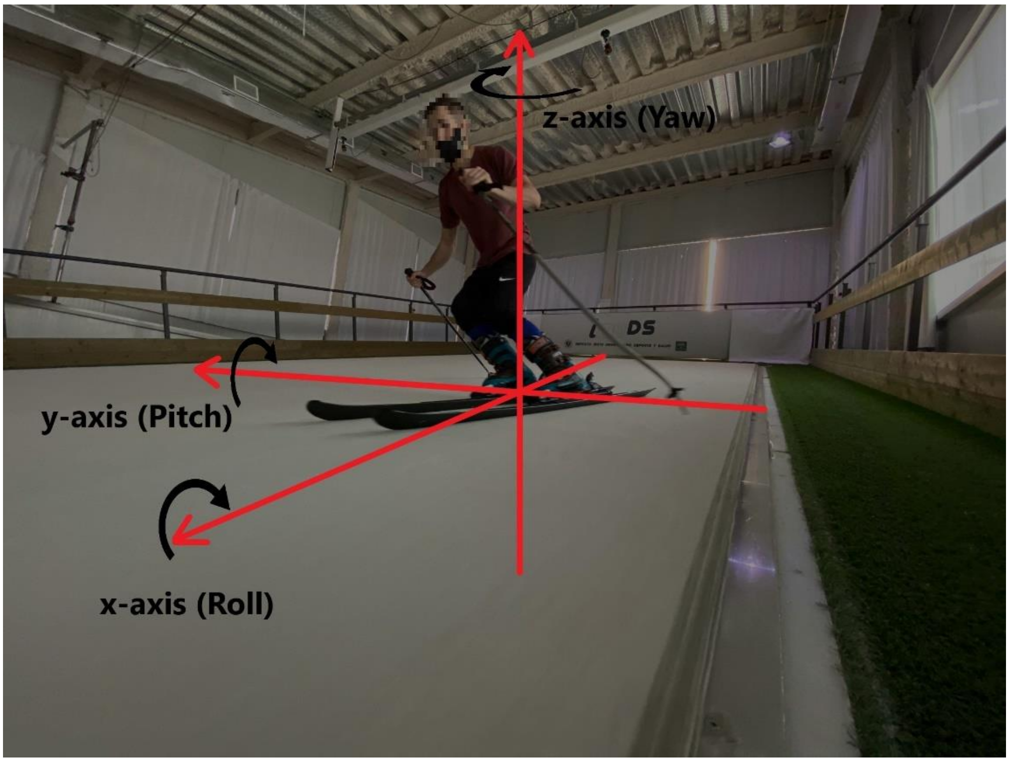

Figure 2. Rotational axes of the ski turn

As mentioned above, to allow correct skis positioning by 3D camara system, five 830 nm IR LEDs VSMG2700 (Vishay Intertechnology, Malvern, PA, USA) were soldered on a PCB (Printed Circuit Board) and placed on in the front and rear part of each ski. Four LEDs (positioning LEDs) were used to monitor the ski movement and the fifth one (sync LED) was used to set the starting of the test as detailed below. The spectrum of the IR LEDs was measured in order to ensure that the maximum frequency emission was tuned with maximum of the frequency response of the IR cameras. The photo spectrometer HR2000+ (Halma, Amersham, UK) was used to acquire the emission curve of the LED, obtaining a maximum emission wave length of 830 nm. Other parameter used to select the LEDs was the emission angle that should be as wide as possible. VSMG2700 LED presents an emission angle of ±60º that is wide enough for our application. Despite the 12 cameras and the active markers some data can be lost due to the dead angles. Therefore, Motive software integrates all the camera data and in the cases of missed data, interpolates and filter the adjacent data to provide a smoothed signal.

Regarding hardware powering, a RS PRO high capacity rechargeable battery (Electrocomponents, London, UK) has been selected. It was disassembled and placed in a 1593QBK (dimensions 112 mm x 66 mm x 28 mm) waterproof box (Hammond Manufacturing Ltd., Guelph, Canada) that was firmly attached to the ski, behind the boot, including the IMU, processing and communication electronics as well as shown in Figure 3. The power bank has a 3.7 Ah lithium-ion rechargeable battery. For wireless linking, a HC-05 programmable Bluetooth) module (Guangzhou HC information technology Co., Ltd., Guangzhou, China) has been used to send data from the IMU to the computer. Each IR LED consumes 50 mA, the IMU board consumes about 20 mA and the Bluetooth module, 50 mA. Therefore, the system has an autonomy of more than 10 hours.

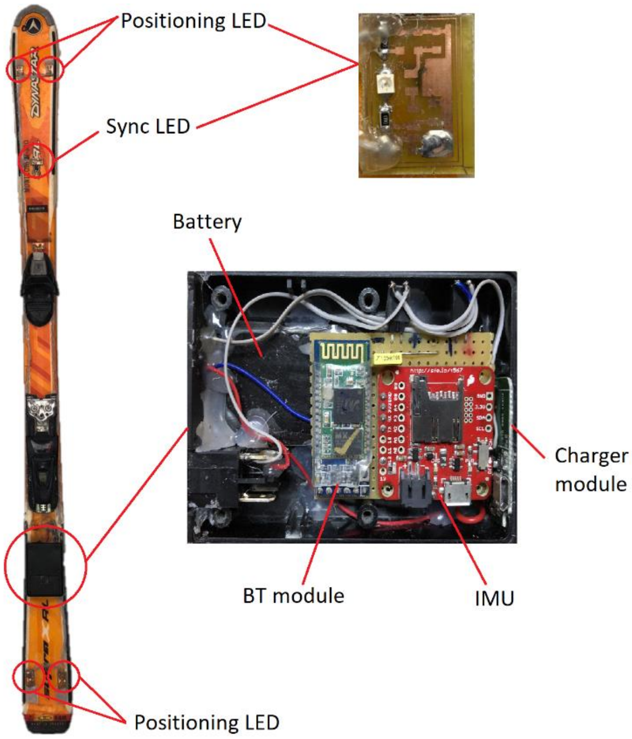

Figure 3. Developed system showing a photo of the ski with the 4 positioning LEDs, the LED for synchronization and the small waterproof box including the IMU board, the Bluetooth module and the rechargeable battery.

2.2. *Test protocol*

A participant of 25-year-old male expert skier (height: 174 cm; mass: 70 kg) skied during several sessions wearing the systems. The measurement process involved the following steps:

1. 3D cameras calibration. Previous to the recording, it is necessary a calibration of the system to set the space and the ground plane where the activity will take part in, according to the Motive software documentation [14].

2. IMU zeroing: The skier stood on a flat platform with a slope of 0 degrees during 10 seconds, in order to establish the zero level for gyroscope and accelerometer calibration. In the next section, the importance of this step will be pointed out, showing data drift with and without it.

3. Synchronization marks: To synchronize the IMU and the 3D camera system, the skier jumped at the beginning and end of the test as was used by Martinez, A et al., [8]. In addition, to check that the mark generated by the sync LED was correct, the sync LED turned off when the IMU-based system begins to collect data providing a visible benchmark in the 3D camera recording.
4. The participant began to ski while the cameras collected the position and inertial angles of both skis and the IMUs sent inertial angles and 3D accelerations data to the computer. To perform periodic turns, the start of each turn was marked with a metronome. The skier listened to the metronome signal through a Bluetooth headset. The cadence was set at 40 turns per minute, 1.5 s per turn cycle, based on average duration of giant slalom turns [15]. The skier made continuous turns for 10 or 5 minutes with a speed of 20 km/h and a slope of 12º. Two different tests were performed in these conditions:

    a. Long-term tests for studying the data drift of IMU with a duration of 10 minutes.
    b. Short-term tests (5 minutes) for the rest of studies.

2.3. Data analysis

First, to perform the data analysis, inertial angles obtained by the proposed system and by the video system should be compared. To do that, video system data needed to be denormalized and filtered:

1. The information from the cameras is denormalized to be able to compare and relate with the IMU's inertial angles. This was necessary because the 3D photogrammetric system data was given normalized between -1 and 1, and the inertial angles provided by the IMU were obtained between 0 and 360 degrees.
2. To avoid comparing between invalid data, samples showing a deviation greater than 20% were replaced by an average of ten previous and subsequent samples.
3. Then, the moving average of twenty samples was calculated.

Equation 1 shows the Pearson correlation coefficient (PCC) used to check the correlation between the inertial angles from the video system and the IMU board [16]:

$$\rho_{X,Y} = \frac{cov(X,Y)}{\sigma_X \sigma_Y} \tag{1}$$

where cov is the covariance between the magnitude X and Y, σ_X is the standard deviation of X and σ_Y is the standard deviation of Y. The concordance correlation coefficient (Lin CCC) was also calculated according Equation 2 [17]:

$$\rho_c = \frac{2\rho\sigma_x\sigma_y}{\sigma_x^2 + \sigma_y^2 + (\mu_x - \mu_y)^2} \tag{2}$$

where μ_x and μ_y are the averaged values of X and Y, and σ_x^2 and σ_y^2 are the corresponding variances. ρ is the correlation coefficient between the two variables. Whereas the ordinary correlation coefficient (Pearson's) is immune to whether the biased or unbiased versions for estimation of the variance is used, the concordance correlation coefficient is not.

Root Mean Square Error (RMSE) was also obtained to measure the correlation between the signals (see Equation 3) [18]:

$$RMSE = \sqrt{\overline{(f-o)^2}} \quad (3)$$

where f were the expected values (IMU data) and o the considered valid angles (Optical motion capture data).

Finally, the coefficient of determination, R^2, was calculated as the squared difference between the y-value estimated for each point and its actual y-value in a linear least square's regression. The sum of these squared differences is called the residual sum of squares, ssresid. Let consider sstotal the total sum of squares. Then, regression sum of squares, ssreg, can be obtained as ssreg= sstotal - ssresid. The smaller the residual sum of squares, compared with the total sum of squares, the larger the value of the coefficient of determination, R^2, which is an indicator of how well the equation resulting from the regression analysis fits both data set:

$$R^2 = \frac{ssreg}{sstotal} \quad (4)$$

To complete the information about the skier's performance, the acceleration module in the xy plane was obtained from the IMU accelerometer. These acceleration data can also be considered as complementary to those given by the 3D photogrammetric system, where accelerations were not available. The moving average of twenty samples was applied to smooth these data. The acceleration of the z direction was not relevant in this study.

3. Results

In this section, the impact of the IMU zeroing procedure in the drift data to determine the reliability of the proposed system as a function of the test duration has been initially tested. Moreover, the correlation of the inertial angles obtained from the video system and our wireless compact system are shown. After system validation, inertial angles and acceleration data were combined to assess preliminary this test's skiing technique.

Long-term tests were carried out to study the angular drift generated by the IMU with and without previous IMU zeroing. These 10 minute tests showed clear differences among parameters' drifts. Table 1 shows the measured angular ranges and time drifts of inertial angles without and with the application of the IMU zeroing procedure. A significant reduction of time drift can be observed when IMU zeroing procedure is carried out, with a reduction factor between 0.03 (yaw) and 0.28 (roll). Assuming an absolute angular drift of 2º as a tolerable limit, according to a previous work [19], our IMU-based system can provide acceptable results during 15 minutes in the worst case (roll), that is a remarkable system feature. Consequently, hereafter the IMU zeroing procedure was always applied in the rest of performed test.

Table 1. Experimental angular ranges and time drifts of inertial angles without and with IMU zeroing.

Inertial angle	Range (°)	Drifts without IMU zeroing	Drifts with IMU zeroing
Yaw	85°	2.30 ± 0.024°/min	0.071 ± 0.031°/min
Pitch	75°	0.21 ± 0.004°/min	0.085 ± 0.016°/min
Roll	30°	0.46 ± 0.023°/min	0.129 ± 0.026°/min

Additional tests of shorter duration were carried out to calculate the correlation between the inertial angles measured by our IMU-based system and those from the video analysis system. The results of direct comparisons can be observed in Figure 4 for the three angles, showing good agreements.

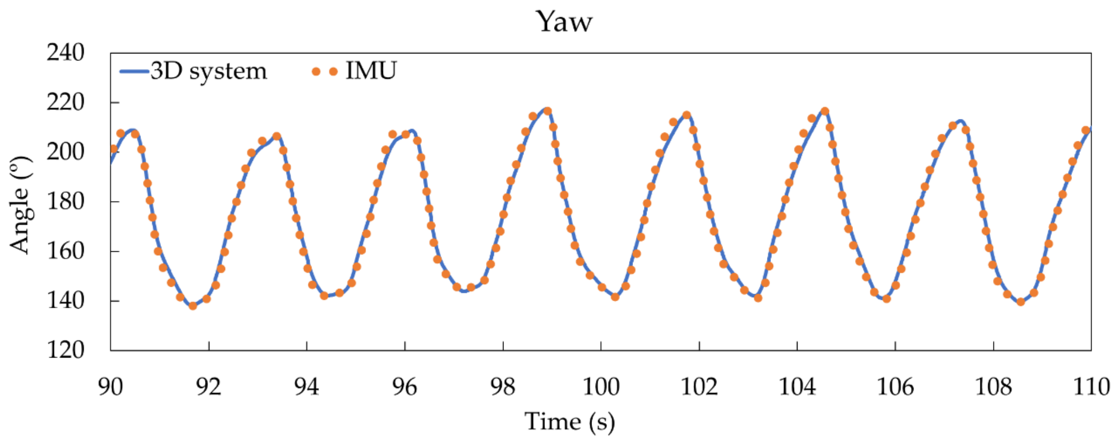

(a)

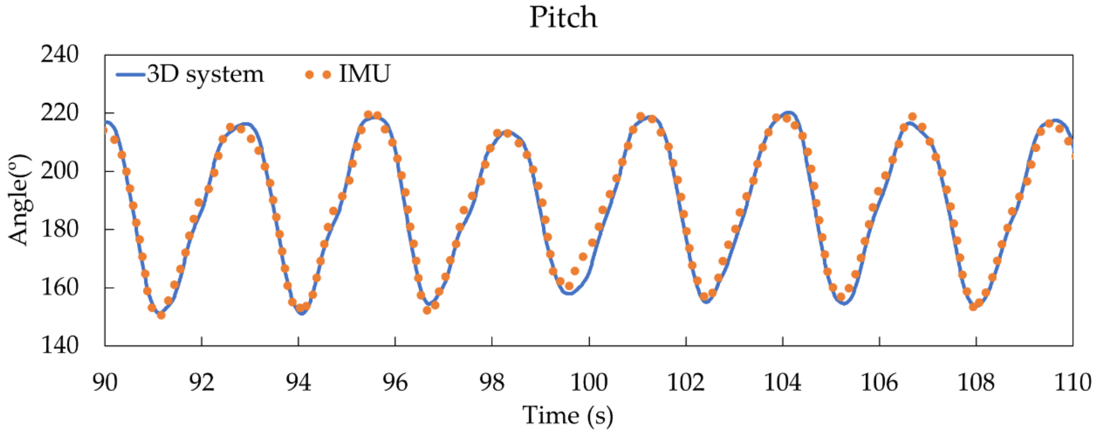

(b)

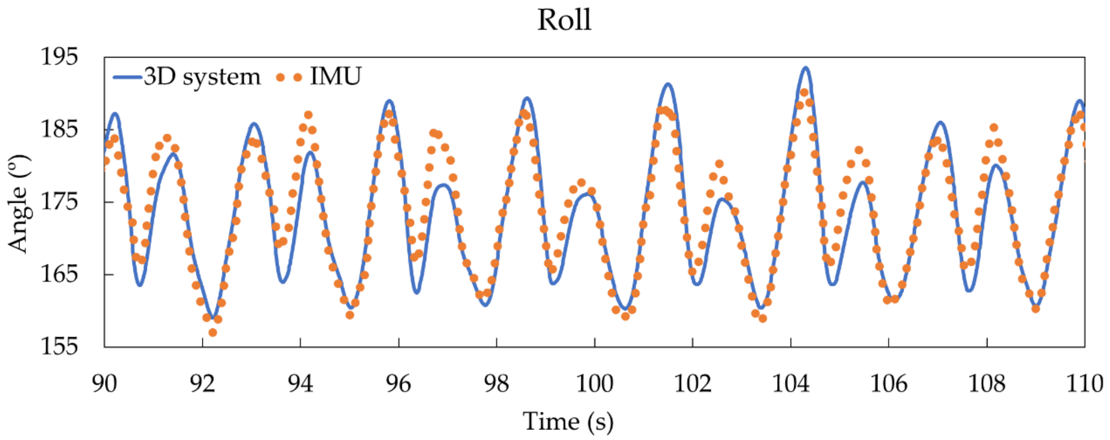

(c)

Figure 4. Comparison of IMU-based system and video system data. Yaw angle (a), pitch angle(b) and roll angle (c).

To quantify the comparisons depicted in Figure 4, the different correlation coefficients are shown in Table 2. A good correlation has been obtained between both data sets, therefore, we can consider validated our system with respect to the inertial angle gathering.

Table 2. Correlation coefficients of the inertial angles.

Angle	Pearson	Lin CCC	RMSE%	R^2
Yaw	0.9959	0.9943	3.0944	0.9935
Pitch	0.9854	0.9829	5.2098	0.9711
Roll	0.9222	0.9168	9.0483	0.8502

A polished skier`s turn technique is essential for a correct skiing performance. Therefore, aiming at shedding light on this issue, the acceleration data have been added to the inertial angles to asses the turning technique, highlighting its kinematics characteristics. The lateral angle of the ski and the acceleration of the ski will determine how each turn is made. These data can provide relevant information about when and at what angle the skier can speed up.

Figures 5 and 6 show synchronised data obtained by our designed IMU-based system around beginning and end of a turn respectively. Results represented are the most relevant inertial angles, yaw and roll, and the acceleration modulus in the xy plane for left and right ski. Vertical lines point out the exact times corresponding to the photos. A maximum and minimum of xy acceleration are marked in Figures 5 and 6 respectively.

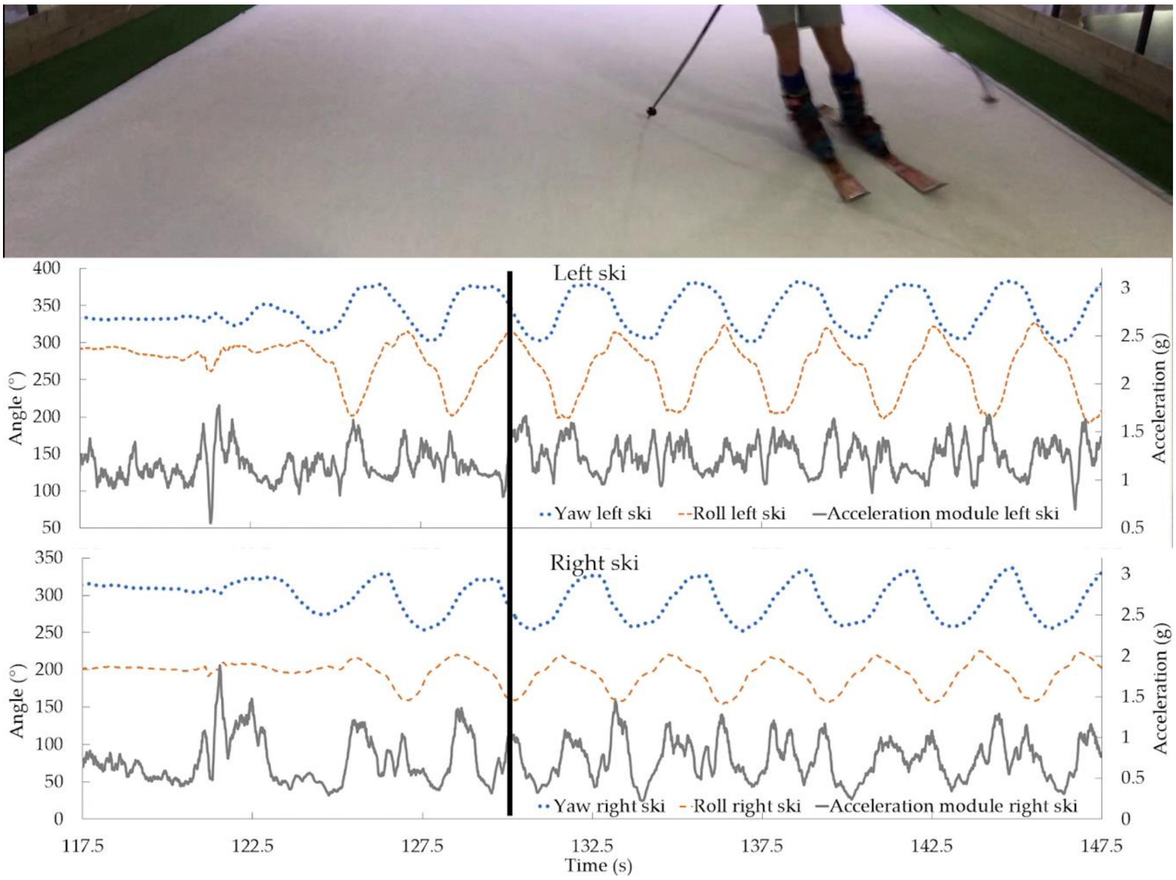

Figure 5. Synchronised yaw, roll and acceleration modulus in the xy plane for each ski around the beginning of a turn. Vertical line shows the point of maximum xy acceleration of a turn.

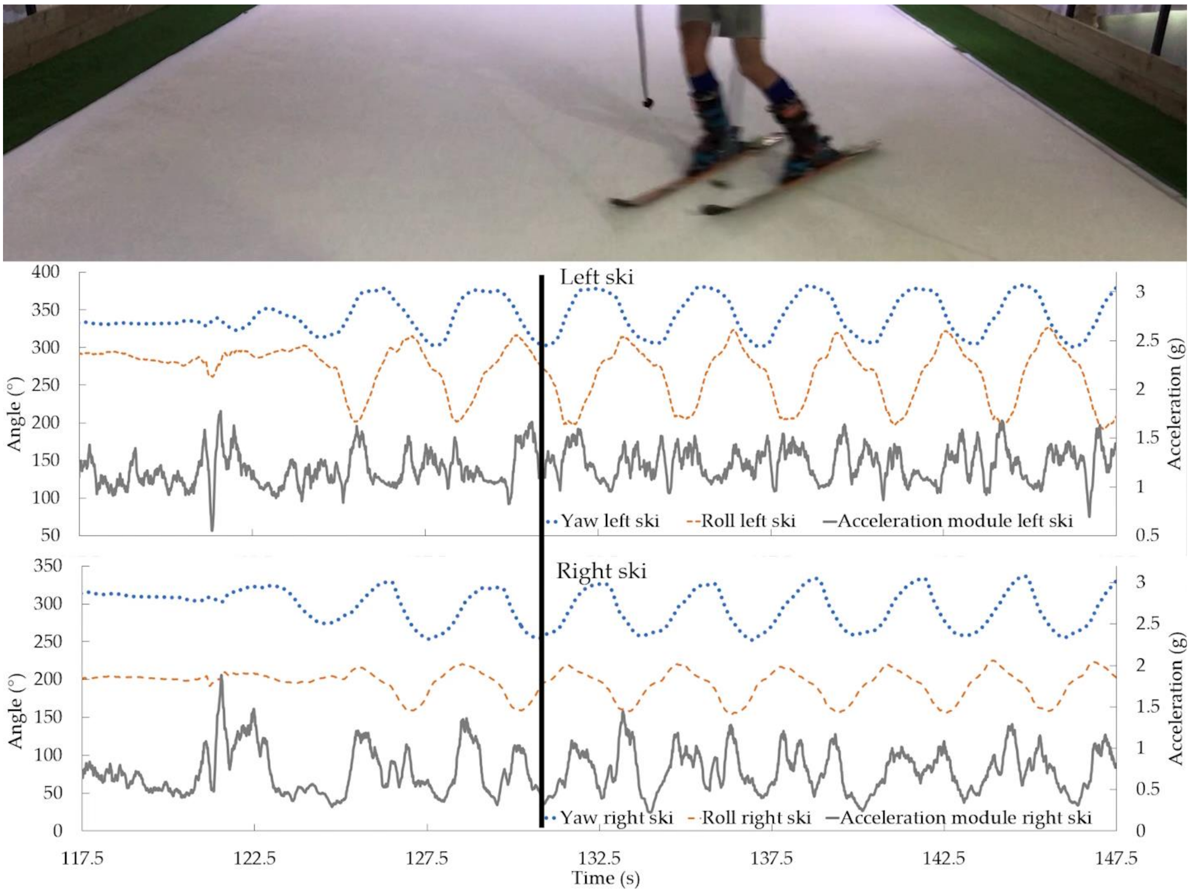

Figure 6. Synchronised yaw, roll and acceleration modulus in the xy plane for each ski around the end of a turn. Vertical line shows the point of minimum xy acceleration of a turn.

4. Discussion

The aim of this study was to develop and verify the feasibility of the designed IMU-based system for monitoring the turn technique in alpine skiing. One of the priorities of our design was the simplicity both of the design and deployment of this evaluation system. Let us remember that the IR LEDs were placed for improvement detection of the gold standard system and synchronization purposes. Consequently, those optoelectronic components would not be included in the final system which only comprises the waterproof box, with the electronic board inside, attached to each ski, and the software for processing and presentation of data. Hardware dimensions can be downsized to 50 mm x 40 mm x 10 mm with minimum weight of 15 g without battery. The battery can be adapted to the required test duration; therefore, a lighter and smaller battery could be used instead of the one here mentioned. Although hardware was located in the ski's rear area behind the boot to reduce water splashed, it can be placed at any different part of the ski.

Another advantage of wireless IMU-based systems is that they not are affected by the data loss due to blind spots of any camara system. This can happen when IR marked (passives or actives) are shielded by the skier body's movement or get wet.

Therefore, with IMU-based systems, data loss is minimized. Furthermore, the selected electronic board has a slot to insert a micro SD memory card for continuous data logging. This would reduce the information loss caused by a Bluetooth link failure.

The results demonstrate that the proposed IMU-based system can provide low-drifted data for more than 15 minutes of continuous usage in the worst case (roll). If only the most relevant inertial angles, for this kind of movement, were considered (yaw and pitch), this duration could be extended to 22 minutes assuming with an angular drift tolerance of 2º. This has been possible thanks to the simply and short IMU zeroing procedure available prior to the test. Moreover, this zeroing procedure is automatically performed when powering up the system, remaining still on a flat surface for 10 second.

Regarding the inertial angles, they showed a good agreement between the signals obtained by the proposed system and those by the gold standard (see Table 1). An excellent correlation was observed between yaw measured by the IMU and by the optical system with a Pearson's correlation coefficient of 0.9959. For pitch a good correlation is obtained while for the roll the calculated correlation is acceptable. The better correlation of yaw and pitch can be explained due to the higher angular range of this magnitude compared to roll. Given the kinematics characteristics of the movement under study, a skiing turn, angular variations are significant larger in the xy plane, corresponding to yaw and pitch, than in the z direction (roll). Therefore, the shorter the range, the more affected by uncertainty sources in both systems, resulting in a lower, although acceptable, correlation. As a results, the accuracy of the angle data obtained by our IMU system implemented on the skis are similar to the accuracy values obtained in the studies by Martinez et al,. (95.3-99.7% comparing IMU system with 2D video) [8] and Neuwirth et al,. (89-95% comparing IMU system with GNSS) [9], regardless of the fact that in these studies, the IMU was placed in the ski boot. This validates the use of IMUs for performance monitoring in alpine skiing.

An additional improvement compared to previous systems, it is that our system provides reliable results for longer periods of time without significant drift (Figure 4). In fact, magnetometer data allows the system correcting the gyroscope's drift. The longest test that has been carried out has been 650 seconds without observing a significant drift. The speed of the simulator was set at 20 km/h, this means that a descent of 3600 meters was monitored. The tests in Figures 5-7 had a duration of 255 seconds at a speed of 20 km/h, corresponding to a descent of about 1400 meters. A professional skier reaches speeds above 80 km/h, consequently, the system can be used for at least 10 minutes -about 13 kilometres- without drifting.

All these features would allow the system to be transferred to real tests in snow without making changes. On the track, a study of a large number of turns can be made in real conditions.

5. Conclusions

A compact, wireless and IMU-based system has been designed and validated to study the alpine skiing technique. Excellent agreement of inertial angles with a 3D camera system has been obtained with Pearson coefficients above 0.92. Additionally, the contribution of acceleration data allows to an exhaustive analysis of skiing performance and makes possible to the coach to create a specific training to improve the technique and to correct the skier's movements. This feedback can be in real time due to wireless connection (Bluetooth link) with a smartphone. Moreover, completing the IMU zeroing process, that only takes 10 seconds and without participant assistance, long term skiing tests can be undergone longer than 10 minutes. Given the system location, the system comfortability can be assured during skiing and its features make possible further research.

References

1. Reid, R.C. *A kinematic and kinetic study of alpine skiing technique in slalom*; 2010; ISBN 978-82-502-0440-9.

2. Spörri, J.; Kröll, J.; Schwameder, H.; Müller, E. Turn characteristics of a top world class athlete in giant slalom: A case study assessing current performance prediction concepts. *Int. J. Sport. Sci. Coach.* **2012**, *7*, 647–659, doi:10.1260/1747-9541.7.4.647.

3. Supej, M.; Kugovnik, O.; Nemec, B. Kinematic determination of the beginning of a ski turn. *Kinesiol. Slov.* **2003**, *9*, 11–17.

4. Takeda, M.; Miyamoto, N.; Endo, T.; Ohtonen, O.; Lindinger, S.; Linnamo, V.; Stöggl, T. Cross-country skiing analysis and ski technique detection by high-precision kinematic global navigation satellite system. *Sensors (Switzerland)* **2019**, *19*, doi:10.3390/s19224947.

5. Stöggl, T.; Welde, B.; Supej, M.; Zoppirolli, C.; Rolland, C.G.; Holmberg, H.C.; Pellegrini, B. Impact of incline, sex and level of performance on kinematics during a distance race in classical cross-country skiing. *J. Sport. Sci. Med.* **2018**, *17*, 124–133.

6. Adesida, Y.; Papi, E.; McGregor, A.H. Exploring the role of wearable technology in sport kinematics and kinetics: A systematic review. *Sensors (Switzerland)* **2019**, *19*, doi:10.3390/s19071597.

7. Camomilla, V.; Bergamini, E.; Fantozzi, S.; Vannozzi, G. Trends supporting the in-field use of wearable inertial sensors for sport performance evaluation: A systematic review. *Sensors (Switzerland)* **2018**, *18*, doi:10.3390/s18030873.

8. Martínez, A.; Brunauer, R.; Venek, V.; Snyder, C.; Jahnel, R.; Buchecker, M.; Thorwartl, C.; Stöggl, T. Development and Validation of a Gyroscope-Based Turn Detection Algorithm for Alpine Skiing in the Field. *Front. Sport. Act. Living* **2019**, *1*, doi:10.3389/fspor.2019.00018.

9. Neuwirth, C.; Snyder, C.; Kremser, W.; Brunauer, R.; Holzer, H.; Stöggl, T.

Classification of alpine skiing styles using GNSS and inertial measurement units. *Sensors (Switzerland)* **2020**, *20*, 1–22, doi:10.3390/s20154232.

10. Snyder, C.; Martínez, A.; Brunauer, R.; Stöggl, T. Validation of a Wearable System for Edge Angle Estimation during Alpine Skiing. *to be Publ. "Science Ski. VIII"* 2020, 1–8.

11. Fasel, B.; Praz, C.; Kayser, B.; Aminian, K. Measuring spatio-temporal parameters of uphill ski-mountaineering with ski-fixed inertial sensors. *J. Biomech.* **2016**, *49*, 3052–3055, doi:10.1016/j.jbiomech.2016.06.017.

12. Martínez, A.; Jahnel, R.; Buchecker, M.; Snyder, C.; Brunauer, R.; Stöggl, T. Development of an automatic alpine skiing turn detection algorithm based on a simple sensor setup. *Sensors (Switzerland)* **2019**, *19*, 1–12, doi:10.3390/s19040902.

13. Yu, G.; Jang, Y.J.; Kim, J.; Kim, J.H.; Kim, H.Y.; Kim, K.; Panday, S.B. Potential of IMU sensors in performance analysis of professional alpine skiers. *Sensors (Switzerland)* **2016**, *16*, 1–21, doi:10.3390/s16040463.

14. Optitrack Motive documentation wiki. (Ver 2.2) Available online: https://v22.wiki.optitrack.com/index.php?title=Motive_Documentation (accessed on Jan 8, 2021).

15. Spörri, J.; Kröll, J.; Fasel, B.; Aminian, K.; Müller, E. Course Setting as a Prevention Measure for Overuse Injuries of the Back in Alpine Ski Racing: A Kinematic and Kinetic Study of Giant Slalom and Slalom. *Orthop. J. Sport. Med.* **2016**, *4*, 1–8, doi:10.1177/2325967116630719.

16. Society, T.R. Note on Regression and Inheritance in the Case of Two Parents Author (s): Karl Pearson Source : Proceedings of the Royal Society of London , Vol . 58 (1895), pp . 240-242. **2015**, *58*, 240–242.

17. Lin, L.I. A Concordance Correlation Coefficient to Evaluate Reproducibility Author (s): Lawrence I-Kuei Lin Published by : International Biometric Society Stable URL : http://www.jstor.org/stable/2532051 REFERENCES Linked references are available on JSTOR for thi. *Biomatrics* **1989**, *45*, 255–268.

18. Armstrong, J.S.; Collopy, F. Error measures for generalizing about forecasting methods: Empirical comparisons. *Int. J. Forecast.* **1992**, *8*, 69–80, doi:10.1016/0169-2070(92)90008-W.

19. Yoshioka, S.; Fujita, Z.; Hay, D.C.; Ishige, Y. Pose tracking with rate gyroscopes in alpine skiing. *Sport. Eng.* **2018**, *21*, 177–188, doi:10.1007/s12283-017-0261-y.

3.3 Microfluidics

Finally, results in the microfluidic research line will be presented. As in the previous sections, the developed sensing platform will be detailed first, followed by the results obtained with it.

3.3.1 Capacitive platform for microfluidics study

In short, the basics of the sensing platform (Figure 38) consist of a pair of metal parallel electrodes positioned below the strip in the path of the advancing imbibition front. As the paper strip becomes wet, the capacitance between these electrodes changes, allowing for accurate and real-time measurement of the process without the need for video cameras or external flow sensors. The capacitive sensor AD7746 (Analog Devices Inc., Cambridge, MA, USA) was employed to measure the capacitance change due to the liquid wicking in the paper strip. It is a 24-bit, 2-channel capacitive to digital converter capable of measure capacitance at 32 kHz achieving an accuracy of 4 fF with a full-scale range of 8 pF. Moreover, a ±4 pF capacitance offset can be added to adjust the measuring range. Sampling frequency can also be selected from 10 to 90 Hz, and its communication with the controller is via I2C serial interface. This chip includes an on-temperature sensor with a resolution of 0.1 °C and accuracy of ±2. °C. As microcontroller an Arduino Nano (Chiasso, Switzerland) was selected. This board use the ATmega 328 microcontroller.

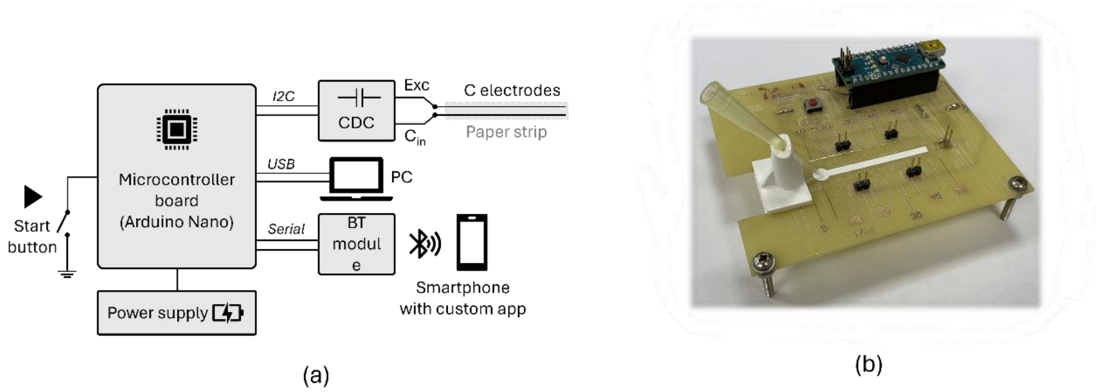

Figure 38. Capacitive sensing platform. (a) Electronic schematic; (b) photo including paper strip and accessory for repetitive water intake [97].

The ATmega328, part of Microchip's AVR microcontroller family, stands out for its versatility and efficiency across a wide range of embedded applications. Its RISC architecture enables efficient execution of a reduced set of instructions, resulting in optimal performance. With a clock speed of up to 20 MHz, this microcontroller is capable of fast and precise operations. In terms of memory, the ATmega328 offers 32 KB of Flash memory for code storage, making it ideal for developing complex applications. Additionally, it features 2 KB of Static Random-Access Memory (SRAM) and 1 KB of Electrically Erasable Programmable Read-Only Memory (EEPROM) for temporary and non-volatile data storage, providing flexibility in data handling. One of the standout features of the ATmega328 is its wide range of integrated peripherals. These include multiple timers/counters, serial communication interfaces such as Universal Synchronous/Asynchronous Receiver/Transmitter (USART), Serial Peripheral Interface (SPI), and Inter-Integrated Circuit (I2C), as well as a 10-bit Analog-to-Digital Converter (ADC) for precise analog data acquisition. Furthermore, it has configurable General Purpose Input/Output (GPIO) ports for interaction with external devices. Energy efficiency is another strong point of the ATmega328, making it suitable for applications with strict power consumption requirements or battery-powered devices. This feature makes it a popular choice for portable devices and standalone systems.

In terms of programming, the ATmega328 is compatible with a variety of programming languages, including C and C++, and can be programmed using standard tools such as the Arduino Integrated Development Environment or AVR Studio. Additionally, its compatibility with the Arduino open-source software ecosystem and libraries facilitates project development and code reuse. In summary, the ATmega328 is a versatile, powerful, and efficient AVR microcontroller suitable for a wide range of embedded applications requiring data processing, control, and monitoring. Its combination of features makes it a popular choice among embedded system designers and developers. These features led to the selection of the ATmega328 for the development of this sensor platform.

In this case, a publication and a presentation at an international conference have been the result so far. In the next section we will discuss the improvements that have been made to the system and future perspectives.

3.3.2 Capacitive platform: actuators for flow controlling

After the development of the microcontrolled platform for microfluidics [97], several experiments and modifications have been carried out to include actuators and increase the sensitivity in order to achieve a system with enhanced capabilities. In terms of actuators, two methodologies have been tested: the inclusion of a heater, which

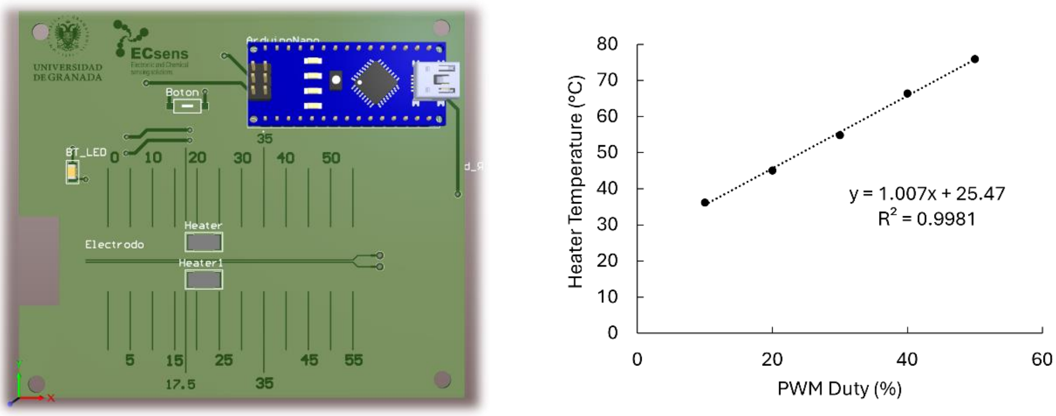

(a) (b)

Figure 39. *(a) Development of the microfluidic platform with the inclusion of two heaters; (b) calibration curve of the temperature as function of duty cycle.*

together with the wax barrier previously tested or the use of NIPAN as a storage valve, enables stopping or permitting the flow; and the use of electro-osmosis to accelerate and decelerate the advancement of the liquid.

For the heater inclusion, two holes with the size of an SMD 2512 resistor (6.35 x 3.2 mm) were added to the plate. As Figure 39a shows, the holes were drilled so that the paper could be heated from both sides without breaking the measurement electrodes. Resistors with this type of encapsulation tolerate up to 1 W of power, which is enough to obtain the temperature required for our application. A characterization was made to study the power consumption and temperatures using resistors between 22 Ω and 82 Ω, being 47 Ω the final choice. A P-type MOSFET transistor was added to feed the resistors considering the current limitations of the Arduino pins. To control it, a PWM signal was used to modify the heater temperature by adjusting the duty cycle. Figure 40b shows the temperature obtained as a function of the duty.

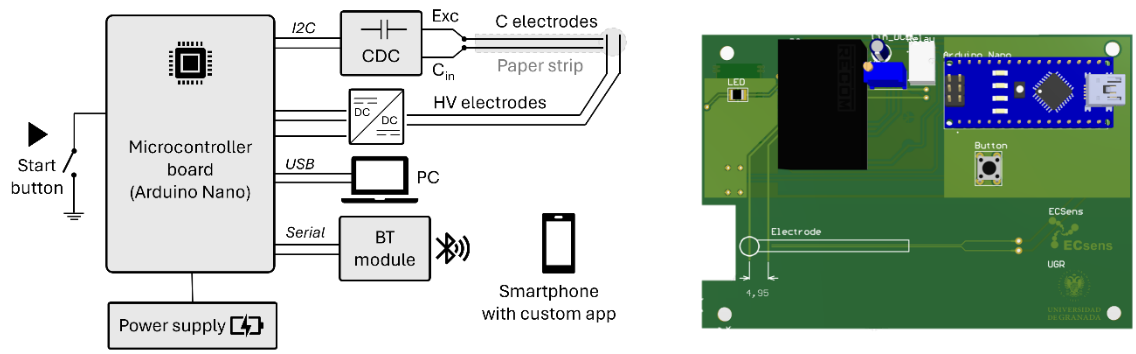

(a) (b)

Figure 40. *Microfluidic platform, DC-DC converter version. (a) comprehensive schematic; (b) board design.*

On the other hand, electroosmosis is a technique commonly used to control flow in microfluidic systems [98]. In this process, an electric field is applied across a microfluidic channel containing a conductive liquid, such as a saline solution or an electrolyte. This electric field induces a flow of liquid along the channel, which can accelerate or decelerate depending on the polarity and intensity of the applied electric field. When an electric current is applied, the ions in the solution move towards the opposite electrode under the influence of the electric field. By changing the direction or intensity of the electric field, it is possible to control the flow velocity and direction in the microfluidic system.

For this purpose, a new electronic board was designed (Figure 40). In this version a RECOM R05-100B (RECOM Power) DC-DC converter was added. It consists of a 3W regulated high output voltage (41 – 125 V) with nominal input of 5 V. In addition, a G6K-2P-Y-DC3 relay from OMROM was added to provide the capability of reversing the polarity on the high voltage electrodes. All the new components are controlled by the Arduino Nano.

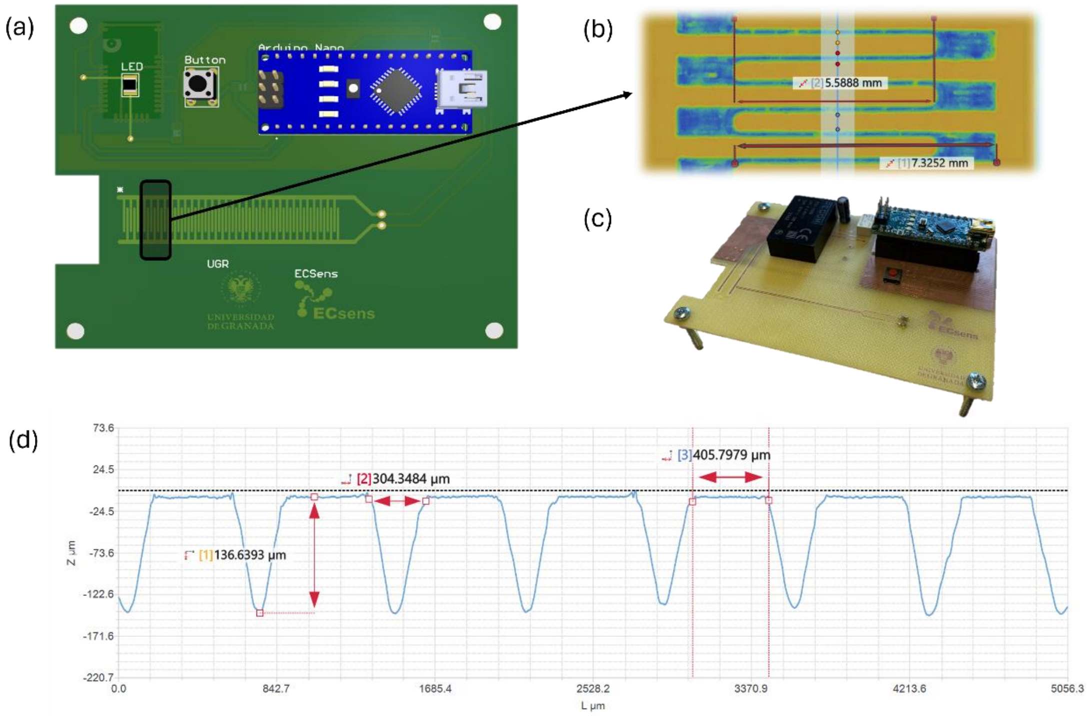

Figure 41. *Capacitive platform, EID version. (a) 3D design; (b) and (d) dimensions of the EID obtained using the optical profilometer; (c) picture of the system.*

Furthermore, the shape of the capacitive electrodes was modified to increase the sensitivity. With this objective, the design was switched from a pair of parallel copper electrodes with a width of 200 µm and a gap of 300 µm to the interdigital electrodes (IDE) depicted in Figure 41. The parallel electrodes had an initial capacitance of 1.71 ± 0.01 pF, while in the new configuration the base capacitance has been increased to 17.55 ± 0.01 pF. Moreover, the measured capacitance increase due to paper wetting has changed from around 0.8 pF to 2.5 pF, thereby increasing the sensitivity of the system by a factor over 3. The designed IDE consists of two interlocking comb-shaped arrays of 32 copper electrodes with a width of 200 µm and a gap of 300 µm. Although the cooper plane has only a thickness of 35 µm, due to the circuit plotter, the depth to which the cutter reaches is 135 µm; in contrast, the designed thickness and gap of the electrodes was 400 µm and 300 µm, respectively, and the PCB was found to match the design.

It is worth noting that during the time these tests were conducted, the major challenge we had was the repetitiveness of the tests. Several actions were taken to address these issues:

- Paper wetting. The way of wetting the paper was one of the major issues encountered, which was influenced by several parameters including initial pressure, overflow, and the paper's capacity for liquid absorption, among others. After numerous tests, the proposed solution was the development of a 3D piece serving as a support for the micropipette nozzle. This allowed for precise collection of the required amount of liquid to fully wet the paper strip.
- Lifetime of double-sided tape. As detailed in section 4.11, where the article published on this topic is presented, for the experimental setup, the paper strips are attached to the platform using double-sided adhesive tape. Simulations and subsequent tests have revealed that the condition and thickness of this adhesive layer significantly impacts the sensitivity of the system. Therefore, a protocol was established whereby the first 5 tests must be discarded, after which 20 to 30 tests could be performed before the adhesive had to be replaced again.
- Reuse of paper strips. It was also observed that paper strips can be reused until they deteriorate, provided that the solutions used leave no residues.
- Orientation of paper fibres. Another aspect studied was the orientation of the paper fibres. The repeatability among different paper strips is influenced, among other factors, by the correct direction of alignment of the cellulose fibres that make up the paper. For this reason, all paper strips were cut to ensure that the advancing liquid front aligned with the same direction of the cellulose fibres.

As a conclusion, following the development and validation of the capacitive flow monitoring platform, two actuator systems have been developed, and the sensitivity of the system has been enhanced. We now have the basis for conducting tests with different dissolutions and analytes that require flow control. In addition, owing to the higher sensitivity of the platform using the EID, it is possible to differentiate between different liquids. This paves the way for new tests, offering additional insights into the solutions while enabling precise flow control.

3.3.3 Publication 4

Capacitive platform for real-time wireless monitoring of liquid wicking in a paper strip

Isidoro Ruiz-García[a,b,d], Pablo Escobedo[a,b,d], Celia E. Ramos-Lorente[b,c], Miguel M. Erenas[b,c], Luis F. Capitán-Vallvey[b,c], Miguel A. Carvajal[a,b,d], Alberto J. Palma[a,b,d,*], Nuria López-Ruiz[a,b,d]

* Corresponding authors
a Electronic and Chemical Sensing Solutions (ECsens), CITIC-UGR, Department of Electronics and Computer Technology, University of Granada (UGR), 18071 Granada, Spain
E-mail: ajpalma@ugr.es
b Unit of Excellence in Chemistry Applied to Biomedicine and the Environment of the University of Granada, Granada, Spain
c Electronic and Chemical Sensing Solutions (ECsens), Department of Analytical Chemistry, University of Granada (UGR), 18071 Granada, Spain
d Sport and Health University Research Institute (iMUDS), University of Granada (UGR), 18071 Granada, Spain

- Lab Chip, 2023,23, 4092-4103. https://doi.org/10.1039/D3LC00368J
- Journal Impact Factor (2022): 6.1
- Rank by Journal Citation Indicator (JCI): Q1 in category INSTRUMENTS & INSTRUMENTATION (7/63)

Abstract

Understanding the phenomenon of liquid wicking in porous media is crucial for various applications, including the transportation of fluids in soils, the absorption of liquids in textiles and paper, and the development of new and efficient microfluidic paper-based analytical devices (μPADs). Hence, accurate and real-time monitoring of the liquid wicking process is essential to enable precise flow transport and control in microfluidic devices, thus enhancing their performance and usefulness. However, most existing flow monitoring strategies require external instrumentation, are generally bulky and unsuitable for portable systems. In this work, we present a portable, compact, and cost-effective electronic platform for real-time and wireless flow monitoring of liquid wicking in paper strips. The developed microcontroller-based system enables flow and flow rate monitoring based on the capacitance measurement of a pair of electrodes patterned beneath the paper strip along the liquid path, with an accuracy of 4 fF and a full-scale range of 8 pF. Additionally to the wired transmission of the monitored data to a computer via USB, the liquid wicking process can be followed in real-time via Bluetooth using a custom-developed smartphone application. The performance of the capacitive monitoring platform was evaluated for different

aqueous solutions (purified water and 1 M NaCl solution), various paper strip geometries, and several custom-made chemical valves for flow retention (chitosan-, wax-, and sucrose-based barriers). The experimental validation delivered a full-scale relative error of 0.25%, resulting in an absolute capacitance error of ± 10 fF. In terms of reproducibility, the maximum uncertainty was below 10 nl/s for flow rate determination in this study. Furthermore, the experimental data was compared and validated with numerical analysis through electrical and flow dynamics simulations in porous media, providing crucial information on the wicking process, its physical parameters, and liquid flow dynamics.

Introduction

Liquid wicking in porous media refers to the process whereby capillary forces draw a liquid into a porous material, driven by its surface tension. The rate of liquid wicking in porous media is dependent on several factors, including the surface tension of the liquid, the pore size and shape of the porous material, the wetting properties of the material, and the geometry and orientation of the porous material[1–3]. This phenomenon is significant in a wide range of applications, including the transport of fluids in soils, the design of microfluidic devices, and the absorption of liquids in textiles and paper[4–6].

Considerable effort has been invested in comprehending the dynamics of liquid imbibition through porous media, owing to the three-phase complex formation of solid−liquid and −gas interfaces. In 1856, Darcy conducted the first experimental investigation of liquid flow in porous media[7]. His model assumes that flow within a porous medium is driven solely by capillary pressure gradient. In 1921, two researchers established a relationship between the capillary height and the rising time of a liquid in porous media, popularly known as the Lucas−Washburn (LW) equation[1,2]. Various studies have utilized the LW model to understand the physics of liquid wicking in porous media. The LW model scales the liquid wicking distance (L_{lf}) with time (t) as $L_{lf} \sim t^{1/2}$. However, both Darcy’s law and the LW equation make simplifying assumptions that restrict their applicability. The LW equation assumes a constant capillary diameter throughout the length of the paper, and it does not account for changes in channel geometry or the effects of evaporation. Hence, several modifications have been reported to make both models more accurate. These modifications include the incorporation of different effects such as gravity[8], liquid evaporation[9], and fibre swelling[10–12], among others. Another approach to address this phenomenon is based on Richards’s equation[13]. This equation can also be effectively solved with numerical simulators, which have been precisely employed in recent works to shed light on the wicking process in porous media, including several of the aforementioned effects[14–16]. A recent review compiles most of the advances in this area[17].

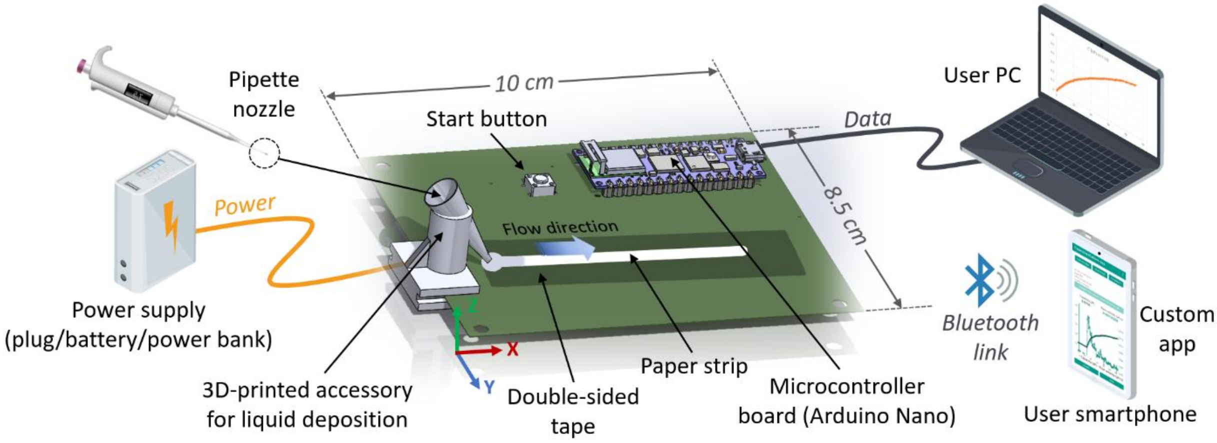

***Figure 1**. Overview of the capacitive platform for liquid wicking monitoring.*

Liquid wicking in porous media plays a crucial role in microfluidic paper-based analytical devices (μPADs). The use of μPADs has several advantages over traditional diagnostic techniques, such as being low cost, ease of use, and portable[18–22]. The wicking of the liquid through the porous matrix in μPADs promotes the transport of the sample and facilitates the mixing of the sample with reagents, enabling the detection of target analytes. μPADs have been utilized for a wide range of applications, including detection of infectious diseases, environmental monitoring, and food safety testing[22]. Understanding liquid wicking in porous media is crucial in the development of new and efficient μPADs. By optimizing the properties of the porous material, such as pore size and shape, and the composition of the reagents, the performance of the device can be enhanced, leading to more sensitive and accurate detection of target analytes[16,23–25].

Flow control is a crucial aspect of μPADs, which rely on capillary forces to manipulate and transport fluids within porous material. Effective flow control is essential to ensure that the liquid flows through the device at the desired rate and reaches the detection zone where the signal is generated. Several strategies have been reported for flow control, including paper strip geometry, mechanical manipulation, chemical modification, and electrical/magnetic/thermal actuators[5,17]. Accurate and real-time flow and flow rate monitoring is essential for useful and practical implementation of these techniques[26] as an alternative to offline flow monitoring methods based on video recording of the wicking process. This ensures precise flow control and therefore improves the performance of microfluidic devices.

External flow sensors are typically employed in systems with active liquid pumping, including close-loop feedbacks, or particle image velocimetry techniques to monitor the flow in microfluidic devices. Although effective, these external solutions are generally bulky and not suitable for portable systems[27]. On the other hand, in the last decade, some integrated flow monitoring strategies, requiring specific fabrication procedures and materials, have been reported based on cantilevers[28], magnetic composites[29], piezoelectric nanofibers[30], optical nanofibers[31], resonant membranes[32], and nanoparticles strain sensors on sealed microfluidic channels[33]. Alternatively, techniques based on electrical measurements with conducting electrodes or materials, such as electrical admittance measurements[34], electrical impedance spectroscopy[35], electrochemical sensors[36,37], and piezoresistive membranes[38], have been presented but require external instrumentation for the electrical magnitude acquisition. A study by the research group of Prof. Delamarche demonstrated a remarkable and inspiring approach for capillary-driven microfluidics in PDMS channels. The channel flow was monitored by measuring the change in a pair of longitudinally patterned metallic electrodes along the hydrophilic flow path while liquid wicking. It produced a dielectric constant change that could be easily detected by capacitive detection. This electronically-microcontrolled setup was provided with a graphical interface and a wireless link to a smartphone for real-time and in-situ data display and transmission[26].

In the present work, we have developed a portable electronic platform for real-time and wireless flow monitoring of liquid wicking in paper strips. The performance of this system was evaluated using different water solutions, paper strip geometries, and various chemical valves. Figure 1 presents a general scheme of our system, which is based on the capacitance measurement of a pair of parallel electrodes patterned beneath the paper strip along the liquid path. These electrodes were designed on a printed circuit board (PCB) along with a capacitance detector and a microcontroller board that includes a Bluetooth link. In addition, experimental capacitive transients were theoretically reproduced with a numerical simulator including both electrical and flow in porous media simulations. The full geometry of the experimental setup was included in the COMSOL Multiphysics software to perform the numerical analysis of the capacitance change of the imbibition process as a function of time. The comparison of experimental and numerical data provides fundamental information about the wicking process in terms of the physical parameters involved, such as dielectric constant, pore size, and permeability; and the flow relevant features, including the dynamics of the length of the liquid front, absorbed liquid mass/volume, and liquid mass/volume flow. To the best of our knowledge, this is the first compact system that enables monitoring of liquid wicking along an entire paper strip, providing physical information about the phenomenon through numerical simulation.

Experimental and numerical procedures

Materials and software

The electronic components were procured from RS Components supplier (Corby, UK). The printed circuit board and the capacitive electrode structure were fabricated using the computer-controlled circuit board plotter LPKF ProtoMat S100 (LPKF Laser & Electronics SE, Garsen, Germany). An accessory for a micropipette tip holder was 3D printed with a Creality CR-X 3D printer (Creality, Shenzhen,China) using polylactic acid (PLA) filament. The proposed capacitive sensing platform was validated using a precision LCR meter E4980AL (Keysight Tech., Santa Rosa, CA, USA). The dielectric constants of the paper, both dry and imbibed with purified water, were measured using a 40 Hz to 110 MHz precision impedance analyzer 4294A interfaced to the dielectric material test fixture with parallel plate electrodes, 16451B (Keysight Tech., Santa Rosa, CA, USA). The physical study of the experimental setup, including the surface morphology and texture changes of the paper strip during the wicking process, was carried out using the 3D optical profilometer SNeox (Sensofar, Barcelona, Spain). The confocal technique was configured with x5, x20, and x50 optical objectives, achieving a spatial resolution ranging from 470 to 180 nm. The features of the surface texture standard ISO 25178 were calculated by the profilometer software SensoVIEW 1.9.2. A Xiaomi Redmi Note 11S smartphone (Xiaomi Corporation, Beinjin, China) was used for videorecording during the validation of the platform, configuration, and real-time results display.

Filter paper Whatman grade 1 (Merck KGaA, Sant Louis, USA) was selected for all experiments of this work. Different paper strip shapes were obtained using a laser cutting machine (Rayjet 50 Laser Engraver, Austria). Hydrophobic double-sided adhesive tape Tesa 64621 (Tesa, Hamburg, Germany) was used to affix the paper strip to the capacitive electrodes. Purified water was produced by a TKA Microlab type II (TKA Wasseraufbereitungssysteme GmbH, Niederelbert, Germany) for the experiments to evaluate the sensing platform's performance. High molecular weight chitosan, NaCl, and sucrose were provided by Sigma-Aldrich Merck (Madrid, Spain) for the chemical experiments. COMSOL Multiphysics 6.1 (Comsol AB, Stockholm, Sweden) was employed for numerical calculations and modelling of the electrical capacitance transient and the flow dynamics of the paper strip in the wicking process. The AC/DC, microfluidics, and porous media flow modules were utilized for the

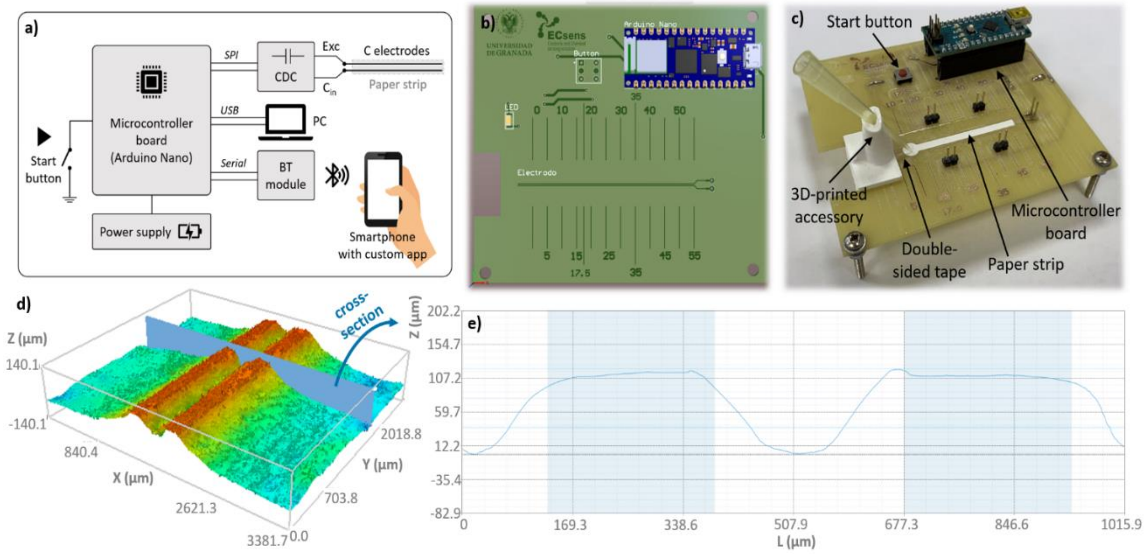

Figure 2. *Capacitive sensing platform. (a) Electronic schematic; (b) PCB layout; (c) Photo including paper strip and accessory for repetitive water intake; (d) 3D profiler image of the capacitive sensing electrodes; (e) Actual cross-section of the electrodes.*

programming of COMSOL applications, including the geometries and materials of the different experimental setups described below. The smartphone application was coded using Android Studio Dolphin (2021.3.1) as the integrated development environment (IDE). The application was designed and tested with Application Programming Interface (API) level 31 (Android 12), although it is compatible with older Android versions, API 22 (Android 5.1) being the minimum level required for functional compatibility. The open-source library MPAndroidChart was used for the visual representation of the data within the application.

Capacitive sensing platform

Our design of the electronic platform for monitoring the dynamics of liquid imbibition in a paper strip is based on tracking the capacitance change over time when wicking the liquid. As depicted in Figure 2, we have patterned a pair of metal parallel electrodes positioned below the strip in the path of the advancing imbibition front. As the paper strip becomes wet, the capacitance between these electrodes changes, allowing for accurate and real-time measurement of the process without the need for video cameras or external flow sensors. Double-sided adhesive tape is attached between the electrodes and the paper strips to fix both elements, also providing a waterproof barrier to prevent the electrodes from getting wet and causing a short-circuit, since they need to be dry for an accurate and reliable capacitance measurement. Our electronic measurement system lies on the small breadboard Arduino Nano (Chiasso, Switzerland) as the controller unit. This controller was selected for its versatility, low power consumption of 19 mA, light weight of 7 g, wireless communication and battery-powering capabilities. This unit is responsible for the configuration and data analysis of the AD7746 capacitive sensor (Analog Devices Inc., Cambridge, MA, USA), which is a 24-bit, 2-channel capacitive to digital converter employed to measure the capacitance change due to the liquid wicking in the paper strip. This capacitive sensor can measure capacitance at 32 kHz achieving an accuracy of 4 fF with a full-scale range of 8 pF. Moreover, a ± 4 pF capacitance offset can be added to adjust the measuring range. Sampling frequency can also be selected from 10 to 90 Hz, and its communication with the controller is via I^2C serial interface. An on-chip temperature sensor is also included with a resolution of 0.1 °C and accuracy of ± 2 °C. The acquired data can be sent wirelessly to the user via Bluetooth with a low power and reprogrammable BM78 Bluetooth module (Microchip Tech. Inc, Chandler, AZ, USA). Wired USB bus is also available to display the data on any serial monitor of a computer for debugging purposes.

As shown in Figure 2b, the pair of metal parallel electrodes were fabricated on a standard copper clad FR4 board, where the electronic components and systems (Arduino Nano, capacitive sensor, and Bluetooth module) were soldered. Considering the practical minimum spatial resolution of the circuit board plotter, the two metal electrodes were initially designed with a width and separation of 254 µm, and a total length of 45 mm. Because of the tolerance of the PCB plotter, the actual width and gap electrodes were measured using an optical profilometer as shown in Figures 2d-e, whose details are given in Table 1. The copper layer thickness of the FR4 board determined the electrode thickness, which was 35 µm. With this configuration, the measured capacitance of the nude electrodes was 1.71 ± 0.01 pF. In addition, the designed printed circuit board includes a button for manual data acquisition initialization and a patterned ruler for quick localization of the imbibition liquid front on the paper strip.

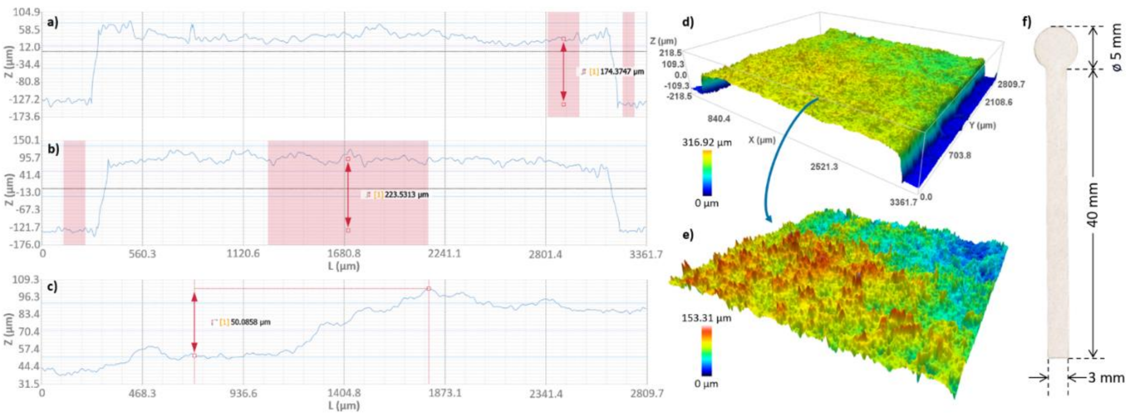

Figure 3. *Paper swelling. (a) Cross-section profile measured in the dry area; (b) Cross-section profile measured in the wet area; (c) Cross-section profile of the transition from dry to wet areas; (d) 3D profiler image of the paper, including the substrate; (e) Detailed 3D profiler image of the paper without the substrate; (f) Photograph of the paper strip with dimensions, consisting of a circular zone for liquid intake, followed by a rectangular zone for liquid imbibition*

The paper strip is attached to the sensing platform in horizontal position; therefore, the gravity effect is not considered in this work. Firstly, a strip of double-sided adhesive tape with dimensions of 10 mm width and 50 mm length is centred and aligned on the capacitive electrodes. This layer functions as a liquid barrier between the electrodes and the paper strip, ensuring that the paper strip remains fixed and flat. Subsequently, the paper strip is attached to the tape with the same centred and aligned position along the longitudinal axis (x-axis) of the electrodes pair (refer to Figure 2c). In order to ensure high test reproducibility, it is essential to precisely control the liquid volume and the water intake disposition, since prior research has proved that the initial contact between the liquid and the paper is a critical determinant of flow rate[3,39]. To achieve this objective and in line with the typical use of this kind of paper strip in analysis, a polymeric accessory has been designed and fabricated using 3D printing technology to secure the micropipette tip in a fixed position. Firstly, a controlled liquid volume is aspired by the micropipette and deposited in the tip. Then, the tip is detached from the micropipette body and brought into contact with the zone of the paper liquid intake. As we will show below, our tests demonstrate that the proposed setup ensures that the liquid flows reproducibly into the paper, driven by the capillary pressure.

Measurement procedure. The procedure for measuring capacitance as a function of time, $\Delta \boldsymbol{C}_{\boldsymbol{exp}}(\boldsymbol{t})$, is illustrated in the flow diagram presented in Figure S1 of the Supplementary Information file. Upon powering up the system, the Arduino Nano configures the capacitive sensor by selecting the desired channel (A or B), the sampling rate, continuous or single conversion mode, and the offset to adjust the measurement range. To minimize electric noise, a sampling rate of 16 Hz was selected to filter out the 50 and 60 Hz electric noise, continuous conversion, and an offset to measure capacitance ranging from 0 to 8 pF. Subsequently, upon pressing the start button, the controller verifies whether the final conversion flag is enabled to store the read capacitance value until the configured output time is reached. To improve the signal-to-noise ratio, a moving average filter of 5 consecutive samples is implemented in the Arduino sketch, providing valid capacitance readings every 100 ms. Following numerous tests, this configuration has provided stable and accurate capacitance measurements for this study. Finally, the data is transmitted via Bluetooth and USB to a smartphone and a computer, respectively. The description of the custom-developed smartphone application along with some screenshots are included in Figure S2.

Numerical analysis

In this study, a finite element method (FEM) was used to solve the numerical problem using the COMSOL Multiphysics environment. A dual simulation was carried out, where the capacitance ($\boldsymbol{C}$) of the electrodes under the paper strip was first calculated as a function of the length of the liquid front assuming a step function for the transition between dry paper and wet paper. To achieve this, the total paper length ($\boldsymbol{L}$) was divided into ten equal segments, and the electrical capacitance of the entire paper strip was calculated sequentially with the complete paper dry, then with the initial segment wet, and so on until all ten segments were completely wet. This provided the simulated capacitance as a function of the length of the liquid front, $\Delta C_{sim}(L_{lf})$. The AC/DC module was used for this numerical calculation, including the complete platform geometry and relevant electric parameters, which are listed in Table 1. The dimensions were measured with the profilometer (including thickness of the swelled paper, as shown in Figure 3); the paper permittivity (dry and wet) was determined with the described setup; and the rest of the parameters were taken from the well-known material properties (copper, FR4 that is glass-reinforced epoxy laminate material, and polypropylene). Paper dimensions were analysed, and Figure 3a-c shows a noticeable increase in paper thickness while wicking, measuring approximately 50 μm of swelling (an additional 27% from the initial dry paper thickness of 180 μm).

Table 1. Dimensions and electrical parameters of capacitance versus the length of the liquid front simulation for our measurement platform.

Structure (material)	Parameter	Value

Substrate (FR4)	Thickness	1.5 mm
	Relative permittivity	4.5
Electrodes (Cu)	Width*	200 µm
	Gap*	300 µm
	Thickness	35 µm
Double-sided adhesive tape (polypropylene)	Thickness*	75 µm
	Relative permittivity	2.4
Paper (Whatman G1)	Total length	40/45 mm
	Width	3/5 mm
	Thickness* (dry)	180 ± 2 µm
	Relative permittivity** (dry)	1.9 [40]
	Thickness* (wet)	230 ± 5 µm
	Relative permittivity** (wet)	18

* Measured with the profilometer

**Measured with the impedance analyser.

Once the correlation between the capacitance and the length of the liquid front was established by electrical simulation, the next step involved incorporating the time variable and liquid flow dynamics into the calculation. Therefore, the second step involved simulating the liquid flow, where the length of the liquid front, $L_{lf}(t)$, intake volume, and flow rate, $Q(t)$, were calculated as a function of time. In this simulation, the paper strip was initially considered filled with air with an initial water saturation of 0.01. The Brooks and Corey model for capillary pressure and relative permeabilities was used for the time-dependent simulation[41]. No water flow was allowed at the side boundaries of the paper strip. The boundary conditions for the bottom and top boundaries for Darcy's law were the atmospheric pressure for water phase at the bottom, and the hydrostatic atmospheric pressure minus the capillary pressure at the

top. For the phase transport, no flux was assumed for the air phase at the bottom boundary. At the top boundary, a mass flux for the air phase was defined, resulting from the pressure gradient given in the Darcy's model.
This numerical calculation employs the multiphase flow in porous media, which couples the Darcy's law and Phase Transport in Porous Media interfaces. The effect of evaporation was not considered, as explained below in the Experimental setup subsection. The Phase Transport in Porous Media interface follows separate equations for the volume fraction s_i of the wetting or nonwetting fluid i:

$$\frac{\partial}{\partial t}\left(\varepsilon_p \rho_i s_i\right) + \nabla \cdot \left(-\rho_i \kappa \frac{\kappa_{ri}}{\mu_i}(\nabla p_i)\right) = 0, \tag{1}$$

where ε_p is the porosity, κ is the permeability, κ_{ri} is the relative permeability (a function of saturation for a given fluid), μ_i is the dynamic viscosity of the fluid, p_i is the pressure, and ρ_i is the fluid density of phase i. As the sum of the volume fractions of the two phases is 1, we can calculate $s_1 = 1 - s_2$. For the wetting phase, the used equations are[41]:

$$p_c = p_{ec} s_1^{\frac{-1}{\lambda_p}} \tag{2}$$

$$\kappa_{r1} = s_1^{3+\frac{2}{\lambda_p}} \tag{3}$$

$$\kappa_{r2} = s_2^2\left(1 + s_1^{1+\frac{2}{\lambda_p}}\right) \tag{4}$$

$$p_{ec} = \frac{2\gamma \cos \cos \theta}{R_c} \tag{5}$$

where p_c is the capillary pressure, and p_{ec} is the entry capillary pressure[42]. Moreover, λ_p is the pore size distribution index, and γ is fluid surface tension. We consider 0º static contact angle as usual in studies with water[16], and the initial value of the volume fraction s_2 as 0.99. Additionally, we incorporated to this standard modelling the effects of observed porosity and pore size reduction, which are known to be significant factors in the swelling of porous media[10,11]. To this end, we included the following relationships to account for the parameter dependence on these magnitudes:

$$\boldsymbol{R_C = R_{c0}(1 - \alpha \cdot t)} \tag{6}$$

$$\boldsymbol{\varepsilon_p = \varepsilon_{p0}(1 - \alpha \cdot t)^2} \tag{7}$$

$$\boldsymbol{\kappa \propto \varepsilon_p R_c^2 = \kappa_0(1 - \alpha \cdot t)^4} \tag{8}$$

where parameters with subscript *0* refer to the initial values, and α is the pore size reduction coefficient (s^{-1}). We are assuming a functional dependence of permeability with the pore size as the capillary-model[43]. The parameters used in this second simulation step are listed in Table 2 for the two liquids employed in the experiments.

Table 2. Parameters for the liquid wicking simulations.

Parameter	**Value**	
	Purified water	**1 M NaCl aqueous solution**
Surface tension (γ)	0.0723 N/m	0.069 N/m [44]
Viscosity (μ)	10^{-3} Pa·s	$1.09 \cdot 10^{-3}$ Pa·s [45]
Density (ρ)	1000 Kg/m^3	927 Kg/m^3 *
Pore size reduction coeff. (α)	10^{-3} s^{-1}	
Pore distribution index (λ_p)	2	
Initial pore radius (R_{C0})	5.5 µm	
Initial porosity (ε_{p0})	0.66 [46]	
Initial permeability (κ_0)	$4.4 \cdot 10^{-13}$ m^2	
Air density	1 kg/m^3	

Air viscosity	$1.76 \cdot 10^{-5}$ Pa·s

*Measured at 21 °C.

To demonstrate the impact of including on the flow dynamics the pore size reduction resulting from paper swelling, Figure S3 shows the absorbed water mass for a range of α values from 0 to $2{\cdot}10^{-3}$ s^{-1}. As expected, a significant variation can be observed in the wicking dynamics with this coefficient, even at low intervals such as 20 s. As we demonstrate later, our best fitting with experimental data is given for α = 10^{-3} s^{-1}. This value is consistent with a similar coefficient of α = $0.954{\cdot}10^{-3}$ s^{-1} reported in a previous study[11].

Following the numerical simulation, a conclusive relationship between the experimental capacitive transients and the flow dynamics was established. As a result, the numerically calculated volume/mass intake and flow rate will be derived as a function of time from the experimental capacitance transient during the wicking process, as detailed in the Results section. The only free parameter is the initial paper permeability, κ_0, with the value presented in Table 2 being compatible and intermediate with those reported by the capillary-model (κ_0 = $2.5{\cdot}10^{-12}$ m^2)[43] and the manufacturer (κ_0 = $9.8{\cdot}10^{-14}$ m^2), and the value referred in recent studies[47]. Numerous empirical and theoretical models have reported varying values for this parameter[11,48]. However, a comprehensive discussion regarding this issue is outside the scope of this work.

Another crucial issue that needs to be considered is the impact of the inaccuracies in the values of the properties presented in Tables 1 and 2 on the calculation of the flow parameters (intake volume and flow rate). To examine the relative sensitivities of the flow monitoring parameters as a function of these properties, we conducted numerical calculations as described in the SI and outlined in Figure S4. By introducing separate relative variations of approximately ±10% for the initial porosity (ε_{p0}), wet paper thickness (th_w), and initial permeability (κ_0), we determined the corresponding variations in volume and flow rate over time. Through a comparison of the three curves associated with each property, it can be concluded that these relative variations are also reflected in the flow parameters for initial porosity and paper thickness. Therefore, relative sensitivities of 1 were obtained for ε_{p0} and th_w. On the other hand, the flow parameters exhibited a relatively low sensitivity to variations in the initial permeability, with a sensitivity of 0.4 for volume variation and 0.11 for flow rate variation. This calculation demonstrates that our procedure exhibits greater robustness against inaccuracies in the only free parameter considered in our simulations (i.e., the initial permeability) compared to the other studied properties.

Experimental setups

The measurements were conducted in our laboratory under controlled environmental conditions of 21 ± 1 °C temperature and 30 ± 10 % relative humidity. An estimation of the evaporation effect on the liquid wicking dynamics was calculated using these ambient conditions along with the flow parameters presented in Table 2 according to a previously reported model[24]. We obtained a correction of the wicking duration below 1% and 2% for time intervals of 40 and 90 s, respectively. As a result, the influence of liquid evaporation on our experiments can be neglected for wicking times below 60 s, and this effect was not considered in the numerical simulations.

Firstly, we measured the relative permittivity of dry, $\varepsilon_r(dry)$, and wet samples, $\varepsilon_r(wet)$, Whatman G1 paper samples. To perform this measurements, six circular-shaped paper samples with 6 cm diameter (three dry and three wet) were laser-cut and inserted between the type A electrodes of the 16451B test fixture, which was connected to the 4294A impedance analyzer. Our results showed $\varepsilon_r(dry)$ = 1.75 ± 0.15, which agrees with a recent experimental finding of 1.9 measured by microwave reflection[40] . Additionally, we determined $\varepsilon_r(wet)$ = 18 ± 2 for wet paper, and this value was used in the numerical calculation of the capacitance (see Table 1). The uncertainty in both cases was calculated as the standard deviation of the experimental dataset. Two preliminary validation experiments were conducted:

V1. Validation of the experimental capacitance measurements. For this purpose, we compared the capacitance values obtained with the developed sensing platform with those measured from the LCR meter used as reference system. To do this, three paper strips with a circular zone of 5 mm diameter for liquid intake, followed by a rectangular zone with dimensions of 40 mm length and 3 mm width for liquid imbibition, were laser-cut as shown in Figure 3f. After attaching these strips to the capacitive platform, they were imbibed with the liquid according to the procedure detailed above. During the validation, the LCR meter was connected to the platform electrodes so that the measurements were conducted under the same conditions. The capacitance measurements were taken by switching between both systems due to the capacitance input coupling of the reference system, which saturated the AD7746 sensor of the platform. The dependence with the temperature of the capacitive platform was also measured from 15 to 35 °C.

V2. Validation of the simulated capacitance. Using the video camera of the mentioned smartphone along with the rule patterned on the PCB (see Figure 2), we measured the capacitance increase as a function of the length of the liquid front (L_{lf}) of three paper strips. Numerical capacitances were also calculated as a function of L_{lf} by the electrical simulation, using the parameters presented in Table 1. The experimental capacitance registered by the developed measurement platform was then compared to the calculated numerical capacitances.

Next, a series of experimental tests were planned to evaluate the performance of the flow monitoring platform in various scenarios, including a reproducibility test, control flow with different paper strip geometries, flow retention with chemical valves, and an application of flow monitoring for accurate analytical determination.

T1. Reproducibility tests with purified water and a 1 M NaCl aqueous solution. For each liquid, five paper strips were used as described in V1. Uncertainty was calculated as the standard deviation of the dataset.

T2. Dependence of paper strip geometry on flow dynamics. Paper strips with exponentially varying width were prepared to modulate the filling dynamics[39]. In this case, the initial paper width was w_0 = 5 mm, and the total length L = 45 mm. The variable width was defined as $w(x) = w_0 e^{-x/l_0}$. Replicating the experiment previously proposed[39], with $w(x) = W_0$, and $l_0 = L/2$ and $L/3$, the flow dynamics of three strip patterns were analysed with the capacitive platform.

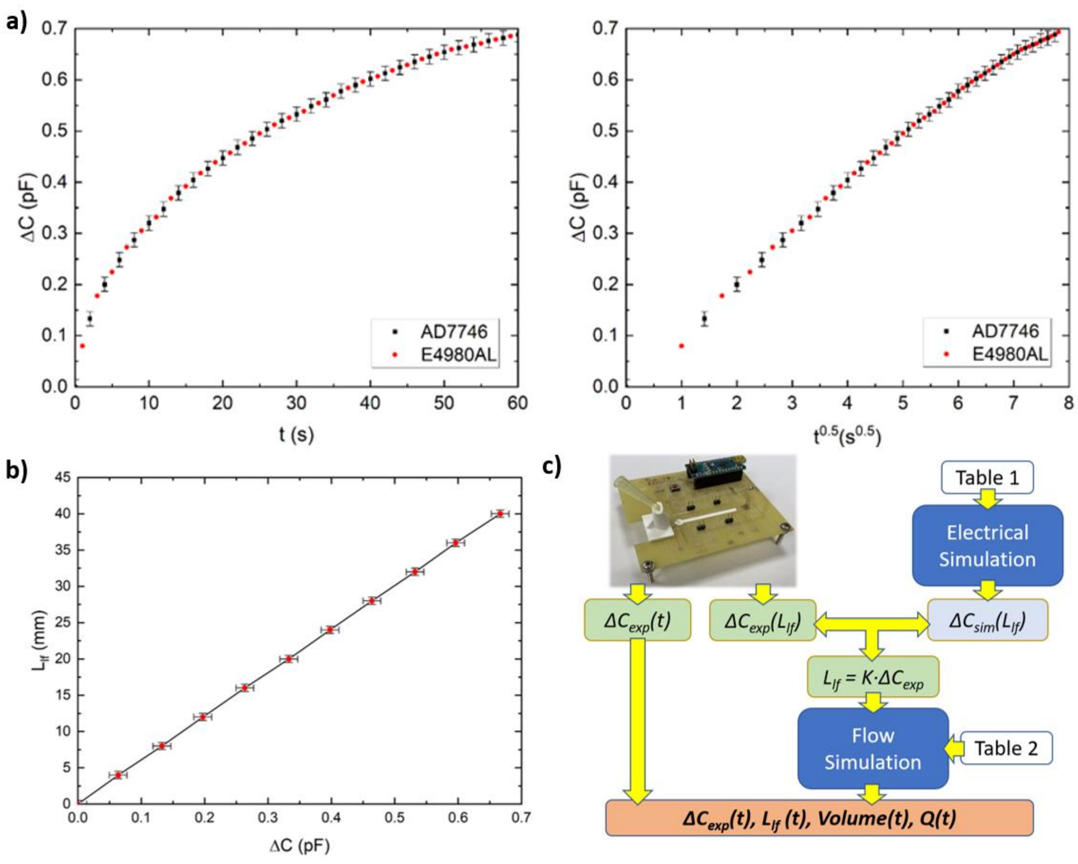

Figure 4. *(a). Validation test curves: comparison between proposed AD7746 capacitive sensor (black symbols) and the reference instrument E4980 (red symbols) versus time and square root of time. (b) Comparison of the experimental data (symbols) and numerical simulation (line), also showing the linear correlation between the length of the liquid front and the capacitance change. (c) Experimental/numerical procedure of flow monitoring.*

T3. Flow retention with chemical valves. A couple of simple experiments including chemical valves were carried out to evaluate the platform's ability to measure irregular flows. Wax, chitosan and sucrose were used as barriers in the imbibition filling with purified water, using the same paper strip shape of experiment V1.

T4. Flow time control for colorimetric determination. An experiment was conducted to assess the performance of the platform in colorimetric detection, where reaction time is an essential parameter to ensure accurate colour measurement. GJM-530 dye was covalently immobilized on Whatman grade 1 paper sheets[49]. These sheets were then cut using a punch into 0.5 cm diameter circles and stored under light-protected from light. Using double-sided tape, the circles were affixed to the end of the paper strip positioned over the flow controller. To initiate the reaction, 28 μL of 0.1 M phosphate buffer solution was added to the intake zone. The reaction was tested under a fixed pH value of 10, resulting in a color change of the dye to red.

Results and discussion

Experimental validation

V1. Validation of the experimental capacitance measurement. Excellent agreement between both capacitive registers can be observed in Figure 4a. A full-scale (8 pF) relative error of 0.25% was measured, resulting in an absolute capacitance error of ± 0.01 pF. This error becomes ± 0.014 pF when ΔC is calculated.

Moreover, the temperature sensor integrated into the capacitive detector was utilized to characterize the linear temperature coefficient, α_T, within the temperature range of 15 to 35 °C. An average value of α_T = 0.6 fF/K was obtained. This low thermal drift ensures the reliability of capacitance data under typical testing conditions.

V2. Validation of the numerical capacitance. Figure 4b compares the experimental and simulated capacitances, showing an excellent agreement with no free parameter in the numerical simulation (see Table 2). With this comparison, we consider that our capacitive platform can provide reliable data, and no further video recordings will be required in subsequent experiments. Moreover, a linear trend was obtained with the length of the liquid front, validating the step approximation for the liquid front as a suitable assumption. This linear fitting allows the determination of L_{lf} from the capacitive measurements through a simple proportionality constant. This fact will provide the link to calculate the absorbed mass/volume and flow rate, $Q(t)$, in the paper strip from the measurements of the proposed platform. The flow chart in Figure 4c details the procedure, which involves the following steps:

1. Experimental $\Delta C_{exp}(t)$ and $\Delta C_{exp}(L_{lf})$ are registered by our capacitive platform. The latter is performed only once for validation purposes.

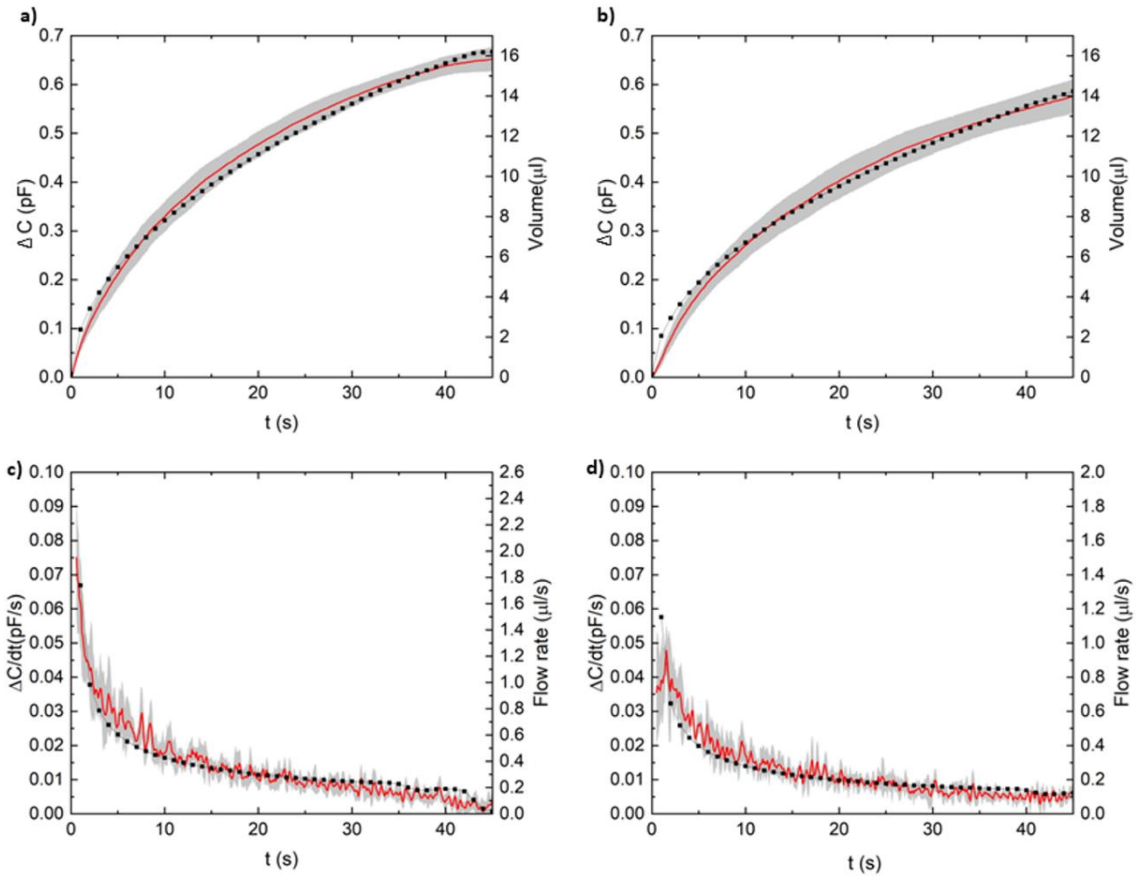

Figure 5. *Purified water (a, c) and 1 M NaCl solution (b, d) wicking dynamics (capacitance/volume variation and flow rate): experimental data (line) and numerical simulations (symbols). The grey area under the line represents the experimental standard deviation of dataset.*

2. The numerical calculation of capacitance increment with $\boldsymbol{L_{lf}}$ is performed, $\Delta C_{sim}(L_{lf})$, and it is fitted with $\Delta C_{exp}(L_{lf})$. The simulation includes the platform geometry and electrical parameters, which are checked with this fitting.

3. Using the mentioned linear relationship between the capacitance increment and the length of the liquid flow, $L_{lf} = K\Delta C_{exp}$, (where K is a proportionality constant), this capacitance is transformed into the experimental length of the liquid front as a function of time, $L_{lf}(t)$.

4. This magnitude is compared with the COMSOL calculation of the flow dynamics, where magnitudes such as length of liquid front, $L_{lf}(t)$, absorbed mass/volume, and flow rate, $Q(t)$, are numerically calculated.

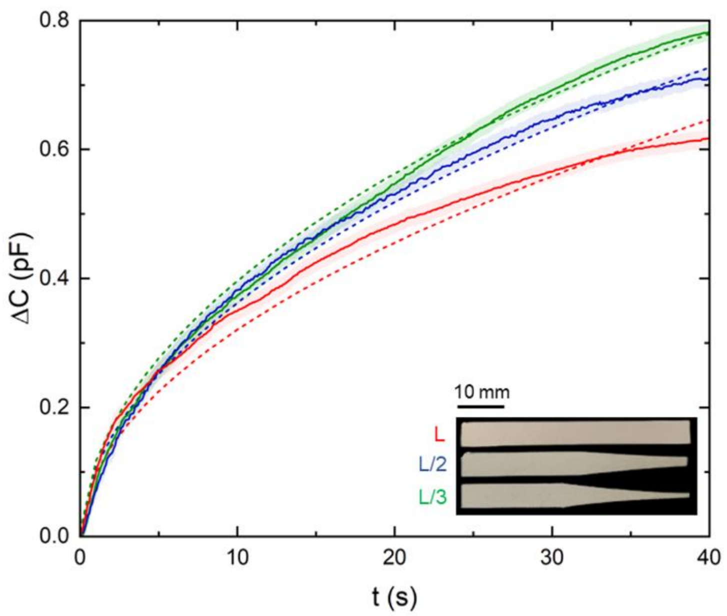

***Figure 6**. Geometrically flow control for L, L/2 and L/3 paper strips: experimental data and error (lines and coloured area) and numerical simulation (dashed lines).*

5. From the fitting between the experimental and numerical lengths of the liquid fronts, the volume and flow rate are also obtained as a function of time, displaying such flow parameters as results on the smartphone. As mentioned above, only the permeability value is a fitting parameter in this numerical calculation. The rest of the geometry, electrical, and flow parameters were measured or provided by manufacturers and previous literature.

Monitoring system performance

T1. Reproducibility tests. To demonstrate the reproducibility of the microfluidic platform, five replications of experiments were performed with two different aqueous solutions under the aforementioned conditions. The standard deviation of the measurements is shown in Figure 5 as a grey area under the red line (experimental tests). The maximum uncertainty obtained for purified water was 0.024 pF (0.5 µl) and 0.00036 pF/s (9 nl/s) in the case of flow rate. The error for NaCl 1M was slightly higher in ΔC, 0.03 pF (0.7 µl), and 0.0003 pF/s (7 nl/s) for flow rate determination. As can be seen, the results obtained by simulation with COMSOL (symbols) show good agreement with the experimental results.

T2. Geometric flow control. To investigate the impact of paper geometry on liquid flow, Elizalde et al[39], designed paper strips of lengths *L*, *L*/2 and *L*/3, as described in their work. The *L*/4 structure was excluded from the study as the tip of the paper in the narrowest end was located between the platform electrodes, rendering reliable testing impossible. Both experimental data and COMSOL simulations indicate similar tendencies and behaviour as those presented in the mentioned study[39], as shown in

Figure 6. Notably, the strip with the smallest exponential width geometry exhibited a shorter total filling time of the paper.

T3. Chemical valves. With the purpose of investigating variations of flow conditions along paper strips, several custom-made chemical valves were tested. First, 5 µl of 25 mg/ml chitosan in purified water were deposited onto a paper strip, allowing it to dry for 40 minutes prior to testing. As shown in Figure 7a, a slight delay in flow rate was observed from seconds five to seven due to the physical barrier created by the chitosan. The second valve tested was created by using a common red crayon, which diffused the wax across the strip creating a barrier after being heated at 100 ºC for five minutes. As shown in Figure 7b, this barrier completely halted the flow of the liquid solution until it was heated again at 80 ºC for two minutes, after which the flow rate was increased.

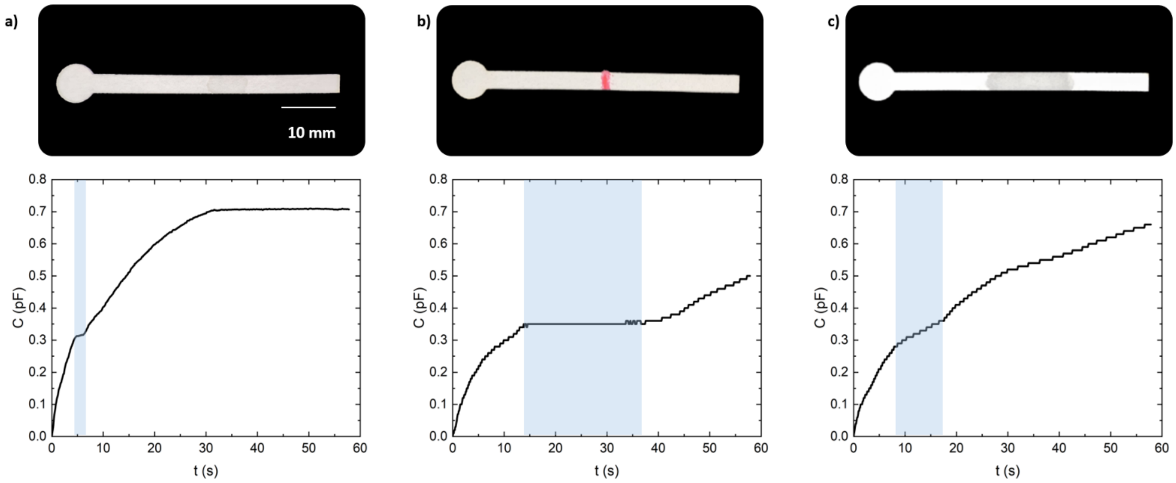

***Figure 7.** Experimental capacitive transients using different chemical valves. Top pictures show the paper strip with the deposited chemicals: a) Chitosan, b) Wax barrier (heated after 23 seconds), and c) Sucrose. Experimental errors have not been represented for the sake of clarity.*

Finally, we investigated the use of a sucrose solution as a valve to slow-down the flow rate in our microfluidic platform. In order to construct an efficient barrier, three layers of 4 µl of saturated sucrose in purified water were deposited, allowing each layer to dry for 20 minutes before depositing the next, and allowing a complete day for the last deposition to dry. A decrease in the flow rate of the liquid between 9 to 17 seconds can be observed in Figure 7c. Therefore, our capacitive measurement system for paper-strips has successfully demonstrated to accurately monitor both the forward movement and flow rate of liquid solutions, providing information on the position of the liquid front of various reagents that may be utilized in more complex chemical reactions. Furthermore, it would be feasible to monitor the time required for a solution to cross over a previously placed reagent, to ensure the complete reaction before measuring the target information[5].

T4. Flow time control for colorimetric determination. This test demonstrated the capability of the proposed platform for taking accurate analytical measurements through flow monitoring. When the phosphate buffer solution was placed in the paper strip's intake area, several facts can be pointed out according to Figure 8. As can be seen, the real-time monitoring of capacitance exhibited a change in slope upon the solution's arrival at the detection area (t_A). Subsequently, at t_B, the detection area became fully saturated, resulting in a constant capacitive response. At this moment, a timer was set for 60 s to ensure reaction stabilization before colour detection at t_C. In this case, a 60-s stabilization period proved to be an optimal time to yield a stable response[49].

Discussion

We have presented a capacitive sensing platform for flow monitoring in capillary-driven microfluidic devices, specifically demonstrated for μPADs. This proposed system is characterised for its compactness and reusability, utilizing off-the-shelf electronics and fabricated on a printed circuit board. In contrast to alternative solutions, no external or bulky equipment or sensors are required. Furthermore, by incorporating commercially available batteries, the system can operate independently of a computer connection. Configuration of the system and retrieval of data are wirelessly performed using a smartphone, enabling real-time and on-site measurement of liquid flow in paper strips. The smartphone application facilitates system operation by non-trained users through a user-friendly and intuitive interface that guides users through the microfluidic tests.

To acquire comprehensive information about the flow process, the capacitive measurements need to be initially combined with numerical simulation, including the physical and chemical parameters that characterize the liquid and the paper strip. However, once the numerical constants establishing the relationship between capacitance and flow parameters (intake liquid volume and flow rate) are determined, the platform can be readily utilized for subsequent tests without the need for further simulations, as long as the liquid and paper strip geometry remain unchanged.

Integrated electrodes for detection or liquid manipulation have already been employed in microfluidic devices for electrokinetic flow, electrowetting, or conductivity monitoring[50], exhibiting excellent performance for local actuation or sensing. Moreover, within our developed versatile flow monitoring platform, the paper substrate could be substituted with fabric, as the capacitive sensing transduction principle will respond to changes in the dielectric constant of a wet fabric. Additionally, by adding more digital capacitance detector chips, the system can be scaled, enabling flow monitoring not only in basic paper strips but also in different paper-based patterns with multiple liquid paths, thereby expanding the capabilities of the system. Therefore, drawing inspiration from our previous expertise in planar printed capacitive sensors and the system presented by Temiz et al.[26], our work introduces several remarkable innovations: *i)* incorporation of a high-resolution digital capacitive detector with a built-in temperature sensor, *ii)* application to paper strips, validation of measurements and determination of flow parameters through a physical-based numerical simulator, and easy scalability for multiple paper paths and applicability to fabric substrates.

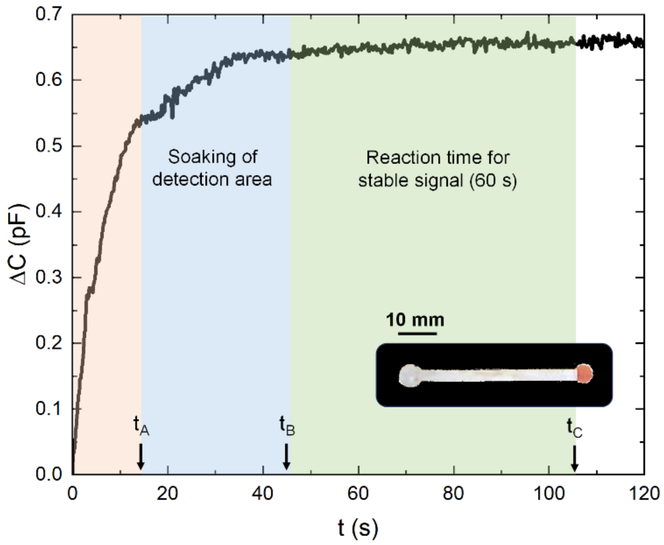

Figure 8. *Experimental capacitance transient of the T4 test, monitoring the imbibition of the paper strip (orange zone), the wetting of the detection area (blue zone), and the duration of 60 s for the complete colorimetric reaction and accurate colour measurement. The limit times between these periods are denoted as* t_A, t_B, *and* t_C. *The inset shows the paper strip with the coloured dye.*

Conclusions

This work presents a wireless and portable electronic platform designed to monitor the flow and flow rate of liquids in paper-based microfluidic devices driven by capillary force. The full hardware and software tools have been described, and operational specifications have been extracted. Relevant features of this measurement system include its affordability, reusability, and its potential for extension to textile substrates as well. Furthermore, the experimental setup demonstrated notable repeatability and good performance for different paper geometries and chemical valves. Not only qualitative but also quantitative flow and flow rate measurements can be obtained together with numerical simulations of the electrical and flow dynamic phenomena. To achieve this, knowledge of the dielectric constant of the wet paper and flow parameters of the paper and liquid is required, which is the main limitation of this study. Nonetheless, we consider that this information, which is easily accessible, is required to obtain such quantitative information. This fact provides the possibility to deepen in the study of the flow dynamics on paper, an issue still opened to further study and modelling. On the other hand, smartphone have been demonstrated once again as essential and versatile widespread devices capable of visualizing and sharing results, serving as the user-interface for the developed platform.

Acknowledgements

This work was funded by Spanish MCIN/AEI/10.13039/501100011033/ (Projects PID2019-103938RB-I00, ECQ2018-004937-P and grant IJC2020-043307-I) and Junta de Andalucía (Projects B-FQM-243-UGR18, P18-RT-2961). The projects and the grant were partially supported by European Regional Development Funds (ERDF) and by European Union NextGenerationEU/PRTR.

References

1 R. Lucas, *Kolloid Zeitschrift*, 1918, **23**, 15–22.
2 E. W. Washburn, *Phys Rev*, 1921, **17**, 273–283.
3 A. Böhm, F. Carstens, C. Trieb, S. Schabel and M. Biesalski, *Microfluid Nanofluidics*, 2014, **16**, 789–799.
4 N. Walji and B. D. MacDonald, *Micromachines (Basel)*, 2016, **7**, 73.
5 E. Fu and C. Downs, *Lab Chip*, 2017, **17**, 614–628.
6 Y. Yang, E. Noviana, M. P. Nguyen, B. J. Geiss, D. S. Dandy and C. S. Henry, *Anal Chem*, 2017, **89**, 71–91.
7 H. Darcy, *The Public Fountains of the City of Dijon*, Paris, 1856, vol. 647.
8 M. Hamdaoui, F. Fayala and S. Ben Nasrallah, *J Appl Polym Sci*, 2007, **104**, 3050–3056.
9 N. Fries, K. Odic, M. Conrath and M. Dreyer, *J Colloid Interface Sci*, 2008, **321**, 118–129.
10 D. Schuchardt and J. Berg, *Wood and Fiber Science*, 1991, **23**, 342–357.
11 R. Masoodi and K. M. Pillai, *AIChE Journal*, 2010, **56**, 2257–2267.
12 S. Chang and W. Kim, *J Fluid Mech*, 2020, **892**, A39.
13 L. A. Richards, *Physics (College Park Md)*, 1931, **1**, 318.
14 R. Masoodi, H. Tan and K. M. Pillai, *AIChE Journal*, 2011, **57**, 1132–1143.
15 D. Rath, N. Sathishkumar and B. J. Toley, *Langmuir*, 2018, **34**, 8758–8766.
16 S. Patari and P. S. Mahapatra, *ACS Omega*, 2020, **5**, 22931–22939.
17 S. Modha, C. Castro and H. Tsutsui, *Biosens Bioelectron*, 2021, **178**, 113026.
18 L. Gervais, N. De Rooij and E. Delamarche, *Advanced Materials*, 2011, **23**, H151.
19 G. G. Morbioli, T. Mazzu-Nascimento, A. M. Stockton and E. Carrilho, *Anal Chim Acta*, 2017, **970**, 1–22.
20 H. Lim, A. T. Jafry and J. Lee, *Molecules*, 2019, **24**, 1–32.
21 E. Noviana, T. Ozer, C. S. Carrell, J. S. Link, C. McMahon, I. Jang and C. S. Henry, *Chem Rev*, 2021, **121**, 11835–11885.
22 Anushka, A. Bandopadhyay and P. K. Das, *European Physical Journal: Special Topics*, 2022, **123**, 1–35.

23 R. J. Roberts, T. J. Senden, M. A. Knackstedt and M. B. Lyne, *Journal of pulp and paper science*, 2003, **29**, 123–131.
24 C. K. Camplisson, K. M. Schilling, W. L. Pedrotti, H. A. Stone and A. W. Martinez, *Lab Chip*, 2015, **15**, 4461–4466.
25 M. N. Islam, J. W. Yost and Z. R. Gagnon, *Analyst*, 2022, **147**, 587–596.
26 Y. Temiz and E. Delamarche, *Sci Rep*, 2018, **8**, 1–11.
27 C. Delaney, P. McCluskey, S. Coleman, J. Whyte, N. Kent and D. Diamond, *Lab Chip*, 2017, **17**, 2013–2021.
28 N. Noeth, S. S. Keller and A. Boisen, *Sensors*, 2014, **14**, 229–244.
29 A. Alfadhel, B. Li, A. Zaher, O. Yassine and J. Kosel, *Lab Chip*, 2014, **14**, 4362–4369.
30 L. Zhang, X. Yu, S. You, H. Liu, C. Zhang, B. Cai, L. Xiao, W. Liu, S. Guo and X. Zhao, *Appl Phys Lett*, 2015, **107**, 242901.
31 Z. Zhang, J. Pan, Y. Tang, Y. Xu, L. Zhang, Y. Gong and L. Tong, *Lab Chip*, 2020, **20**, 2572–2579.
32 M. H. Zarifi, H. Sadabadi, S. H. Hejazi, M. Daneshmand and A. Sanati-Nezhad, *Sci Rep*, 2018, **8**, 1–10.
33 E. Skotadis, E. Aslanidis, G. Kokkoris, E. A. Vargkas Kousoulas, A. Tserepi and D. Tsoukalas, *Sens Actuators A Phys*, 2022, **344**, 113765.
34 J. Collins and A. P. Lee, *Lab Chip*, 2004, **4**, 7–10.
35 N. Arjmandi, C. Liu, W. Van Roy, L. Lagae and G. Borghs, *Microfluid Nanofluidics*, 2012, **12**, 17–23.
36 J. Wu and J. Ye, *Lab Chip*, 2005, **5**, 1344–1347.
37 C. Bathany, J. R. Han, K. Abi-Samra, S. Takayama and Y. K. Cho, *Biosens Bioelectron*, 2015, **70**, 115–121.
38 M. N. Islam, S. M. Doria, X. Fu and Z. R. Gagnon, *Sensors*, 2022, **22**, 1489.
39 E. Elizalde, R. Urteaga and C. L. A. Berli, *Lab Chip*, 2015, **15**, 2173–2180.
40 A. R. Eldamak and E. C. Fear, *Sensors*, 2018, **18**, 4088.
41 R. H. Brooks and A. T. Corey, *Journal of the Irrigation and Drainage Division*, 1966, **92**, 61–90.
42 R. Masoodi and K. M. Pillai, *J Porous Media*, 2012, **15**, 775–783.
43 F. L. Dullien, *Fluid Transport and Pore Structure*, New York, 1992.
44 B. R. Bzdek, L. Collard, J. E. Sprittles, A. J. Hudson and J. P. Reid, *Journal of Chemical Physics*, 2016, **145**, 054502.
45 J. Kestin, I. R. Shankland and R. Paul, *Int J Thermophys*, 1981, **2**, 301–314.
46 V. P. Mai, C. H. Ku and R. J. Yang, *Microfluid Nanofluidics*, 2019, **23**, 1–10.
47 N. Koursari, O. Arjmandi-Tash, A. Trybala and V. M. Starov, *Microgravity Sci Technol*, 2019, **31**, 589–601.
48 R. Liu, Y. Jiang, B. Li and L. Yu, *Microfluid Nanofluidics*, 2016, **20**, 1–13.
49 M.J. Arroyo, I. Orbe-Payá, M. Ortega, J. Vilar, D. Gallego, G.J. Mohr, L.F. Capitán-Vallvey, and M.M. Erenas, Sensors and Actuators B, 2022, **359**, 131549
50 N. Fukuna, T. Sonsa-ard, N. Chantipmanee, P.C. Hauser, P. Wilairant, and D. Nacapricha, Sensors and Actuators B, 2020, **339**, 129838

3.3.3.1 *Publication 4. Supplementary Information*

Capacitive platform for real-time wireless monitoring of liquid wicking in a paper strip

Isidoro Ruiz-García[a,b,d], Pablo Escobedo[a,b,d], Celia E. Ramos-Lorente[b,c], Miguel M. Erenas[b,c], Luis F. Capitán-Vallvey[b,c], Miguel A. Carvajal[a,b,d], Alberto J. Palma[a,b,d,*], Nuria López-Ruiz[a,b,d]

[a] *Electronic and Chemical Sensing Solutions (ECsens), CITIC-UGR, Department of Electronics and Computer Technology, University of Granada (UGR), 18071 Granada, Spain.*
[b] *Unit of Excellence in Chemistry Applied to Biomedicine and the Environment of the University of Granada, Granada, Spain.*
[c] *Electronic and Chemical Sensing Solutions (ECsens), Department of Analytical Chemistry, University of Granada (UGR), 18071 Granada, Spain.*
[d] *Sport and Health University Research Institute (iMUDS), University of Granada (UGR), 18071 Granada, Spain*

Measurement procedure and smartphone application

The procedure for measuring capacitance as a function of time, ∆Cexpt, is illustrated in the flow diagram presented in Figure S1.

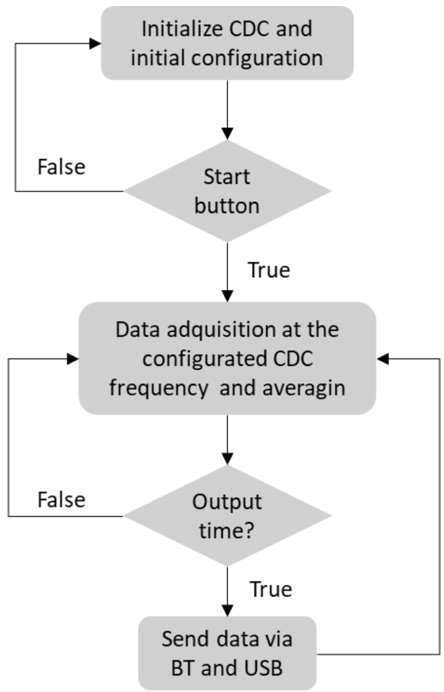

Figure S1. Flow chart of the measurement procedure of the capacitance

A customized smartphone application was developed to enable easy connection and data reception from the capacitive sensing platform, as illustrated in Figure S2. Upon the first opening of the application, the user must conduct the pairing process with the Bluetooth device, which can be done using the 'Discover' button to select the sensing platform from a list of available devices. Once paired, the application automatically saves the device's MAC address in a plain text file on the internal memory of the smartphone. In this way, whenever the user opens the application, they can simply click on the 'Connect' button to automatically bond with the sensing platform without requiring another pairing process since the keys have been already established. Once connected, the user only needs to press the 'Start' button on the screen to activate the reception mode. After this, when the user clicks on the physical start button on the sensing platform (refer to Figure 2c), the application begins to receive and graph the data in real-time via the Bluetooth connection. After the completion of the data acquisition process, the user can navigate through the graphed data and select specific data points by using pinch and zoom gestures. Additionally, the application features an action bar, as shown in Figure S2, with several options that allow the user to save the acquired data (both numeric data and graph) on the smartphone's internal memory, clear the chart for new data acquisition, or share the results through email and various cloud or messaging services. A video demonstration of the smartphone application working in connection with the capacitive sensing platform is available in the Supplementary Movie.

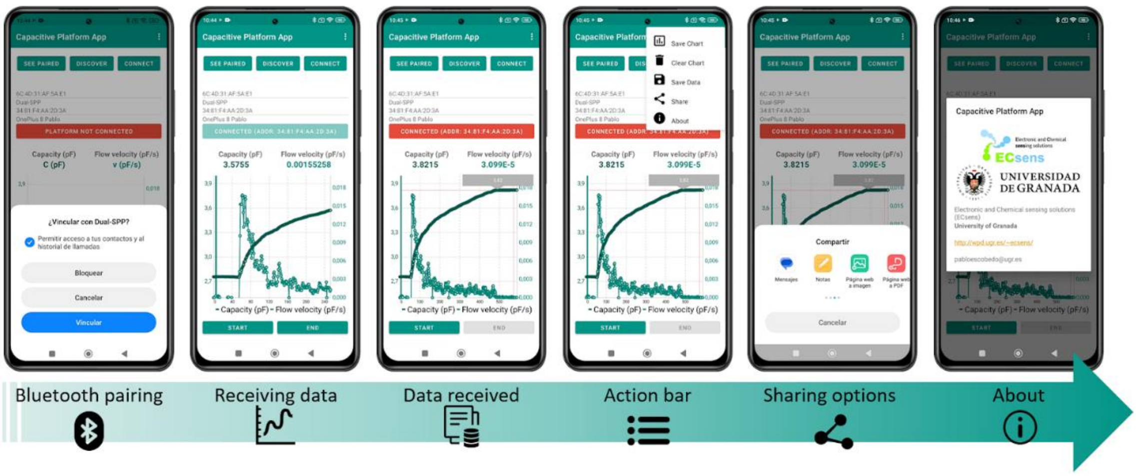

Figure S2. Smartphone app screenshots illustrating some of the key steps of the connection with the capacitive sensing platform, including pairing, data reception, and available options.

Numerical analysis

To demonstrate the impact of including the pore size reduction, α, resulting from paper swelling on the flow dynamics, Figure S3 shows the absorbed water mass for a range of α values from 0 to $2\cdot10^{-3}$ s^{-1}.

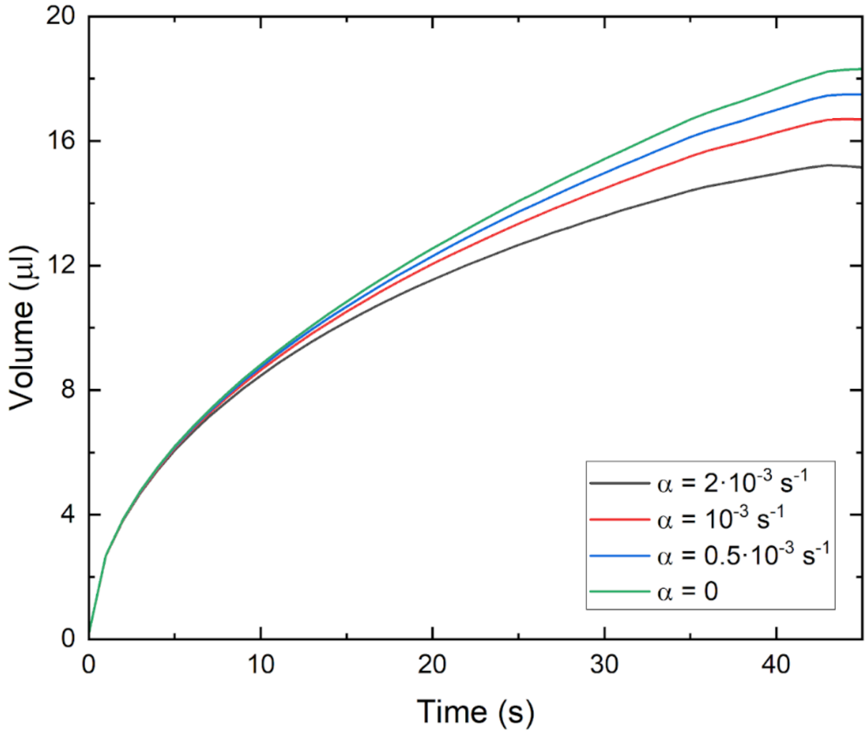

Figure S3. Simulated water intake vs time for various pore size reduction coefficients, α. Geometry of the paper strip is, as validation and reproducibility tests, described in the experimental setups.

4 Conclusions and future work

In this section, a comprehensive overview of the primary findings attained through the conducted research is provided. The focal point of this investigation has been the development and implementation of microcontrolled sensing platforms designed for diverse health-oriented applications.

In particular, the presented thesis has explored three distinct fields: the investigation of semiconductors devices as dosimetric sensors in radiotherapy, inertial sensor technology applied to sports monitoring, and microfluidic platforms for flow monitoring in cellulosic substrates. The main conclusions pertaining to each field are as follows:

Dosimetry

- A system was developed for the study of diodes and photodiodes as dosimetric sensors. The system is based on the PIC18F46K42 microcontroller, leveraging its features along with the designed signal conditioning to achieve a theoretical sensitivity of 80 pA. Beyond measuring the current induced by radiation, the system enables real-time temperature monitoring of the sensor to correct the drift of the dose rate calculated affected by thermal dependency. Additionally, with the incorporation of a multiplexer into the reading unit, the system can concurrently monitor up 4 sensors. The configuration of the system enables real time measurement of the devices' radiation response at a sample rate of 1 Hz. Although this sampling rate could seem slow, the reader unit performs a much higher sampling, complemented by digital filtering and analog filters integrated onto the electronics board.
- An in-depth study of the feasibility of using different commercial optical sensors as dosimeters for gamma beams was conducted using the previously developed system. It was concluded that the BPW34S photodiode is the best candidate among those tested for this purpose. This device exhibited an average sensitivity of 13.9 ± 0.5 nC/cGy with a bias voltage of -10V. Additionally, the sensitivity was reduced by less than 2% after 21.4 Gy. Details of this study are presented in the first publication of the compendium.
- Further, the thermal dependency of the same device was studied, and a method to correct it was implemented. To achieve this, the forward voltage, directly related to the temperature of the device, was monitored, and the dark current, which is exponentially affected by temperature, was corrected. As a result of applying this rectification, the thermal dependency was reduced from 1.5% to 0.2%. The results of this study are collected in the second publication of the compendium.
- To conclude the study of the BPW34S photodiode and its characterization as a dosimeter, its dependence on the angle of radiation incidence was examined. A

dependence of over 35% was found, which was corrected by implementing a 3D sensor composed of six photodiodes. This cube-shaped sensor reduced the dependence on the angle to 10.6%.

- Continuing the study of dosimetric sensors, RADFETs from Varadis were tested for their use as proton beam sensors. Specifically, the VT06 model was examined under proton beams of various energies (1, 2, 3, 151.23, and 230 MeV). As a result, it was concluded that this device is suitable for use for this purpose, exhibiting a linear increase in threshold voltage with dose for all studied energies.
- Finally in the study of dosimetric sensors, four models of commercial diodes (1N4007, UF4007, BY203, and GP02-40) with different breakdown voltages were tested as sensors for high dose rate gamma rays (365.17 Gy/min). Their sensitivity and degradation were studied, as well as the temperature and its potential dependence on the measured dose. All of them exhibited adequate sensitivity for use as dosimeters, with a degradation of sensitivity not exceeding 1.5% for a cumulative dose of 6.08 kGy. An in-depth study should be performed to apply a correction in the measured dose due to the increase in temperature during irradiations.

Sports monitoring

- A general-purpose inertial measurement system was developed and implemented for sports monitoring. This system utilizes a three-axis accelerometer, a three-axis gyroscope, and a three-axis magnetometer to estimate the position of the object under study. The ATSAMD21G18 microprocessor, in conjunction with the MPU-9250 sensor, has been employed for this purpose. The processing power of the ARM architecture processor enables real-time data processing and transmission at a rate of up to 200 Hz. The inclusion of a battery, along with the required electronics for its charging, make the system a very powerful portable tool with autonomy exceeding 10 hours. The third publication of the compendium shows the system development and its main results.
- The developed inertial measurement platform in was utilized for performance analysis in alpine skiing and for the development of an algorithm for detecting height and flight time of vertical jumps satisfactorily. In its application for alpine skiing, excellent agreement of inertial angles with a 3D camera system was obtained, with Pearson coefficients above 0.92. Additionally, in its use for the development of the vertical jump algorithm, minimal errors were observed, with just 0.35% for flight time and -1.84% for height measurement. In the future it is expected to be able to use the developed inertial measurement unit to detect different skiing techniques by applying artificial intelligence. It should be noted that after the publication of these results, the inertial development has continued to be improved in order to include it in a commercial product in collaboration with a company in the sector. Work continues along these lines in order to bring this

development to the market, obtaining a satisfactory transfer of results to the end user.

Microfluidics

- A capacitive platform based on the ATmega328 (Arduino Nano) was developed to monitor the flow and flow rate of liquids in paper-based microfluidic devices driven by capillary force. The experimental setup demonstrated notable repeatability and good performance for different paper geometries and chemical valves, as shown in the fourth publication of the compendium.
- Finally, the mentioned capacitive platform has been enhanced. Actuators have been added to control the flow in addition to monitoring it, and the capacitive measuring electrodes have been modified to increase the sensitivity by over 3 times. Due to these modifications, the latest tests have shown the ability to differentiate liquids using the platform. Therefore, the next steps will be focused on the detection of different dissolutions.

Overall, the conclusions drawn from each field reflect significant advancements and insights in each of the three key areas explored in this thesis, paving the way for future advancements, innovations and applications in the realm of health-related technologies.

5 Scientific contributions

Journals papers

Ruiz-García, I.; Navarro-Marchal, I.; Ocaña-Wilhemi, J.; Palma, A.J.; Gómez-López P.J.; Carvajal, M.A., *Development and Evaluation of a Low-Drift Inertial Sensor-Based System for Analysis of Alpine Skiing Performance*, Sensors 2021, 21, 2480, https://doi.org/10.3390/s21072480 (I.F. JCR: 3.847, Q2).

Ruiz-García, I.; Román-Raya, J.; Jesus Banqueri; Palma, A.J.; Guirado, D; Carvajal, M.A., *Commercial photodiodes and phototransistors as dosimeters of photon beams for radiotherapy*, Med. Phys., 48 (2021), pp. 5440-5447 https://doi.org/10.1002/mp.14921, (I.F. JCR: 3.8, Q1)

Ruiz-García, I.; Román-Raya, J.; Escobedo, P.; Andjelkovic, M.; Guirado, D; Palma, A.J.; Carvajal, M.A., T*hermal drift reduction in photodiode dosimeters with switching bias,* Measurement 2022, Volume 199, 111538, https://doi.org/10.1016/j.measurement.2022.111538 (I.F. JCR: 5.131, Q1)

Ruiz-García, I.; Escobedo, P.; Ramos-Lorente, C.E.; Erenas, M.M.; Capitan-Vallvey, L.F.; Carvajal, M.A.; Palma, A.J.; López-Ruiz, N., *Capacitive platform for real-time wireless monitoring of liquid wicking in a paper strip*. Lab on a Chip 2023. https://doi.org/10.1039/D3LC00368J (I.F. JCR: 6.1, Q1).

Román-Raya, J.; **Ruiz-García, I.**; Escobedo, P.; Palma, A.J.; Guirado, D.; Carvajal, M.A., *Light-Dependent Resistors as Dosimetric Sensors in Radiotherapy*, Sensors 2020, 20(6), 1568, https://doi.org/10.3390/s20061568 (I.F. JCR: 3.847, Q2).

Moreno-Pérez, J.A.; **Ruiz-García, I.**; Martín-Holgado, P.; Romero-Maestre, A.; Anguiano, M.; Vila, R.; Carvajal, M.A. *General Purpose Transistor Characterized as Dosimetry Sensor of Proton Beams*. Sensors (Basel, Switzerland) 2023, 23, 3771. https://doi.org/10.1039/D3LC00368J (I.F. JCR: 3.9, Q2).

Moreno-Pérez, J.A.; **Ruiz-García, I**.; Navarro-Marchal, I.; López-Ruiz, N.; Gómez-López, P.J.; Palma, A.J.; Carvajal, M.A. *System Based on an Inertial Measurement Unit for Accurate Flight Time Determination in Vertical Jumps*. Sensors (Basel, Switzerland) 2023, 23, 6022. https://doi.org/10.3390/s23136022 (I.F. JCR: 3.9, Q2).

Soares, S.; Ramos-Lorente, C.E.; **Ruiz-García, I**.; Rocha, F.R.P.; Erenas, M.M.; Orbe-Payá, I.D.; López-Ruiz, N.; Capitán-Vallvey, L.F. *A Cost-Effective Microfluidic Device for Determination of Biodiesel Content in Diesel Blends*. Sensors and actuators. B, Chemical 2023, 390, 134033. https://doi.org/10.1016/j.snb.2023.134033 (I.F. JCR: 8.4, Q1).

Arroyo, M.J., Escobedo, P., **Ruiz-García, I**. et al. POC device for rapid oral pH determination based on a smartphone platform. Microchim Acta 191, 134 (2024). https://doi.org/10.1007/s00604-024-06227-1 (I.F. JCR: 5.7, Q1).

Martín-Sierra, C.; Chavez, M.T.; Escobedo, P.; García-Cabrera, V.; López-Delgado, F.J.; Guardia-Monteagudo, J.J.; **Ruiz-García, I.**; Erenas, M.M.; Sanchez-Martin, R.M.; Capitán-Vallvey, L.F. et al. *SARS-CoV-2 Viral RNA Detection using the Novel CoVradar Device Associated with the CoVreader Smartphone App*. Biosensors & bioelectronics 2023, 230, 115268. https://doi.org/10.1016/j.bios.2023.115268 (I.F. JCR: 12.6, Q1).

International conferences

Isidoro Ruiz-García, Juan Román-Raya, Marko S. Andjelković, Damián Guirado, Alberto J. Palma, Miguel A. Carvajal, *Compensation of the temperature effect of the dark current in photodiodes dosimeters,* International Conference on Radiation in Various Fields of Research, Montenegro, June 2022.

Miguel Ángel Carvajal Rodríguez, Juan Antonio Moreno Pérez, **Isidoro Ruiz García**, Jaime Estela, María Sofía Martínez García, Damián Guirado Llorente, Alberto José Martínez García, *Multi-sensor MOSFET dosimeter for radiation measurements in Precursor CubeSat*, International Conference on Radiation in Various Fields of Research, Montenegro, June 2022.

Juan A. Moreno-Pérez**, Isidoro Ruiz-García**, Pedro Martín-Holgado, Yolanda Morilla, Alberto José Palma, Miguel Ángel Carvajal, *Commercial MOSFET characterization for proton dosimetry*, International Conference on Radiation in Various Fields of Research, Montenegro, June 2022.

Isidoro Ruiz-García, Juan A. Moreno-Pérez, Pedro Martín-Holgado, Amor Romero Maestre, Alberto José Palma, Miguel Ángel Carvajal, *PIN photodiodes as high dose dosimeters for proton beams,* International Conference on Radiation in Various Fields of Research, Montenegro, June 2022.

Isidoro Ruiz-García, Ismael Navarro-Marchal, Juan A. Moreno-Pérez, P. Lorenzo Uhrich, Alberto J. Palma, Pablo J. Gómez-López, Miguel A. Carvajal, *Smart Alpine Skis*, The 27th Annual Congress of the European College of Sport Science, Spain, September 2022.

Juan A. Moreno-Pérez, **Isidoro Ruiz-García**, Ismael Navarro-Marchal, Alberto J. Palma, Pablo J. Gómez-López, Miguel A. Carvajal, *Monitoring of jumps with an AD-HOC Inertial System,* The 27th Annual Congress of the European College of Sport Science, Spain, September 2022.

Juan Alejandro De La Torre, **Isidoro Ruiz-García**, Damián Guirado, Miguel A. Carvajal, Marta Anguiano Millan, Antonio M. Lallena Rojo; *Study of the angular dependence of a photodiode-based dosimeter using Monte Carlo simulation*, 11th International Conference on Radiation, Natural Sciences, Medicine, Engineering, Technology and Ecology., Montenegro, June 2023.

Isidoro Ruiz García, Pablo Escobedo Araque, Miguel Ángel Carvajal Rodríguez, Alberto José Palma Lopez; *Temperature effect on the sensitivity of PIN diodes used as gamma*

dosimeters; 11th International Conference on Radiation, Natural Sciences, Medicine, Engineering, Technology and Ecology., Montenegro, June 2023.

Juan Antonio Moreno Perez, **Isidoro Ruiz García**, Yolanda Morilla Garcia, Alberto José Palma Lopez, Miguel Ángel Carvajal Rodríguez; *Proton dosimetry with commercial MOSFETs*; 18th International School on the Effects of Radiation on Embedded Systems for Space Applications (SERESSA). Suiza, Diciembre 2022.

Bibliography

[1] STANLEY, R.C. Microprocessors in Brief. *IBM journal of research and development* **1985**, *29*, 110-131

[2] Dortmans, H.M.J.M. Application of Microprocessors. *Journal of physics. E, Scientific instruments* **1981**, *14*, 777-782

[3] Furber, S. Microprocessors: The Engines of the Digital Age. *Proc. R. Soc. A* **2017**, *473*, 20160893

[4] McGrath, J.; Neville, J.; Stewart, T.; Cronin, J. Upper Body Activity Classification using an Inertial Measurement Unit in Court and Field-Based Sports: A Systematic Review. *Proceedings of the Institution of Mechanical Engineers, Part P: Journal of Sports Engineering and Technology* **2021**, *235*, 83-95

[5] Alanen, A.; Raisanen, A.; Benson, L.; Pasanen, K. The use of Inertial Measurement Units for Analyzing Change of Direction Movement in Sports: A Scoping Review. *Br J Sports Med* **2021**, *55*, A45-A46

[6] Yu, J.; Ma, X.; Qi, S.; Liang, Z.; Wei, Z.; Li, Q.; Ni, W.; Wei, S.; Zhang, S. Key Transition Technology of Ski Jumping Based on Inertial Motion Unit, Kinematics and Dynamics. *Biomedical engineering online* **2023**, *22*, 21

[7] Bruzzo, J.; Perkins, N.C.; Mikkola, A. Embedded Inertial Measurement Unit Reveals Pole Lean Angle for Cross-Country Skiing. *Sports Eng* **2020**, *23*

[8] Winkel, D.; Bol, G.H.; Kroon, P.S.; van Asselen, B.; Hackett, S.S.; Werensteijn-Honingh, A.M.; Intven, M.P.W.; Eppinga, W.S.C.; Tijssen, R.H.N.; Kerkmeijer, L.G.W. *et al.* Adaptive Radiotherapy: The Elekta Unity MR-Linac Concept. *Clinical and translational radiation oncology* **2019**, *18*, 54-59

[9] Chargari, C.; Peignaux, K.; Escande, A.; Renard, S.; Lafond, C.; Petit, A.; Lam Cham Kee, D.; Durdux, C.; Haie-Méder, C. Radiotherapy of Cervical Cancer. *Cancer radiothérapie* **2022**, *26*, 298-308

[10] Barton, M.B.; Jacob, S.; Shafiq, J.; Wong, K.; Thompson, S.R.; Hanna, T.P.; Delaney, G.P. Estimating the Demand for Radiotherapy from the Evidence: A Review of Changes from 2003 to 2012. *Radiotherapy and oncology* **2014**, *112*, 140-144

[11] *Determination of Absorbed Dose in a Patient Irradiated by Beams of X Or Gamma Rays in Radiotherapy Procedures ICRU Report 24.*; International Commission on Radiation Units and Measurements: United States, 1987

[12] Washington, C.M. *Principles and Practice of Radiation Therapy.*; Mosby: St. Louis [u.a.], 1996

[13] Khan, F.M. *The Physics of Radiotherapy*, 3. ed. ed, 2003

[14] Rosenfeld, A.B. Electronic Dosimetry in Radiation Therapy. *Radiation measurements* **2006**, *41*, S134-S153

[15] Yang, Y.; Noviana, E.; Nguyen, M.P.; Geiss, B.J.; Dandy, D.S.; Henry, C.S. Paper-Based Microfluidic Devices: Emerging Themes and Applications. *Analytical chemistry (Washington)* **2017**, *89*, 71-91

[16] Santhiago, M.; Nery, E.W.; Santos, G.P.; Kubota, L.T. Microfluidic Paper-Based Devices for Bioanalytical Applications. *Bioanalysis* **2014**, *6*, 89-106

[17] MARTINEZ, A.W.; PHILLIPS, S.T.; WHITESIDES, G.M.; CARRILHO, E. Microfluidic Paper-Based Analytical Devices: Emerging Themes and Applications. *Analytical chemistry (Washington)* **2010**, *82*, 3-10

[18] Ramachandran, B.; Liao, Y. Microfluidic Wearable Electrochemical Sweat Sensors for Health Monitoring. *Biomicrofluidics* **2022**, *16*, 051501

[19] Li, S.; Ma, Z.; Cao, Z.; Pan, L.; Shi, Y. Advanced Wearable Microfluidic Sensors for Healthcare Monitoring. *Small (Weinheim an der Bergstrasse, Germany)* **2020**, *16*, e1903822-n/a

[20] Qin, N.; Zhao, P.; Ho, E.A.; Xin, G.; Ren, C.L. Microfluidic Technology for Antibacterial Resistance Study and Antibiotic Susceptibility Testing: Review and Perspective. *ACS sensors* **2021**, *6*, 3-21

[21] Lievens, Y.; Borras, J.M.; Grau, C. Cost Calculation: A Necessary Step Towards Widespread Adoption of Advanced Radiotherapy Technology. *Acta Oncologica* **2015**, *54*, 1275

[22] Borras, J.M.; Lievens, Y.; Dunscombe, P.; Coffey, M.; Malicki, J.; Corral, J.; Gasparotto, C.; Defourny, N.; Barton, M.; Verhoeven, R. *et al.* The Optimal Utilization Proportion of External Beam Radiotherapy in European Countries: An ESTRO-HERO Analysis. *Radiotherapy and Oncology* **2015**, *116*, 38

[23] Rosenberg, I. *Radiation Oncology Physics: A Handbook for Teachers and Students*.; Nature Publishing Group: London, 2008; pp. 1020

[24] Romei, C.; Di Fulvio, A.; Traino, C.A.; Ciolini, R.; d'Errico, F. Characterization of a Low-Cost PIN Photodiode for Dosimetry in Diagnostic Radiology. *Physica Medica* **2015**, *31*, 112-116

[25] Andjelković, M.S.; Ristić, G.S. Feasibility Study of a Current Mode Gamma Radiation Dosimeter Based on a Commercial PIN Photodiode and a Custom made Auto-Ranging Electrometer. *Nuclear Technology and Radiation Protection* **2013**, *28*, 73-83

[26] Shi, J.; Simon, W.E.; Zhu, T.C. Modeling the Instantaneous Dose Rate Dependenceof Radiation Diode Detectors. *Medical physics (Lancaster)* **2003**, *30*, 2509-2519

[27] Knoll, G.F. *Radiation Detection and Measurement*, 3rd Ed. ed.; John Wiley & Sons, Inc, 2000

[28] Barthe, J. Electronic Dosimeters Based on Solid State Detectors. *Nuclear Instruments and Methods in Physics Research, Section B: Beam Interactions with Materials and Atoms* **2001**, *184*, 158-189

[29] Rosenfeld, A.B. Electronic Dosimetry in Radiation Therapy. *Radiat. Measur.* **2006**, *41*, S134-S153

[30] Soubra, M.; Cygler, J.; Mackay, G. Evaluation of a Dual Bias Dual Metal Oxide-Silicon Semiconductor Field Effect Transistor Detector as Radiation Dosimeter. *Med. Phys.* **1994**, *21*, 567-572

[31] Hughes, R.C.; Huffman, D.; Snelling, J.V.; Zipperian, T.E.; Ricco, A.J.; Kelsey, C.A. Miniature Radiation Dosimeter for in Vivo Radiation Measurements. *International Journal of Radiation Oncology*Biology*Physics* **1988**, *14*, 963-967

[32] R. A. Price; C. Benson; M. J. Joyce; K. Rodgers. Development of a RadFET Linear Array for Intracavitary in Vivo Dosimetry during External Beam Radiotherapy and Brachytherapy. *IEEE Transactions on Nuclear Science* **2004**, *51*, 1420-1426

[33] Holmes-Siedle, A.; Adams, L. RADFET: A Review of the use of Metal-Oxide-Silicon Devices as Integrating Dosimeters. *International Journal of Radiation Applications and Instrumentation.Part C.Radiation Physics and Chemistry* **1986**, *28*, 235-244

[34] Andjelkovic, M.; Simevski, A.; Chen, J.; Schrape, O.; Stamenkovic, Z.; Krstic, M.; Ilic, S.; Ristic, G.; Jaksic, A.; Vasovic, N. *et al.* A Design Concept for Radiation Hardened RADFET Readout System for Space Applications. *Microprocessors and microsystems* **2022**, *90*, 104486

[35] Sarrabayrouse, G.; Siskos, S. Radiation Dose Measurement using MOSFETS. *IEEE instrumentation & measurement magazine* **1998**, *1*, 26-34

[36] Ma, T.P.; Dressendorfer, P.V. *Ionizing Radiation Effects in MOS Devices and Circuits*.; New York, NY (USA); John Wiley and Sons Inc: United States, 1989

[37] Carvajal, M.A.; Martínez-García, M.S.; Guirado, D.; Banqueri, J.; Palma, A.J. Dose Verification System Based on MOS Transistor for Real-Time Measurement. *Sensors and Actuators, A: Physical* **2016**, *247*

[38] Supej, M.; Kugovnik, O.; Nemec, B. Kinematic Determination of the Beginning of a Ski Turn. *Kinesiologia Slovenica* **2003**, *9*, 11-17

[39] Reid, R.C. A Kinematic and Kinetic Study of Alpine Skiing Technique in Slalom. **2010**, 371

[40] Azadi, B.; Haslgrübler, M.; Anzengruber-Tanase, B.; Grünberger, S.; Ferscha, A. Alpine Skiing Activity Recognition using Smartphone's IMUs. *Sensors (Basel, Switzerland)* **2022**, *22*, 5922

[41] Supej, M. 3D Measurements of Alpine Skiing with an Inertial Sensor Motion Capture Suit and GNSS RTK System. *J. Sports Sci.* **2010**, *28*, 759-769

[42] Aragón, L.F. Evaluation of Four Vertical Jump Tests: Methodology, Reliability, Validity, and Accuracy. *Measurement in physical education and exercise science* **2000**, *4*, 215-228

[43] Pérez-Chirinos Buxadé, C.; Fernández-Valdés, B.; Morral-Yepes, M.; Tuyà Viñas, S.; Padullés Riu, J.M.; Moras Feliu, G. Validity of a Magnet-Based Timing System using the Magnetometer Built into an IMU. *Sensors (Basel, Switzerland)* **2021**, *21*, 5773

[44] Azadi, B.; Haslgrübler, M.; Anzengruber-Tanase, B.; Grünberger, S.; Ferscha, A. Alpine Skiing Activity Recognition using Smartphone's IMUs. *Sensors (Basel, Switzerland)* **2022**, *22*, 5922

[45] Hussein Lopez-Nava, I.; Munoz-Melendez, A. Wearable Inertial Sensors for Human Motion Analysis: A Review. *JSEN* **2016**, *16*, 7821-7834

[46] Yuan, Q.; Chen, I. Human Velocity and Dynamic Behavior Tracking Method for Inertial Capture System. *Sensors and actuators. A. Physical.* **2012**, *183*, 123-131

[47] Liu, H.; Hartmann, Y.; Schultz, T. CSL-SHARE: A Multimodal Wearable Sensor-Based Human Activity Dataset. *Frontiers in computer science (Lausanne)* **2021**, *3*

[48] Yoshioka, S.; Fujita, Z.; Hay, D.C.; Ishige, Y. Pose Tracking with Rate Gyroscopes in Alpine Skiing. *Sports Engineering* **2018**, *21*, 177-188

[49] Moreno-Pérez, J.A.; Ruiz-García, I.; Navarro-Marchal, I.; López-Ruiz, N.; Gómez-López, P.J.; Palma, A.J.; Carvajal, M.A. System Based on an Inertial Measurement Unit for Accurate Flight Time Determination in Vertical Jumps. *Sensors (Basel, Switzerland)* **2023**, *23*, 6022

[50] Straeten, M.; Rajai, P.; Ahamed, M.J. Method and Implementation of Micro Inertial Measurement Unit (IMU) in Sensing Basketball Dynamics. *Sensors and actuators. A. Physical.* **2019**, *293*, 7-13

[51] Kasabalis, A.; Douda, H.; Tokmakidis, S.P. Relationship between Anaerobic Power and Jumping of Selected Male Volleyball Players of Different Ages. *Perceptual and motor skills* **2005**, *100*, 607-614

[52] Borodacz, K.; Szczepański, C.; Popowski, S. Review and Selection of Commercially Available IMU for a Short Time Inertial Navigation. *Aircraft engineering* **2022**, *94*, 45-59

[53] Schall, M.C.; Chen, H.; Cavuoto, L. Wearable Inertial Sensors for Objective Kinematic Assessments: A Brief Overview. *Journal of occupational and environmental hygiene* **2022**, *19*, 501-508

[54] Martínez, A.; Brunauer, R.; Venek, V.; Snyder, C.; Jahnel, R.; Buchecker, M.; Thorwartl, C.; Stöggl, T. Development and Validation of a Gyroscope-Based Turn Detection Algorithm for Alpine Skiing in the Field. *Frontiers in sports and active living* **2019**, *1*, 18

[55] Bar-Shalom, Y.; Li, X.; Kirubarajan, T. *Estimation with Applications to Tracking and Navigation*, 2001

[56] Kalman, R.E. A New Approach to Linear Filtering and Prediction Problems. *J. Fluids Eng* **1960**, *82*, 35-45

[57] Julier, S.J.; Uhlmann, J.K. New Extension of the Kalman Filter to Nonlinear Systems. *Proceedings of SPIE* **1997**, *3068*, 182-193

[58] Mahony, R.; Hamel, T.; Pflimlin, J.-. Nonlinear Complementary Filters on the Special Orthogonal Group. *TAC* **2008**, *53*, 1203-1218

[59] Madgwick, S.O.H.; Harrison, A.J.L.; Vaidyanathan, R. Estimation of IMU and MARG Orientation using a Gradient Descent Algorithm. In ; pp. 1-7

[60] Mahony, R.; Hamel, T.; Pflimlin, J.-. Nonlinear Complementary Filters on the Special Orthogonal Group. *TAC* **2008**, *53*, 1203-1218

[61] Doucet, A. *Sequential Monte Carlo Methods in Practice*, 2001st ed.; Springer: New York [u.a.], 2010

[62] Fiore, L.; Mazzaracchio, V.; Serani, A.; Fabiani, G.; Fabiani, L.; Volpe, G.; Moscone, D.; Bianco, G.M.; Occhiuzzi, C.; Marrocco, G. *et al.* Microfluidic Paper-Based Wearable Electrochemical Biosensor for Reliable Cortisol Detection in Sweat. *Sensors and actuators. B, Chemical* **2023**, *379*, 133258

[63] Weng, X.; Kang, Y.; Guo, Q.; Peng, B.; Jiang, H. Recent Advances in Thread-Based Microfluidics for Diagnostic Applications. *Biosensors & bioelectronics* **2019**, *132*, 171-185

[64] Choi, J.R.; Nilghaz, A.; Chen, L.; Chou, K.C.; Lu, X. Modification of Thread-Based Microfluidic Device with Polysiloxanes for the Development of a Sensitive and Selective Immunoassay. *Sensors and actuators. B, Chemical* **2018**, *260*, 1043-1051

[65] Wu, P.; Zhang, C. Low-Cost, High-Throughput Fabrication of Cloth-Based Microfluidic Devices using a Photolithographical Patterning Technique. *Lab on a chip* **2015**, *15*, 1598-1608

[66] Zhang, C.; Su, Y.; Liang, Y.; Lai, W. Microfluidic Cloth-Based Analytical Devices: Emerging Technologies and Applications. *Biosensors & bioelectronics* **2020**, *168*, 112391

[67] Abe, K.; Suzuki, K.; Citterio, D. Inkjet-Printed Microfluidic Multianalyte Chemical Sensing Paper. *Anal. Chem.* **2008**, *80*, 6928-6934

[68] MARTINEZ, A.W.; PHILLIPS, S.T.; WHITESIDES, G.M.; CARRILHO, E. Diagnostics for the Developing World: Microfluidic Paper-Based Analytical Devices. *Analytical chemistry (Washington)* **2010**, *82*, 3-10

[69] Cate, D.M.; Adkins, J.A.; Mettakoonpitak, J.; Henry, C.S. Recent Developments in Paper-Based Microfluidic Devices. *Analytical chemistry (Washington)* **2015**, *87*, 19-41

[70] Malon, R.S.P.; Heng, L.Y.; Córcoles, E.P. Recent Developments in Microfluidic Paper-, Cloth-, and Thread-Based Electrochemical Devices for Analytical Chemistry. *Reviews in analytical chemistry* **2017**, *36*, 1811-1824

[71] Ortiz-Gómez, I.; Salinas-Castillo, A.; García, A.G.; Álvarez-Bermejo, J.A.; de Orbe-Payá, I.; Rodríguez-Diéguez, A.; Capitán-Vallvey, L.F. Microfluidic Paper-Based Device for Colorimetric Determination of Glucose Based on a Metal-Organic Framework Acting as Peroxidase Mimetic. *Microchim Acta* **2018**, *185*, 47-8

[72] Akyazi, T.; Basabe-Desmonts, L.; Benito-Lopez, F. Review on Microfluidic Paper-Based Analytical Devices Towards Commercialisation. *Analytica chimica acta* **2018**, *1001*, 1-17

[73] Darcy, H. *The Public Fountains of the City of Dijon*, Orig. publ. [in French] in 1856 in Paris ed.; Kendall/Hunt Publ. Co: Dubuque, Iowa, 2004

[74] Washburn, E.W. The Dynamics of Capillary Flow. *Physical review* **1921**, *17*, 273-283

[75] Lucas, R. Ueber Das Zeitgesetz Des Kapillaren Aufstiegs Von Flüssigkeiten. *Colloid and polymer science* **1918**, *23*, 15-22

[76] Jeong, S.; Kim, J.; Jin, S.H.; Park, K.; Lee, C. Flow Control in Paper-Based Microfluidic Device for Automatic Multistep Assays: A Focused Minireview. *Korean J. Chem. Eng* **2016**, *33*, 2761-2770

[77] Cunningham, J.C.; DeGregory, P.R.; Crooks, R.M. New Functionalities for Paper-Based Sensors Lead to Simplified User Operation, Lower Limits of Detection, and New Applications. *Annual review of analytical chemistry (Palo Alto, Calif.)* **2016**, *9*, 183-202

[78] Fu, E.; Lutz, B.; Kauffman, P.; Yager, P. Controlled Reagent Transport in Disposable 2D Paper Networks. *Lab on a Chip* **2010**, *1*, 918-92

[79] Martinez, A.W.; Phillips, S.T.; Nie, Z.; Cheng, C.; Carrilho, E.; Wiley, B.J.; Whitesides, G.M. Programmable Diagnostic Devices made from Paper and Tape. *Lab on a chip* **2010**, *10*, 2499-2504

[80] Li, X.; Zwanenburg, P.; Liu, X. Magnetic Timing Valves for Fluid Control in Paper-Based Microfluidics. *Lab on a chip* **2013**, *13*, 2609-2614

[81] Shin, J.H.; Park, J.; Kim, S.H.; Park, J. Programmed Sample Delivery on a Pressurized Paper. *Biomicrofluidics* **2014**, *8*, 054121

[82] Jahanshahi-Anbuhi, S.; Chavan, P.; Sicard, C.; Leung, V.; Hossain, S.M.Z.; Pelton, R.; Brennan, J.D.; Filipe, C.D.M. Creating Fast Flow Channels in Paper Fluidic Devices to Control Timing of Sequential Reactions. *Lab on a chip* **2012**, *12*, 579-585

[83] Toley, B.J.; McKenzie, B.; Liang, T.; Buser, J.R.; Yager, P.; Fu, E. Tunable-Delay Shunts for Paper Microfluidic Devices. *Analytical chemistry (Washington)* **2013**, *85*, 11545-11552

[84] Jahanshahi-Anbuhi, S.; Henry, A.; Leung, V.; Sicard, C.; Pennings, K.; Pelton, R.; Brennan, J.D.; Filipe, C.D.M. Paper-Based Microfluidics with an Erodible Polymeric Bridge Giving Controlled Release and Timed Flow Shutoff. *Lab on a chip* **2014**, *14*, 229-236

[85] Gerbers, R.; Foellscher, W.; Chen, H.; Anagnostopoulos, C.; Faghri, M. A New Paper-Based Platform Technology for Point-of-Care Diagnostics. *Lab on a chip* **2014**, *14*, 442-449

[86] Noh, H.; Phillips, S.T. Metering the Capillary-Driven Flow of Fluids in Paper-Based Microfluidic Devices. *Analytical chemistry (Washington)* **2010**, *82*, 4181-4187

[87] Phillips, E.A.; Shen, R.; Zhao, S.; Linnes, J.C. Thermally Actuated Wax Valves for Paper-Fluidic Diagnostics. *Lab on a chip* **2016**, *16*, 4230-4236

[88] Akyazi, T.; Gil-González, N.; Basabe-Desmonts, L.; Castaño, E.; Morant-Miñana, M.C.; Benito-Lopez, F. Manipulation of Fluid Flow Direction in Microfluidic Paper-Based Analytical Devices with an Ionogel Negative Passive Pump. *Sensors and actuators. B, Chemical* **2017**, *247*, 114-123

[89] Akyazi, T.; Saez, J.; Elizalde, J.; Benito-Lopez, F. Fluidic Flow Delay by Ionogel Passive Pumps in Microfluidic Paper-Based Analytical Devices. *Sensors and actuators. B, Chemical* **2016**, *233*, 402-408

[90] Gao, Y.; Wei, M.; Li, X.; Xu, W.; Ahiabu, A.; Perdiz, J.; Liu, Z.; Serpe, M.J. Stimuli-Responsive Polymers: Fundamental Considerations and Applications. *Macromol. Res* **2017**, *25*, 513-527

[91] D'Eramo, L.; Chollet, B.; Leman, M.; Martwong, E.; Li, M.; Geisler, H.; Dupire, J.; Kerdraon, M.; Vergne, C.; Monti, F. *et al.* Microfluidic Actuators Based on Temperature-Responsive Hydrogels. *Microsystems & nanoengineering* **2018**, *4*, 17069

[92] Ziółkowski, B.; Czugala, M.; Diamond, D. Integrating Stimulus Responsive Materials and Microfluidics: The Key to Next-Generation Chemical Sensors. *Journal of intelligent material systems and structures* **2013**, *24*, 2221-2238

[93] Ruiz-Garc, I.; Rom An-Raya, J.; Us Banqueri, J.; Palma, A.J.; Carvajal, M.A. Commercial Photodiodes and Phototransistors as Dosimeters of Photon Beams for Radiotherapy.

[94] Sze, S.M.; Ng, K.K. *Physics of Semiconductor Devices, Third Edition*, 3rd ed. ed.; Wiley, 2006

[95] Soliman, F.A.S.; Ashry, H.A. Radiation Effects on Non-Linear Resistances. *J. Mater. Sci. : Mater. Electron.* **1993**, *4*, 293-300

[96] Ruiz-García, I.; Navarro-Marchal, I.; Ocaña-Wilhelmi, J.; Palma, A.J.; Gómez-López, P.J.; Carvajal, M.A. Development and Evaluation of a Low-Drift Inertial Sensor-Based System for Analysis of Alpine Skiing Performance. **2021**, *21*

[97] Ruiz-Garca, I.; Escobedo, P.; Ramos-Lorente, C.E.; Erenas, M.M.; Capitn-Vallvey, L.F.; Carvajal, M.A.; Palma, A.J.; Lpez-Ruiz, N. Capacitive Platform for Real-Time Wireless Monitoring of Liquid Wicking in a Paper Strip. *Lab on a chip* **2023**, *23*, 492-413

[98] Chen, L.; Wu, C.; Wu, R.; Chang, H. Electroosmotic Flow Control in Microfluidic Chips using a Self-Assembled Monolayer as the Insulator of a Flow Field-Effect Transistor. *Langmuir, Volume 28* **2012**, *28*, Langmuir, Volume 28, Issue 31, page(s) 11281–11285.

[99] Román-Raya, J.; Ruiz-García, I.; Escobedo, P.; Palma, A.J.; Guirado, D.; Carvajal, M.A. Light-Dependent Resistors as Dosimetric Sensors in Radiotherapy. *Sensors* **2020**, *20*